DISCLAIMER

This report was prepared as an account of work sponsored by an agency of the United States Government. Neither the United States Government nor any agency thereof, nor any of their employees, makes any warranty, express or implied, or assumes any legal liability or responsibility for the accuracy, completeness, or usefulness of any information, apparatus, product, or process disclosed, or represents that its use would not infringe privately owned rights. Reference herein to any specific commercial product, process, or service by trade name, trademark, manufacturer, or otherwise does not necessarily constitute or imply its endorsement, recommendation, or favoring by the United States Government or any agency thereof. The views and opinions of authors expressed herein do not necessarily state or reflect those of the United States Government or any agency thereof.

LBL-14605
GSRMP-12
TR 82-39

PHYSICAL PROCESSES OF SUBSIDENCE IN GEOTHERMAL RESERVOIRS

LBL--14605

DE83 011017

by

John F. Schatz

with contributions by

Kenneth Wolgemuth, Scott Carlisle, Mark Smith, Ahmed Abou-Sayed

Terra Tek Research
University Research Park
420 Wakara Way
Salt Lake City, Utah 84108

June 1982

Prepared for

Earth Sciences Division
Lawrence Berkeley Laboratory
University of California
Berkeley, California 94720

NOTICE
PORTIONS OF THIS REPORT ARE ILLEGIBLE.
It has been reproduced from the best available copy to permit the broadest possible availability.

This work was supported by the Assistant Secretary for Conservation and Renewable Energy, Office of Renewable Technology, Division of Geothermal and Hydropower Technologies of the U.S. Department of Energy under Contract No. DE-AC03-76SF00098 with Lawrence Berkeley Laboratory through Subcontract No. 4500310.

DISTRIBUTION OF THIS DOCUMENT IS UNLIMITED

DISCLAIMER

This report was prepared as an account of work sponsored by an agency of the United States Government. Neither the United States Government nor any agency Thereof, nor any of their employees, makes any warranty, express or implied, or assumes any legal liability or responsibility for the accuracy, completeness, or usefulness of any information, apparatus, product, or process disclosed, or represents that its use would not infringe privately owned rights. Reference herein to any specific commercial product, process, or service by trade name, trademark, manufacturer, or otherwise does not necessarily constitute or imply its endorsement, recommendation, or favoring by the United States Government or any agency thereof. The views and opinions of authors expressed herein do not necessarily state or reflect those of the United States Government or any agency thereof.

DISCLAIMER

Portions of this document may be illegible in electronic image products. Images are produced from the best available original document.

DO NOT MICROFILM THIS PAGE

LEGAL NOTICE

This book was prepared as an account of work sponsored by an agency of the United States Government. Neither the United States Government nor any agency thereof, nor any of their employees, makes any warranty, express or implied, or assumes any legal liability or responsibility for the accuracy, completeness, or usefulness of any information, apparatus, product, or process disclosed, or represents that its use would not infringe privately owned rights. Reference herein to any specific commercial product, process, or service by trade name, trademark, manufacturer, or otherwise, does not necessarily constitute or imply its endorsement, recommendation, or favoring by the United States Government or any agency thereof. The views and opinions of authors expressed herein do not necessarily state or reflect those of the United States Government or any agency thereof.

Printed in the United States of America
Available from
National Technical Information Service
U.S. Department of Commerce
5285 Port Royal Road
Springfield, VA 22161
Price Code: A08

Lawrence Berkeley Laboratory is an equal opportunity employer.

ABSTRACT

The objectives of this project were to acquire core and fluid from producing geothermal reservoirs (East Mesa, United States, and Cerro Prieto, Mexico); to test specimens of this core for their short-term and long-term (creep) compaction response; and to develop a compaction constitutive model that would allow future analysis of reservoir compaction and a surface subsidence.

A total of approximately two hundred feet of core was obtained from eleven wells in the two geothermal fields. Depths and porosities ranged from 3500 to 11,000 feet and 15 to 40 percent, respectively. Several samples of geothermal fluids were also obtained. After geologically and geochemically describing the materials obtained, selected specimens were tested for their response to the pressures and temperatures of the geothermal environment and to simulated changes in those conditions that would be caused by production. Short-term tests (for example, tests for compressibility extending over a time interval of an hour or less in the laboratory) indicated that these sedimentary materials behaved normally with respect to the expected behavior of reservoir sandstones of these depths and porosities. Compressibilities were of the order 1×10^6 psi.

Long-term tests, extending up to several weeks in duration, indicated that pore pressure reduction, simulating reservoir production, tended to cause creep compaction at an initial rate of about 1×10^{-7} percent porosity reduction per second. This rate was found to be consistent with a mechanism of porosity reduction related to pressure solution of quartz grains at contact asperities. This observation led to the development of a theory explaining the creep behavior that allowed extrapolation to long times (several years). Although

initial compaction may be small (a few tenths of a percent at most), the theory developed here indicates that ultimate compaction as caused by pore pressure reduction may range up to several percent and needs to be taken into account for ultimate subsidence predictions.

ACKNOWLEDGEMENTS

Many people have contributed to the success of this project. We thank especially: from the Earth Sciences Division of the Lawrence Berkeley Laboratory - J. Noble, T. N. Narasimhan, S. Vonder Haar, M. Lippmann, and N. Goldstein; from Republic Geothermal, Inc. - D. Michaels; from the Comisión Federal de Electricidad - Ing. A. Mañón M.; from the Mechanical Engineering Department of the University of California at Berkeley - M. Carroll; from the Terra Tek, Inc. professional staff - R. Van Buskirk and S. Kelkar; and from the Terra Tek support staff - R. Binch, L. Beard, and A. MacLeod.

This work was supported by the Assistant Secretary for Conservation and Renewable Energy, Office of Renewable Technology, Division of Geothermal and Hydropower Technologies of the U. S. Department of Energy under Contract No. DE-AC03-76SF00098 with Lawrence Berkeley Laboratory through Subcontract No. 4500310 to Terra Tek, Inc., under the Geothermal Subsidence Research Program. The program was administered by John Noble and Norman Goldstein. Mr. H. A. Todd was the contract administrator for Lawrence Berkeley Laboratory.

TABLE OF CONTENTS

		Page
	ABSTRACT	iii
	ACKNOWLEDGEMENTS	v
	LIST OF FIGURES	ix
	LIST OF TABLES	xv
1.	INTRODUCTION	1
	1.1 Background	1
	1.2 Project Objectives	2
	1.3 Project Plan	3
2.	DESCRIPTION OF MATERIALS	7
	2.1 General Geologic Information	7
	2.2 East Mesa	9
	2.3 Cerro Prieto	14
	2.4 Summary and Comparison of Cores and Fluids	27
3.	TESTING EQUIPMENT AND PROCEDURES	31
	3.1 General Information	31
	3.2 Preliminary Sample Handling	31
	3.3 Basic Testing	34
	3.3.1 Drained and Undrained Hydrostatic Compression (Isotropic Compression)	37
	3.3.2 Room Temperature and High Temperature Drained Hydrostatic Compression	39
	3.3.3 Cycling	39
	3.3.4 Pore Pressure Reduction	39
	3.3.5 Uniaxial Strain	40
	3.3.6 Ultrasonic Velocities	40
	3.4 Creep Testing	40
	3.5 Fluid Chemistry	46
	3.6 Microstructual Analyses	55
4.	BASIC TESTING RESULTS	59
	4.1 East Mesa	59
	4.1.1 Drained Hydrostats	59
	4.1.2 Pore Pressure Reduction	62
	4.1.3 Confining Pressure Cycling and Uniaxial Compaction	69
	4.2 Cerro Prieto	73

Table of Contents (continued) Page

4.2.1 Drained Hydrostats 74
4.2.2 Pore Pressure Reduction. 78
4.2.3 Confining Pressure Cycling and Uniaxial Compaction . 82
4.2.4 Ultrasonic Velocities. 82

5. CREEP TESTING RESULTS. 87

5.1 Initial Creep Tests, East Mesa. 89
5.2 Initial Creep Tests, Cerro Prieto 91

5.2.1 Volume Strain Results. 91
5.2.2 Permeability Results 95

5.3 Long-Term Creep Tests, East Mesa. 97
5.4 Long-Term Creep Tests, Cerro Prieto 99

6. FLUID CHEMISTRY RESULTS. 100

7. MINERALOGICAL AND STRUCTURAL RESULTS 107

7.1 X-Ray Diffraction 107

7.1.1 EM-5 108
7.1.2 EM-8 109

7.2 Scanning Electron Microscopy - Energy Dispersive Analysis by X-Rays 110

8. SUMMARY AND SYNTHESIS OF TEST RESULTS. 113

9. MECHANISMS OF CREEP AND THEORETICAL MODELING 121

9.1 Static Pore Collapse Theory 123
9.2 Pressure Solution Theory. 128
9.3 Creep Compaction Theory 131

10. CONCLUSIONS AND IMPLICATIONS FOR SUBSIDENCE PREDICTION 135

11. REFERENCES 137

LIST OF FIGURES

Figure	Title	Page
1	Schematic Drawing Showing Concept of Subsidence as Caused by Reservoir Compaction	1
2	Flow Chart Showing Planned Progress of Program	4
3	Map of Salton Trough Geothermal Province Showing Major Geothermal Anomalies	8
4	Detailed Map of the East Mesa Known Geothermal Resource Area	10
5	Schematic Cross Section of the East Mesa Geothermal Field Showing Approximate Depth of Producing Zones	11
6	Lithologic Log of East Mesa Well #58-30 From Which Caprock Material was Obtained for This Program	12
7	Lithologic Log of the East Mesa Well #78-30 From Which Reservoir Material was Obtained for This Program	13
8a	Photomicrograph of Fine-Grained Claystone Material From Caprock in East Mesa Well #58-30	16
8b	Photomicrograph of Fine- to Medium-Grained Sandstone Material From Reservoir Depth in Well 78-30	16
9	Map of Cerro Prieto Geothermal Well Locations Showing Wells for Which Core was Obtained for This Program	18
10	Schematic Cross Section of Cerro Prieto Geothermal Field Showing Approximate Depth From Which Core was Obtained for This Program	19
11a	Photomicrograph of Thin Section from Cerro Prieto Well M-110	23
11b	Photomicrograph of Thin Section from Cerro Prieto Well E-366	23
11c	Photomicrograph of Thin Section from Cerro Prieto Well M-7	24
11d	Photomicrograph of Thin Section from Cerro Prieto Well M-93	24
12	Apparatus for Determination of Calcite Content by Carbon Dioxide Evolution	25

List of Figures (continued)

Figure	Title	Page
13	Calibration of Carbon Dioxide Evolution Apparatus Showing the Accuracy of Method is About ±1/2 percent.	25
14	Approximate Temperature Ranges in the East Mesa and Cerro Prieto Geothermal Reservoirs.	29
15	Schematic Diagram of Assembled Test Specimen Showing Sample, Endcaps, Jacket, and Pore Fluid Connections	33
16	Schematic Diagram of the High Pressure, Medium Temperature System Used for Basic Testing	35
17	Photograph of System Used for Basic Testing	35
18	Diagram of Pore Pressure System Used for Basic Testing. . .	36
19	Schematic Diagram of Test Specimen Showing Axial and Transverse Cantilever Strain Transducers.	38
20	Photograph of Assembled Test Specimen Showing Strain Transducers	38
21	Schematic Diagram of High Temperature Creep Testing System.	41
22	Photograph of High-Temperature Creep System	42
23	Photograph of Sample Assembly, for High Temperature Creep Measurement	42
24	Outline of Creep Testing Procedure.	44
25	Schematic Diagram of Pore Fluid Sampling System Used During High Temperature Creep Testing	48
26	Schematic Diagram of Acid Injection System Used to Achieve Carbonate Equilibrium and Correct pH for High Temperature, High Pressure Testing	50
27	Flow Chart of Cycle Through Which Fluid From the Cerro Prieto Reservoir was Taken Between Sampling at the Wellhead and Final Analysis After Testing	51
28	Schematic Diagram Showing Flushing Procedure Used to Achieve Fluid Equilibrium Prior to Creep Testing.	56
29-30	Drained Hydrostat on Caprock Material from East Mesa Well 58-30.	60

List of Figures (continued)

Figure	Title	Page
31-32	Drained Hydrostat on Reservoir Material from East Mesa Well 78-30.	61
33-35	Pore Pressure Cycling Test on Caprock Material from East Mesa 58-30.	64
36-41	Pore Pressure Cycling Test on Reservoir Material from East Mesa 78-30	66
42	Confining Pressure Cycling Test on Caprock Material from East Mesa Well 58-30.	70
43	Confining Pressure Cycling Test on Caprock Material from East Mesa Well 78-30.	70
44	Confining Pressure Cycling Test on Reservoir Material from East Mesa Well 78-30	71
45	Uniaxial Compaction Test on Reservoir Material from East Mesa Well 58-30	71
46-47	Uniaxial Compaction Test on Reservoir Material from East Mesa Well 78-30	72
48-49	Drained Hydrostat on Material from Cerro Prieto Well M-123.	75
50-53	Drained Hydrostat on Material from Cerro Prieto Well T-366.	76
54-55	Pore Pressure Cycling Test on Material from Cerro Prieto Well M-107.	79
56-57	Pore Pressure Cycling Test on Material from Cerro Prieto Well M-127.	80
58-59	Pore Pressure Cycling Test on Material from Cerro Prieto Well T-366.	81
60	Confining Pressure Cycling Test on Cerro Prieto Material From Well M-107	83
61	Confining Pressure Cycling Test on Cerro Prieto Material From Well M-127	83
62	Confining Pressure Cycling Test on Cerro Prieto Material From Well T-366	84
63	Uniaxial Compaction Test on Material from Cerro Prieto Well T-366.	84

List of Figures (continued)

Figure	Title	Page
64	Uniaxial Compaction Test on Material from Cerro Prieto Well M-127.	85
65	Uniaxial Compaction Test on Material from Cerro Prieto Well M-107.	85
66-69	Creep Compaction Test on Material from East Mesa Well 78-30	90
70	Creep Compaction Test on Material from Cerro Prieto Well M-127.	92
71	Creep Compaction Test on Material from Cerro Prieto Well M-110.	92
72	Creep Compaction Test on Material from Cerro Prieto Well 0473	92
73	Creep Compaction Test on Material from Cerro Prieto Well M-7.	93
74	Creep Compaction Test on Material from Cerro Prieto Well M-107.	93
75	Creep Compaction Test on Material from Cerro Prieto Well M-129.	93
76	Creep Compaction Test on Material from Cerro Prieto Well NL-1	94
77	Creep Compaction Test on Material from Cerro Prieto Well M-93	94
78-80	Long-Term Creep Test on Material from East Mesa Well 78-30.	98
81	Long-Term Creep Test on Material from East Mesa Well 58-30.	98
82	Long-Term Creep Test on Material from Cerro Prieto Well T-366	99
83	Concentration of Silica with Respect to Degree of Saturation for Several Cerro Prieto Creep Tests as a Function of Time During the Tests.	104
84a	SEM Photomicrograph of Quartz Crystal in Rock After Creep Test - Material is From East Mesa well 78-30.	111
84b	SEM Photomicrograph of Void Left by Grain Plucked During Sample Preparation Process - Material is From East Mesa Well 78-30 After Creep Test	111

List of Figures (continued)

Figure	Title	Page
85	Diagram Indicating the Concept of Spherical Pore Deformation Theory	124
86	Deformation of Pore in Spherical Pore Theory.	126
87	Spherical Pore Theory Compared with Compaction Data for a Porous Tuff	127
88	Internal Contact Shearing Stress Versus Strain Rate According to the Theory of Rutter and Mainprice	130
89	Long-Term Sandstone Creep Compaction Extrapolation Predicted by Theory Derived in Text and for Parameters Typical of Those Measured During This Program	134

LIST OF TABLES

Table	Title	Page
1	East Mesa Mineralogy	15
2	East Mesa Brine Composition, Well 78-30	17
3	Core Obtained from Cerro Prieto	21
4	Cerro Prieto Mineralogy	22
5	Cerro Prieto Calcite Contents	26
6	Cerro Prieto Brine Composition, Average	28
7	Average Properties of Cores and Fluids Obtained From East Mesa and Cerro Prieto	28
8	East Mesa Brine Composition, Well 78-30	48
9	Cerro Prieto Brine Composition	52
10	Pore Fluid Chemistry Analysis	54
11	Experimental Accuracy	54
12	Initial Conditions, East Mesa Pore Pressure Reduction Tests	63
13	Initial Conditions, Cerro Prieto Pore Pressure Reduction Tests	78
14	Ultrasonic Velocities, Cerro Prieto	86
15	Creep Test Summary	88
16	Permeabilities, Cerro Prieto	96
17	East Mesa Fluid Chemistry Summary	101
18	Cerro Prieto Fluid Chemistry Summary	102
19	Silica and Carbonate Chemistry	103
20	XRD Scans Obtained of Separated Clays	108
21	Typical Mineralogy of Test Specimens	114
22	Test Conditions	114
23	Basic Tests - Average Results	116

List of Tables (continued)

Table	Title	Page
24	Ultrasonic Velocities - Average Results	116
25	Creep Tests - Average Results	117
26	Permeability Tests - Average Results.	120

1. INTRODUCTION

1.1 Background

The withdrawal of fluids in large quantities from subsurface reservoirs, and subsequent pore pressure reduction, creates the potential for reservoir compaction and in turn, the possibility of surface subsidence. A conceptual drawing is shown in Figure 1. Subsidence has been observed in the past in many locations in the world in association with both water and oil withdrawal. More recently, subsidence has been identified as a possible consequence of hydrothermal fluid production from geothermal reservoirs. For example, in California's Imperial Valley, hot brines will be produced from a geologically young sedimentary sequence of sands and shales, and cooler fluids may be reinjected. The compaction of the subsurface aquifer and layers above, as caused by fluid pressure reduction, may propagate to the surface in the form of subsidence and may affect natural or man-made agricultural drainage systems.

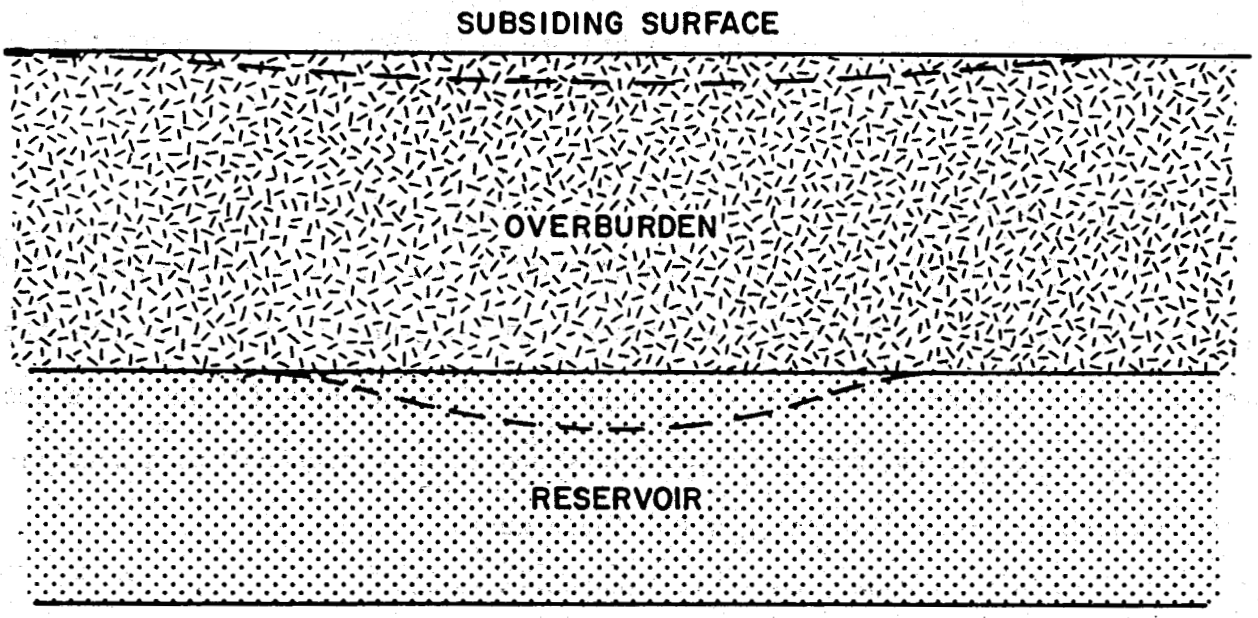

Figure 1. Schematic drawing showing concept of subsidence as caused by reservoir compaction. Solid lines are initial surfaces and dashed lines are surfaces after compaction and subsidence have occurred.

Little is known about the exact potential for subsidence in geothermal areas. Extraction rates may be large, therefore increasing the potential for subsidence; on the other hand, depths may be substantial, thus decreasing the potential for subsidence. Some data exist and have been reviewed (such as Grimsrud, et al., 1978.) For example, at Wairakei, New Zealand, production of geothermal fluids has caused local subsidence of more than 15 feet in ten years. The area of surface affected was approximately 3000 feet in diameter. It should be noted that Wairakei is in a volcanic geologic setting and no fluid has been reinjected. Many other geothermal areas are in sedimentary basins and may not react in a way consistent with the experience at Wairakei. In sedimentary basins, experience with subsidence caused by water and oil production may be more applicable. In any case, it is desirable to have a method of understanding and predicting subsidence in geothermal areas. Because of the lack of widespread historical experience, it is extremely unlikely that an accurate empirical model can be developed in the near future. Consequently, a logical first step (aside from gathering as much field information as possible) is to investigate the physical mechanisms of compaction in geothermal reservoir rocks as caused by pore pressure reduction.

1.2 Project Objectives

The major objective of this project was to study, in the laboratory, the compaction of rock obtained from geothermal reservoirs and to relate that compaction to parameters that are observable or measurable in the field such as depth, temperature, and reservoir pressure. To be somewhat more specific, the project had four distinct goals. These were:

1. To obtain core from active geothermal areas.
2. To perform a variety of tests at simulated in-situ conditions with emphasis on the study of compaction as triggered by pore pressure reduction.

3. To identify, as accurately as possible, the mechanisms of compaction.
4. To develop a constitutive model for reservoir compaction as triggered by pore pressure reduction.

Resulting from this project are a data set and interpretations in terms of constitutive behavior that will be useful to reservoir modelers for the purposes of the understanding and predicting of subsidence. In addition, some spinoff benefits are derived for reservoir engineers in terms of improved understanding of compressibility, permeability, borehole stability and deposition-solution phenomena in geothermal areas.

1.3 Project Plan

A flow chart of the project, as planned, is shown in Figure 2. Two major legs of the project started simultaneously. One leg began with obtaining core from known and developing geothermal areas. The other leg began with test machine modification to prepare equipment for creep compaction experiments, since the possibility of time-dependent effects at geothermal reservoirs temperatures was considered important enough to warrant study.

Through discussion and cooperation with the Lawrence Berkeley Laboratory, the U.S. Department of Energy, Republic Geothermal, Inc., and the Commission Federal de Electricidad of Mexico, core was obtained from the East Mesa geothermal field in California and the Cerro Prieto geothermal field, Mexico. Core was brought to the laboratory where lithology, and properties such as density and porosity were determined. Then, work entered into a testing phase for basic mechanical properties with emphasis on measurements of compressibility at reservoir conditions. With basic measurements completed, three types of experiments were conducted: 1) compaction experiments, where reservoir conditions were achieved, and specimens were caused to compact by reduction of pore pressure; 2) flow experiments, where reservoir conditions were achieved,

PROGRAM FLOW CHART

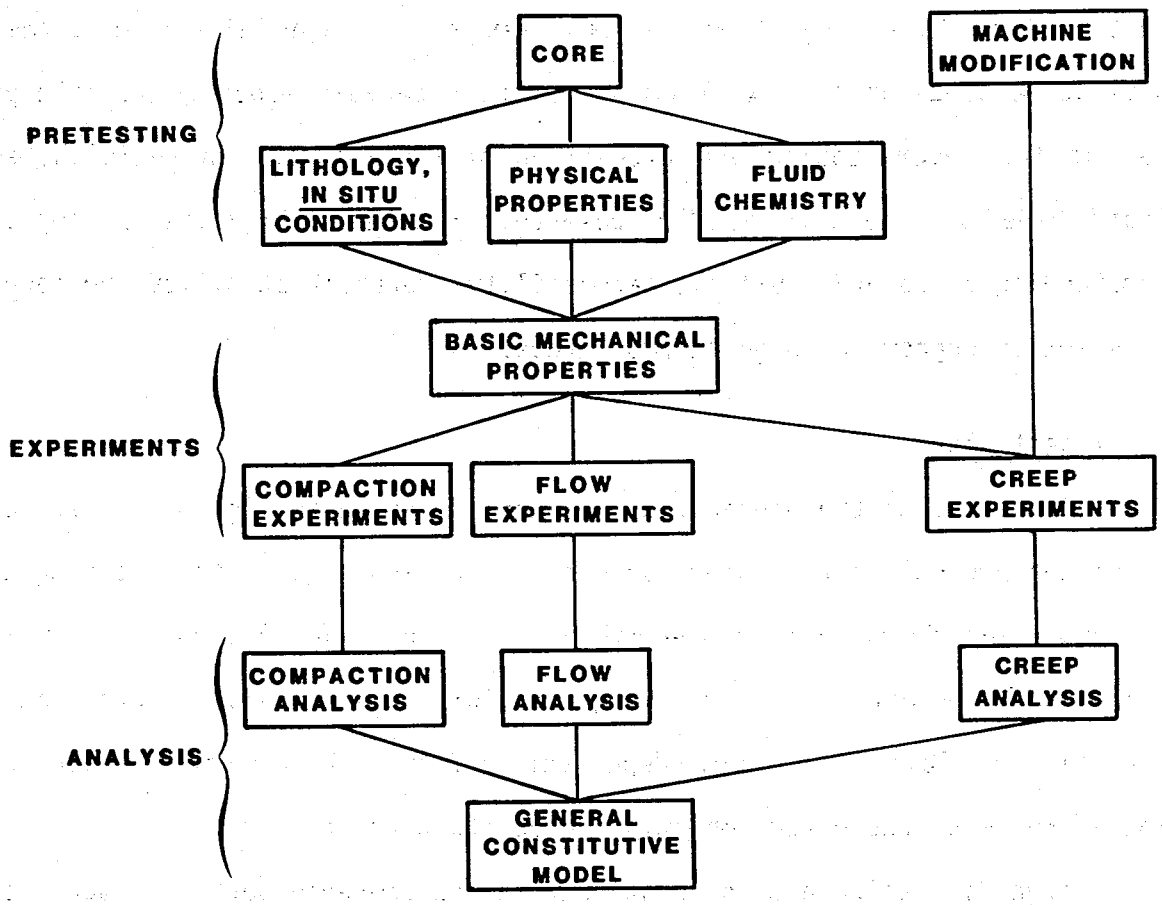

Figure 2. Flow chart showing planned progress of program.

pore pressure was reduced, and effects on permeability were investigated; and 3) creep experiments, where reservoir conditions were achieved, pore pressure was reduced and then held at a reduced value for long periods of time (up to several weeks) in order to investigate time-dependent effects.

As data became available, work began on analysis. Ultimately, a general understanding of the behavior of rocks from these geothermal reservoirs was achieved. Then, theoretical work was undertaken to develop a method of extrapolation of creep behavior to long periods of time. The results of all of this work are contained in this final report.

2. DESCRIPTION OF MATERIALS

2.1 General Geologic Information

Material was obtained from two geothermal areas in the physiographic basin province known as the Salton Trough. This basin extends from south central California, in the United States, to northern Baja California, in Mexico, and southward into the Gulf of California, or the Sea of Cortez, as it is known in Mexico. This basin has been a repository for clastic sediments that have been deposited since Miocene time. (For a general survey, see Elders, 1979.) These sediments were derived mainly from the Colorado River drainage of the Colorado plateau region. The cause of geothermal activity in the region is related to the fact that this basin marks the location of a major plate tectonic boundary between the North American and Pacific plates. Figure 3 shows the location of the main geothermal areas in the trough. For this project, core was obtained from the East Mesa field in California and the Cerro Prieto field in Mexico. Core obtained (described in more detail in the following sections) can be described very generally as originating from a deltaic sedimentary sequence that has been altered by hydrothermal activity and also in some cases, by tectonic activity. Porosities of most of the sands are in the range from 10 to 40%, varying mostly with depth of burial, with the lower values being at the greater depths. These are typical values for normally consolidated sandstones. Matrix permeabilities, on the other hand, are perhaps somewhat atypically low for sands of these ages and clay contents. This is probably a result of the hydrothermal mechanisms, some of which tend to reduce permeability. (Large-scale fracture systems that would enhance flow in the geothermal systems are not observable in the laboratory.) In general appearance, these rocks do not seem to be unusually susceptible to compaction,

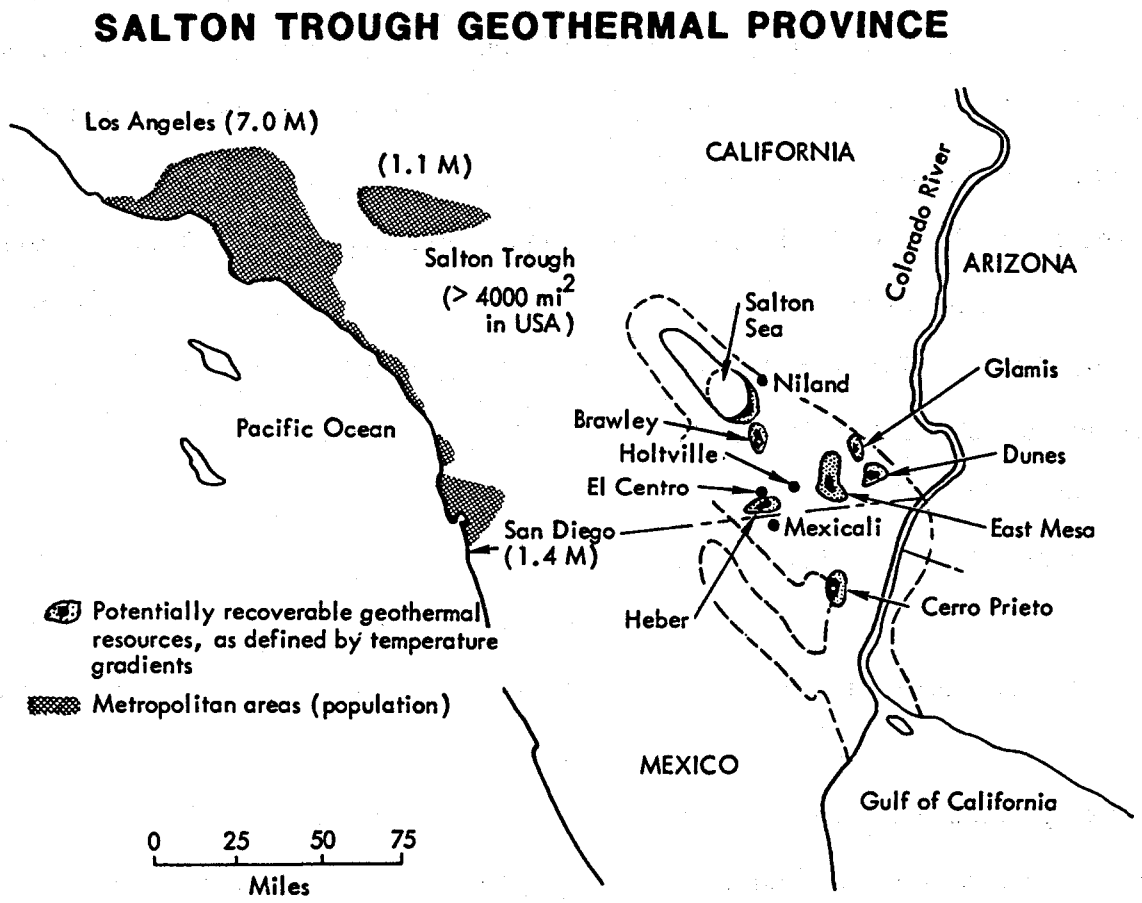

Figure 3. Map of Salton Trough Geothermal Province showing major geothermal anomalies.

i.e., they are not weak or friable; however, nor are they unusually hard or strong. We hope that they are reasonably representative of many young, hydrothermal/geothermal sedimentary materials, in terms of their susceptibility to compaction, but there is certainly no large body of evidence to support this statement. Fluid samples or fluid chemistry information was also obtained for each reservoir. This was done in order to maintain appropriate chemical equilibrium conditions during the testing of the rock. The following sections give detailed information on core obtained and on fluid properties associated with each reservoir.

2.2 East Mesa

A map of the East Mesa geothermal field is shown in Figure 4. Core was obtained, with the cooperation of Republic Geothermal, Inc., from two wells in section 30 of this field. The wells were #58-30 and #78-30. A total of 40 feet of core was obtained.

In well #78-30, core was recovered from 5500-5540 feet and from 7135-7170 feet. Both these zones are production zones as shown in the schematic stratigraphic cross-section in Figure 5. As discussed further below, the rocks from these zones were quartz sandstones with various amounts of clay, and calcite and silica cements. Rock from the cap rock zone of the reservoir was obtained from well #58-30 at depths from 3252-3282 feet. In this case, the rock was largely claystone with minor stringers of siltstone and sandstone.

All core was recovered at the wellhead, wrapped in aluminum foil and sealed in wax for transport to the Terra Tek laboratory. This was done to prevent dehydration of the pore spaces and clays which might otherwise affect the mechanical properties of the rock. A lithologic log obtained from core descriptions is given in Figures 6 and 7. Thirteen thin sections were prepared from the core recovered including replicates that were impregnated with

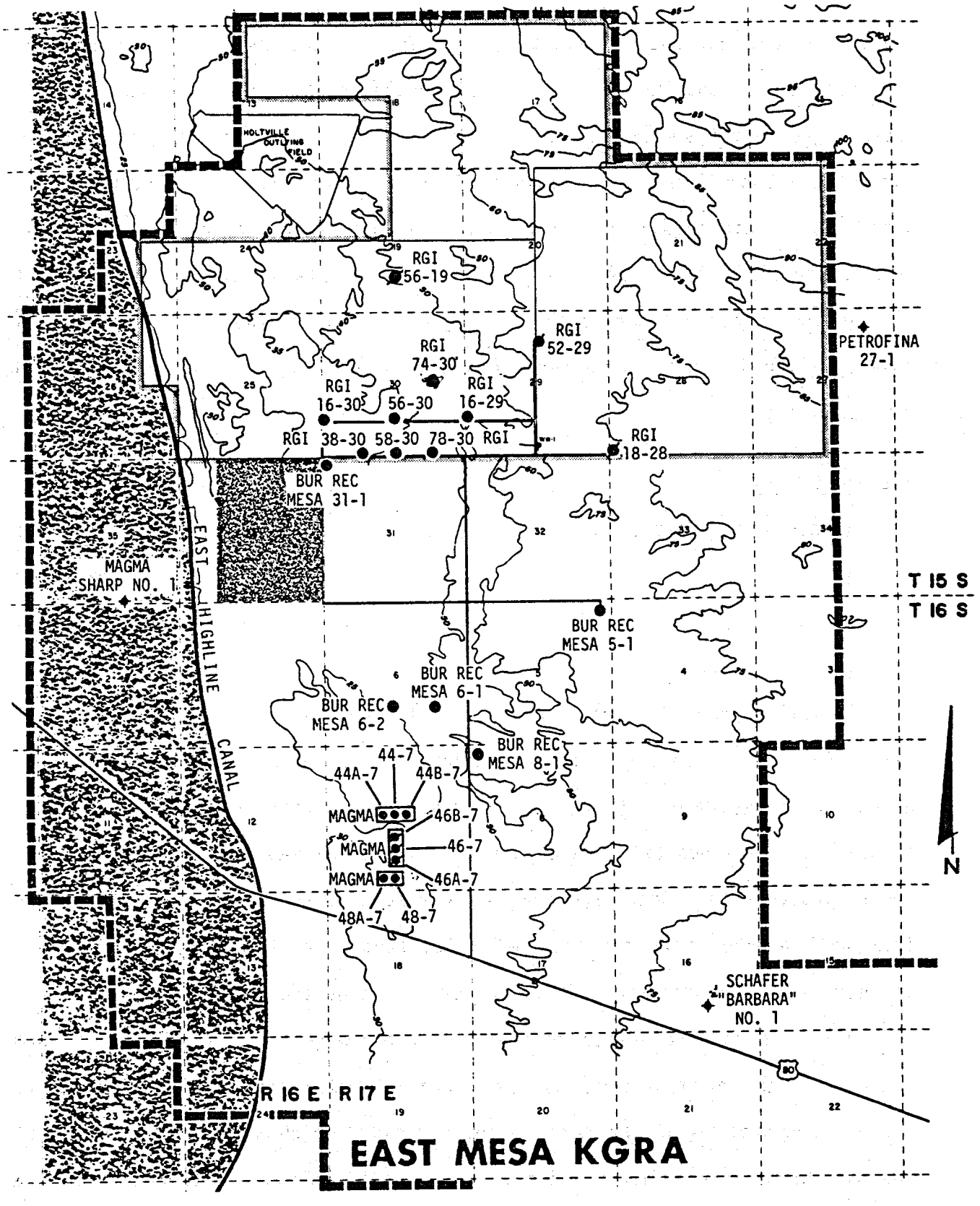

Figure 4. Detailed map of the East Mesa Known Geothermal Resource Area. Wells investigated for this program are Republic Geothermal's 58-30 and 78-30 shown in upper left center of map.

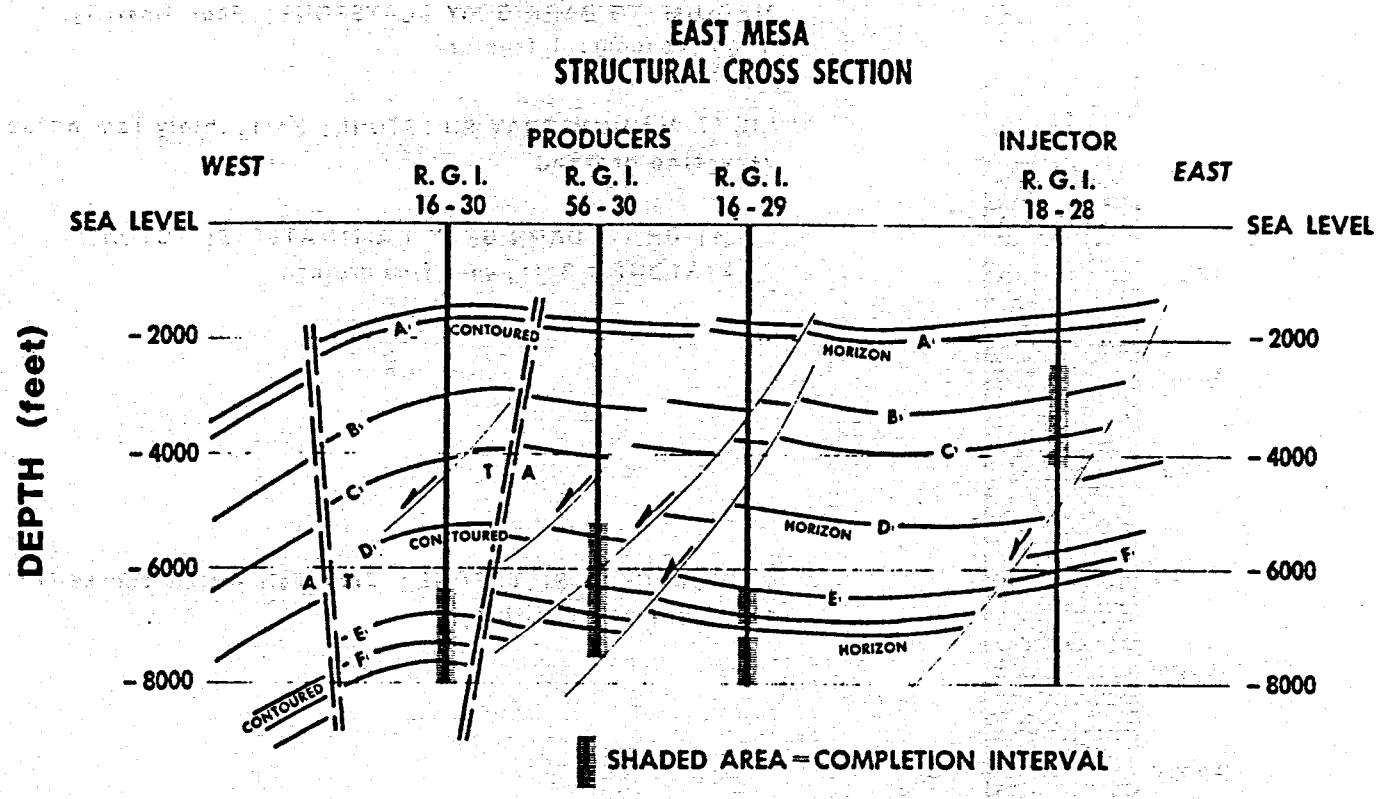

Figure 5. Schematic cross section of the East Mesa geothermal field showing approximate depth of producing zones.

LITHOLOGIC LOG
EAST MESA WELL # 58-30

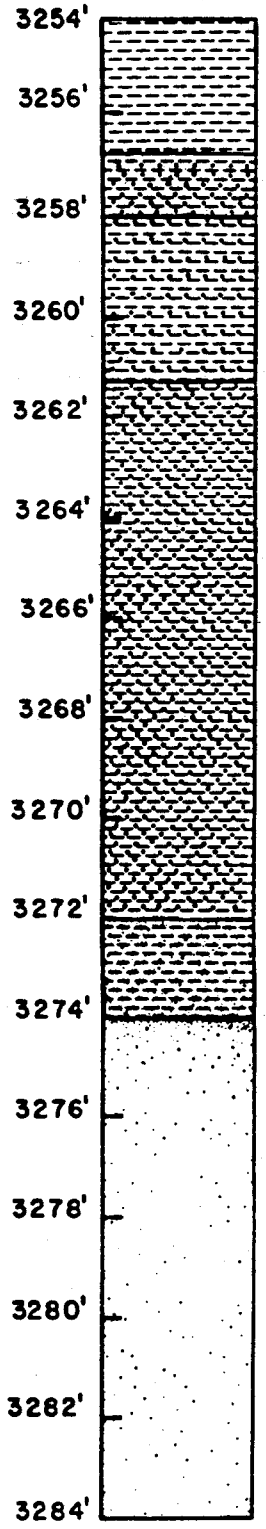

DESCRIPTION

MEDIUM TO DARK GRAY CLAYSTONE; Poor fissility, slight conchoidal fracture.

LIGHT MEDIUM GRAY SILTSTONE; Soft, thinly laminated, very fine grained

LIGHT GRAY/DARK GRAY LAMINATED SILTSTONE / CLAYSTONE; Soft, very fine grained.

MEDIUM GRAY SILTSTONE; Very well sorted coarse silt, soft, very poorly lithified.

GRADATIONAL CONTACT

MEDIUM GRAY SANDSTONE; very well sorted, very fine grained, subrounded to round, mostly quartz, with a trace of dark minerals, soft, friable, poorly lithified.

Figure 6. Lithologic log of East Mesa well #58-30 from which caprock material was obtained for this program.

LITHOLOGIC LOG
EAST MESA WELL #78-30RD

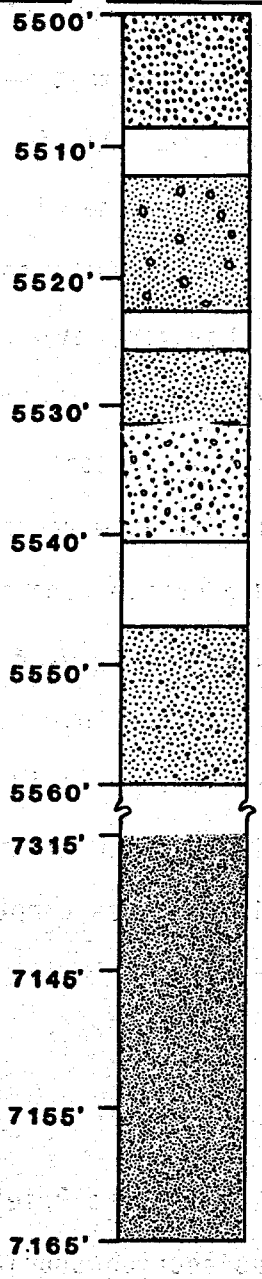

DESCRIPTION

SANDSTONE FINE GRAINED, MOSTLY QUARTZ, SLIGHTLY CALCAREOUS, MEDIUM HARD, GRAY.

MISSING SECTION

SANDSTONE FINE TO MEDIUM GRAINED, MOSTLY QUARTZ, FEW DARK MINERALS, MEDIUM HARD, BROWNISH GRAY.

MISSING SECTION

SANDSTONE VERY FINE GRAINED, MOSTLY QUARTZ, SLIGHTLY CALCAREOUS, WELL CEMENTED , HARD.

SANDSTONE MEDIUM TO FINE GRAINED, MOSTLY QUARTZ, SLIGHTLY FRIABLE, MEDIUM HARD GRAY.

MISSING SECTION

SANDSTONE VERY FINE GRAINED, WELL SORTED, WELL CEMENTED, CALCAREOUS, HARD, GRAY.

SANDSTONE VERY FINE GRAINED TO FINE, WELL SORTED, MOSTLY QUARTZ, WITH FEW PERCENT DARK MINERALS, FAIRLY WELL CEMENTED, MEDIUM HARD TO HARD, GRAY.

Figure 7. Lithologic log of the East Mesa well #78-30 from which reservoir material was obtained for this program.

blue epoxy and one stained for calcite. A mineralogical analysis obtained from these thin sections is given in Table 1. Representative photographic examples of these thin sections are shown in Figures 8a and b. Note the difference in grain size between the overlying claystone and the sandstone of the production zones. As can be seen from Table 1, the porosity in the reservoir material from well #78-30 ranges from about 16 to 28% and most sections are medium to fine grained sandstones with quartz content generally in excess of 70%. Cementation is mostly silica with some calcite. Clay mineral content is small to moderate. The silica cementation and quartz overgrowths that are evident give some evidence of hydrothermal activity; however, evidence of extremely high-temperature alteration is sparse in these rocks. The caprock material from well #58-30 is fine-grained with very high clay content.

Specific fluid and downhole condition data for well #78-30 were obtained from Dr. Donald Michaels of Republic Geothermal, Inc. Production zone temperature is in the range 165-175°C which is a moderate temperature for a hydrothermal reservoir and is consistent with our observation in the thin sections of a relative lack of products of high-temperature alteration. A fluid composition of water from the production zone in this well is given in Table 2. The total dissolved solids content of this water is fairly low as compared to other wells in the Imperial Valley geothermal areas. However, it is within the normal range of variation in the East Mesa area.

2.3 Cerro Prieto

Location of wells from which core was obtained in the Cerro Prieto geothermal field are shown in Figure 9. A schematic cross-section showing core depths is given in Figure 10. A total of 40 feet of core from the Cerro Prieto field was kindly provided by Ing. Alfredo Mañón M. and his associates

Table 1

East Mesa Mineralogy

Classification	Well and Sample No.	Grains (% of Total)												Matrix (% of Total)						Cement (% Total)			Porosity (%)	Roundness (Powers, 1953)	Sorting	Quartz Overgrowths (Yes or No)	Mean Grain Dia. (mm)
		Undulose Qtz.	Non-Undulose Qtz	Composite Qtz.	Plagioclase	Orthoclase	Microcline	Biotite	Muscovite	R.F. Chert	R.F. Shale	Epidote		Clay Minerals	Pyrite	Hematite	Organic Matter			Calcite	Silica	Hematite					
Very Fine Grained Sandstone	78-30 A-4	75	-	-	2	-	1	T	T	2	-	T	-	6	-	1	-	-	-	3	5	-	16.4	Angular to Subangular	Mod. Well	Yes	.098
Fine Grained Sandstone	78-30 A-13	68	-	1	8	1	3	-	T	1	-	T	-	4	-	1	-	-	-	2	8	-	22.3	Subangular to Subrounded	Poorly	Yes	.15
Fine Grained Sandstone	78-30 A-31	65	-	1	10	1	2	T	T	2	-	T	-	5	-	1	-	-	-	1	6	-	26.1	Subangular to Subrounded	Poorly	Yes	.20
Medium Grained Sandstone	78-30 A-38	65	-	2	1	-	3	-	T	4	T	T	-	3	-	T	-	-	-	2	8	-	26.8	Subrounded to Rounded	Mod. Well	Yes	.39
Medium Grained Sandstone	78-30 A-45D	62	-	3	4	T	T	T	-	6	-	2	-	2	-	1	-	-	-	2	8	-	28.9	Subangular to Angular	Poorly	Yes	.30
Fine Grained Sandstone	78-30 BM-1	64	-	3	5	-	1	T	T	8	-	T	-	6	-	T	-	-	-	1	3	-	20.7	Angular to Subangular	Mod. Well	Yes	.15
Fine Grained Sandstone	78-30 BM-2	68	-	2	3	1	3	T	T	7	-	T	-	5	-	T	-	-	-	1	3	-	22.7	Subangular to Subrounded	Mod. Well	No	.19
Claystone	58-30 C-5	9	-	-	-	-	-	1	T	-	-	T	-	79	-	-	1	-	-	5	5	-	18.7	Subangular to Subrounded	Poorly	No	.01
Claystone	58-30 C-10	9	-	-	-	-	-	1	T	-	-	T	-	79	-	-	1	-	-	5	5	-	18.4	Subangular to Subrounded	Poorly	No	.01
Coarse to Medium Siltstone	58-30 C-14	47	-	T	3	T	-	1	T	-	-	T	-	10	10	3	-	-	-	10	5	3	21.5	Subangular	Well	No	.03
Claystone	58-30 C-22	8	-	-	-	-	-	-	1	-	-	T	-	80	-	-	1	-	-	5	5	-	17.1	Subangular	Poorly	No	.013

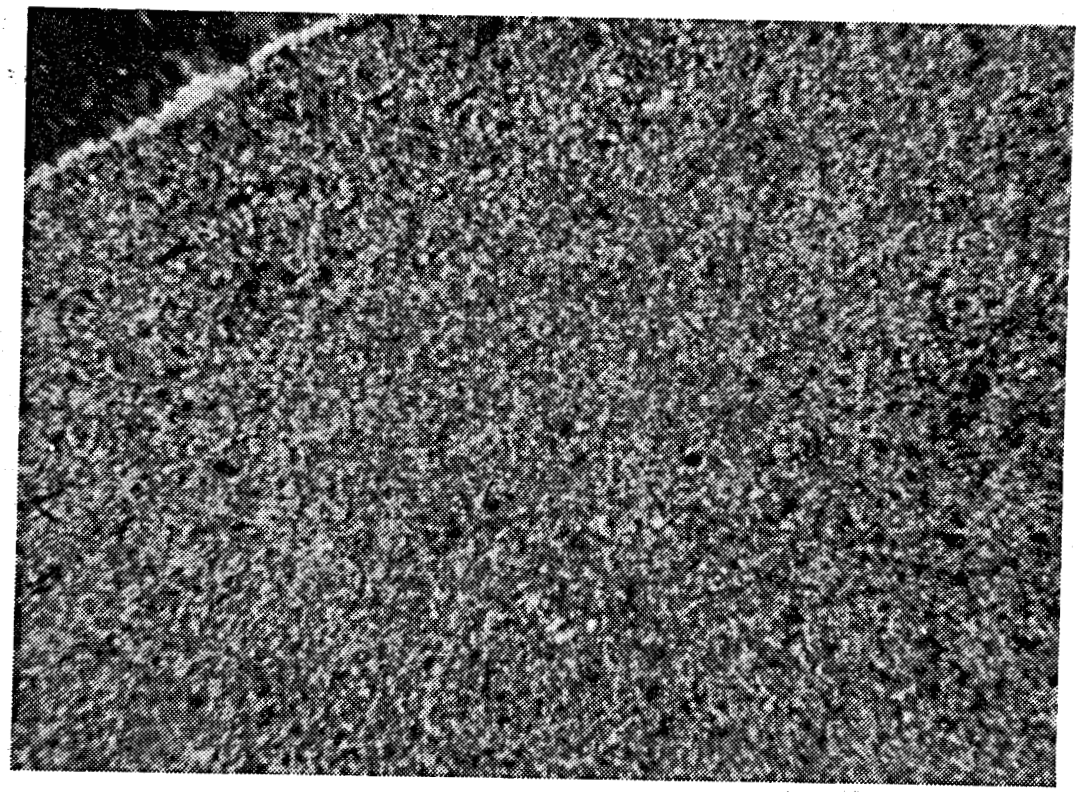

Figure 8a. Photomicrograph of fine-grained claystone material from caprock in East Mesa well 58-30. Magnification is 100x.

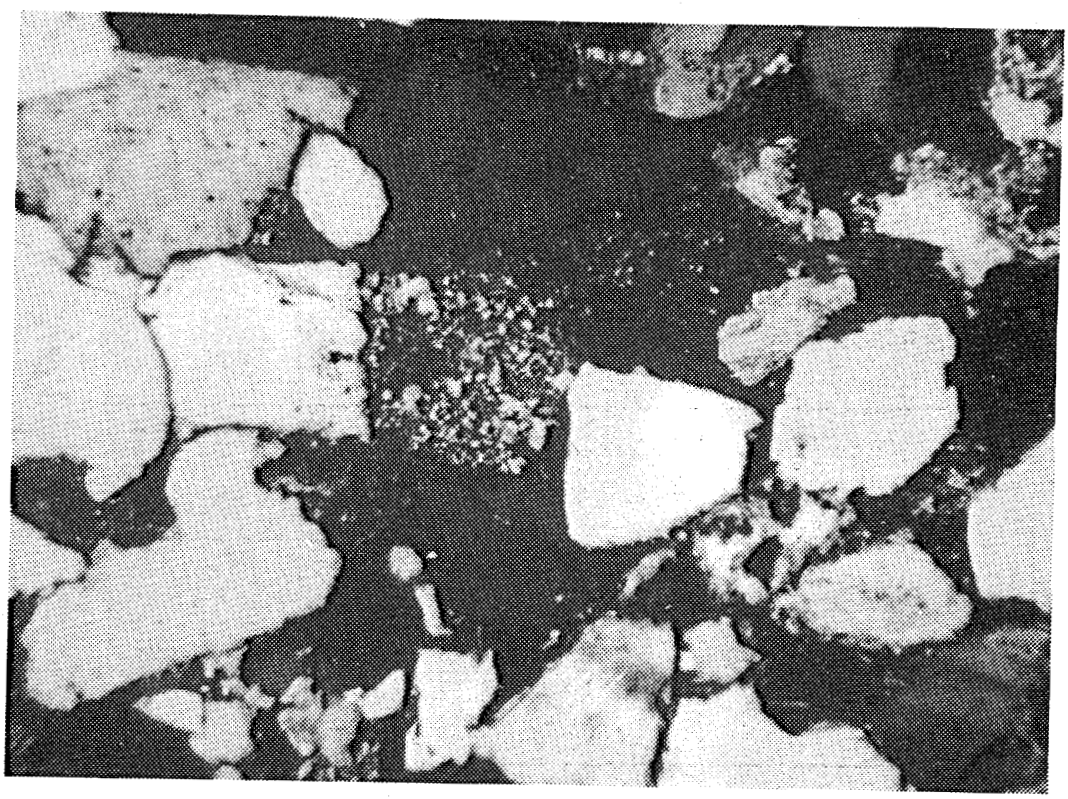

Figure 8b. Photomicrograph of fine- to medium-grained sandstone material from reservoir depth in well 78-30. Magnification is 100x.

Table 2

East Mesa Brine Composition
Well 78-30

Constituent	
pH	6-7
Ca	9 ppm
Na	510
Cl	420
K	25
SiO_2	170
HCO_3	420
SO_4	150
TDS	1700-2400

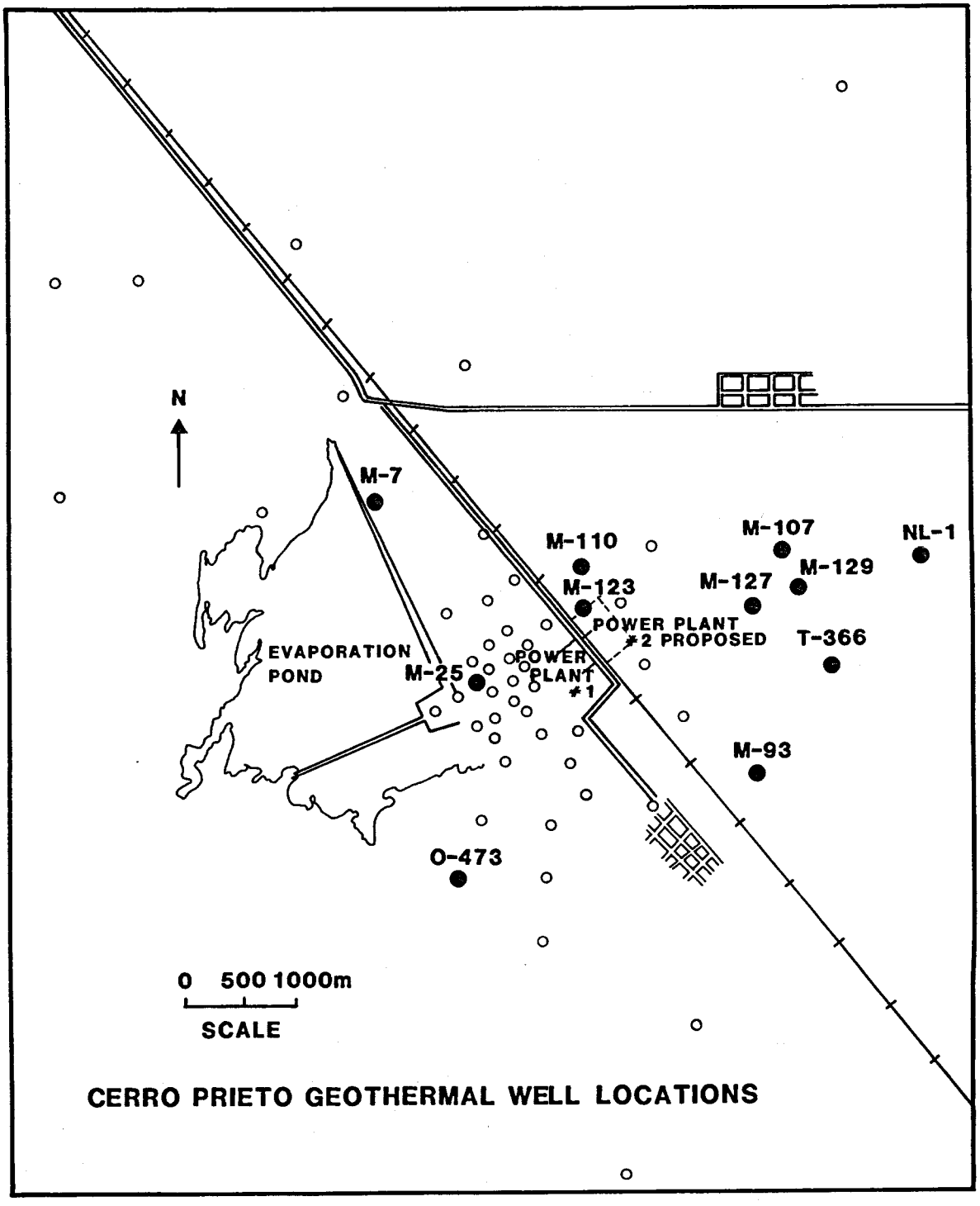

Figure 9. Map of Cerro Prieto geothermal well locations showing wells for which core was obtained for this program.

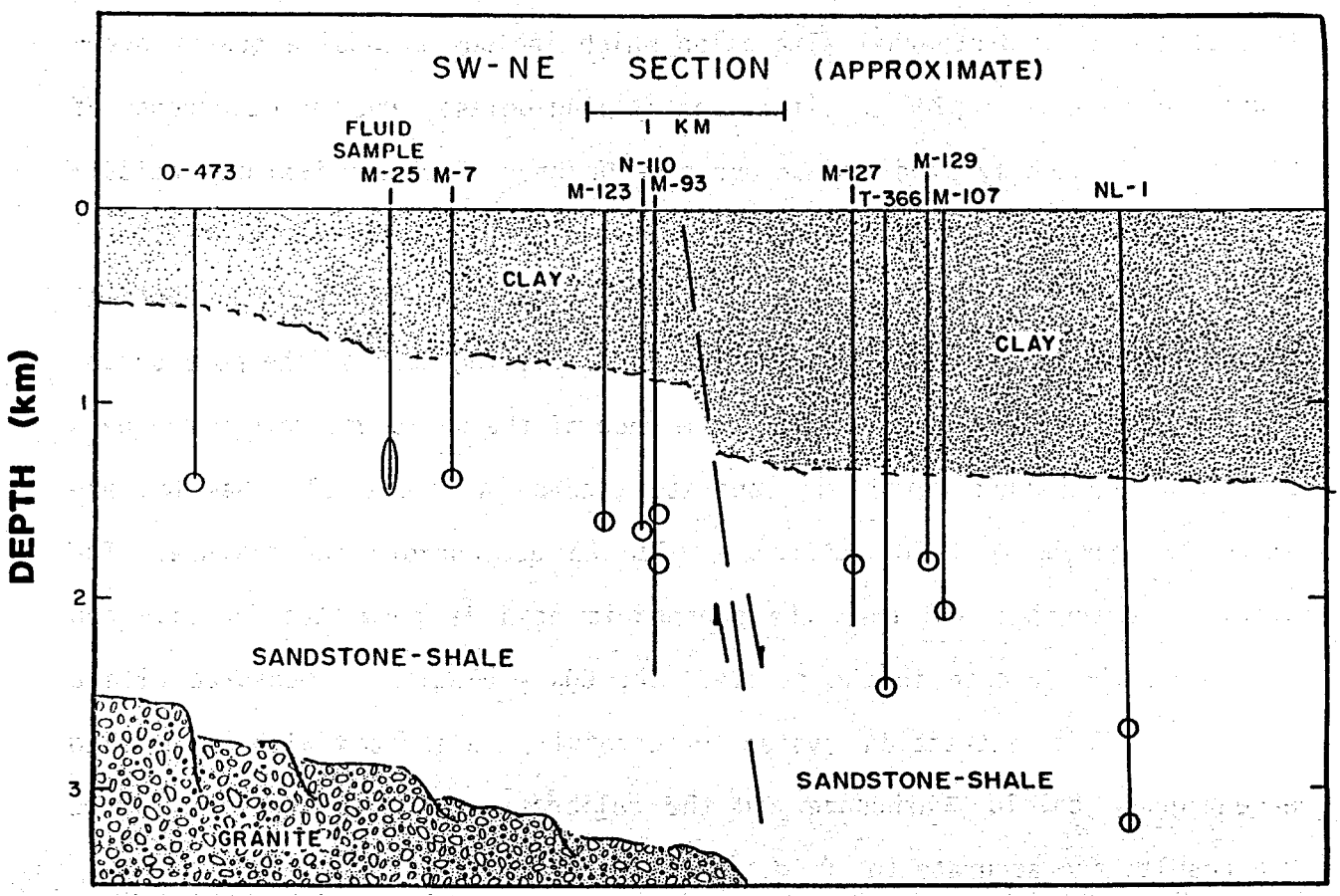

Figure 10. Schematic cross section of Cerro Prieto geothermal field showing approximate depth from which core was obtained for this program.

at the Comision Federal de Electricidad. Specific well designations and depths are given in Table 3. Thin sections were prepared from the core obtained and mineralogical results are given in Table 4. Some representative micrographs are shown in Figures 11a, b, c and d. These rocks are, in general, fine to medium-grained sandstones with quartz contents in the range 60-70% and porosities in the range of 15-30%. These rocks show many characteristics attributable to hydrothermal alteration which include extensive quartz overgrowths, presence of epidote, alteration of plagioclase, and the occurrence of chlorite. Frequently, the quartz overgrowths have a sutured texture indicating that they are authigenic and not relics from a previous depositional cycle. Perhaps the best evidence of hydrothermal alteration is the abundant epidote, shown in several of the photographs, filling much of the pore space.

The calcite content of samples from each of the wells was determined by a CO_2 evolution method using the apparatus shown in Figure 12. Samples are placed in phosphoric acid and frozen with an acetone-dry ice mixture. The system is evacuated and then the phosphoric acid is permitted to thaw and react with the calcite in the sample. The CO_2 evolution is measured with a manometer. This extraction system is carefully calibrated with oven-dried reagent-grade calcium carbonate and the calibration line is shown in Figure 13. Results are accurate to ±0.5%.

The calcite contents as determined fall into three categories and are shown in Table 5. Wells M107, M110, M127, NL1 and T366 have essentially zero calcite. Wells M7, and 0473 have approximately 1% calcite, and wells M93 and M129 have approximately 6-8% calcite. Elders, et al. (1978) have shown that the calcite content of Cerro Prieto rock correlates quite well with temperature boundaries in and near to the reservoir. Rocks with no calcite represent the hydrothermal reservoir itself in which calcite has been decomposed and

Table 3

Core Obtained from Cerro Prieto

Well	Depth (ft)
M-7	4600
M-93	5100, 5900, 6400, 7800
M-107	5300, 7000
M-110	5400
M-127	6100, 7100
M-129	5300, 5900
NL-1	9000, 10,500
O-473	4500
T-366	8200

Table 4

Cerro Prieto Mineralogy

Classification	Well No.	Grains (% of Total)											Matrix (% of Total)					Cement (% Total)			Porosity (%)	Roundness (Powers, 1953)	Sorting	Quartz Overgrowths (Yes or No)	Mean Grain Dia. (mm)
		Undulose Qtz.	Non-Undulose Qtz	Composite Qtz.	Plagioclase	Orthoclase	Microcline	Biotite	Muscovite	R.F. Chert	R.F. Shale	Epidote	Clay Minerals	Pyrite	Hematite	Organic Matter		Calcite	Silica	Hematite					
Very Fine Grained Sandstone	T-366	66	-	-	5	T	2	T	-	-	-	12	-	5	-	-	1	-	-	-	5	-	20	Subangular to Subrounded	Mod. Well	Yes	.06
Very Fine Grained Sandstone	O-473	72	-	T	2	1	5	-	T	-	3	5	-	-	-	1	-	-	-	-	8	-	23	Subangular to Subrounded	Mod. Well to Poorly	Yes	.01
Medium Grained Sandstone	M-7	58	-	1	5	2	3	T	-	T	-	1	-	14	-	T	3	-	-	4	6	-	19	Rounded to Subrounded	Mod. Well	Yes	.35
Very Fine Grained Sandstone	M-93	58	-	-	3	2	-	2	-	-	-	T	-	10	-	-	4	-	-	15	3	-	39	Angular to Subangular	Mod.	Yes	.03
Coarse Grained Siltstone	M-107	51	-	-	2	-	-	T	-	-	-	15	-	20	-	-	3	-	-	-	5	-	25	Angular to Subangular	Mod.	Yes	.04
Fine Grained Sandstone	M-110	68	-	T	3	2	10	T	-	-	-	1	-	8	-	T	2	-	-	-	3	-	15	Subrounded	Mod. Well	Yes	.19
Fine Grained Sandstone	M-127	66	-	T	2	2	3	T	-	T	-	10	-	5	-	-	3	-	-	-	5	T	17	Angular to Subrounded	Poorly	Yes	.15
Coarse Grained Carbonaceous Siltstone	M-129	56	-	-	2	T	T	-	-	T	-	4	-	12	-	-	5	-	-	15	2	-	17	Subangular to Subrounded	Mod. Well	Yes	.05
Fine Grained Sandstone	NL-1	49	-	T	7	4	7	-	-	T	-	6	-	15	-	-	-	-	-	-	6	-	18	Subangular to Rounded	Mod. Well	Yes	.13

Figure 11a. Photomicrograph of thin section from Cerro Prieto well M-110. Magnification is 60x.

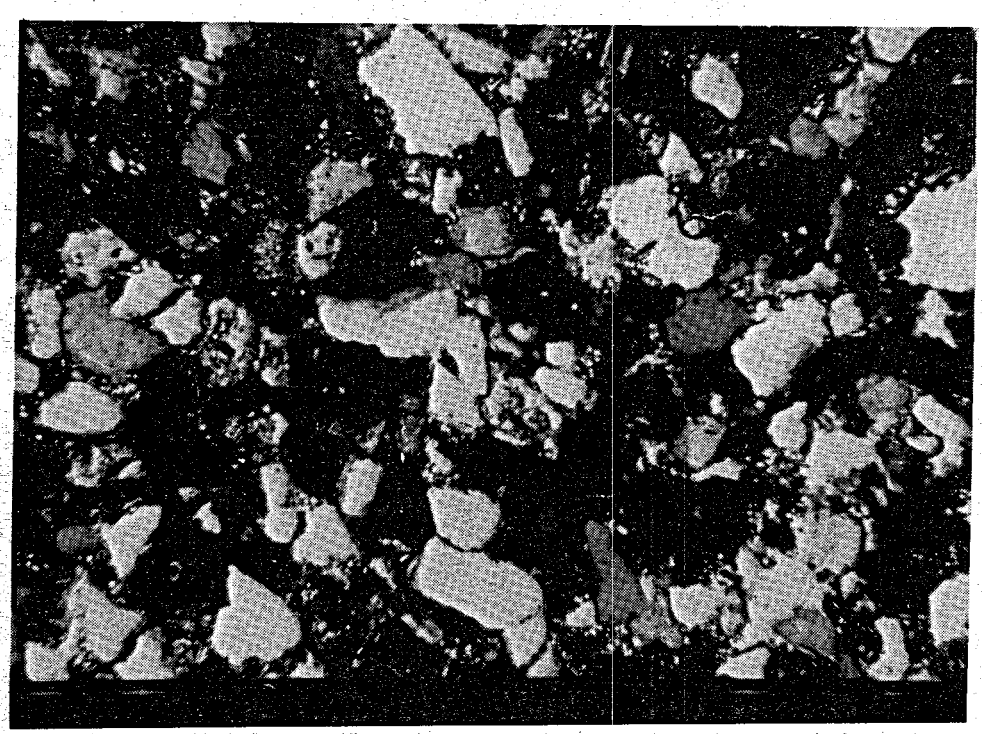

Figure 11b. Photomicrograph of thin section from Cerro Prieto well E-366. Magnification is 60x.

Figure 11c. Photomicrograph of thin section from Cerro Prieto well M-7. Magnification is 60x.

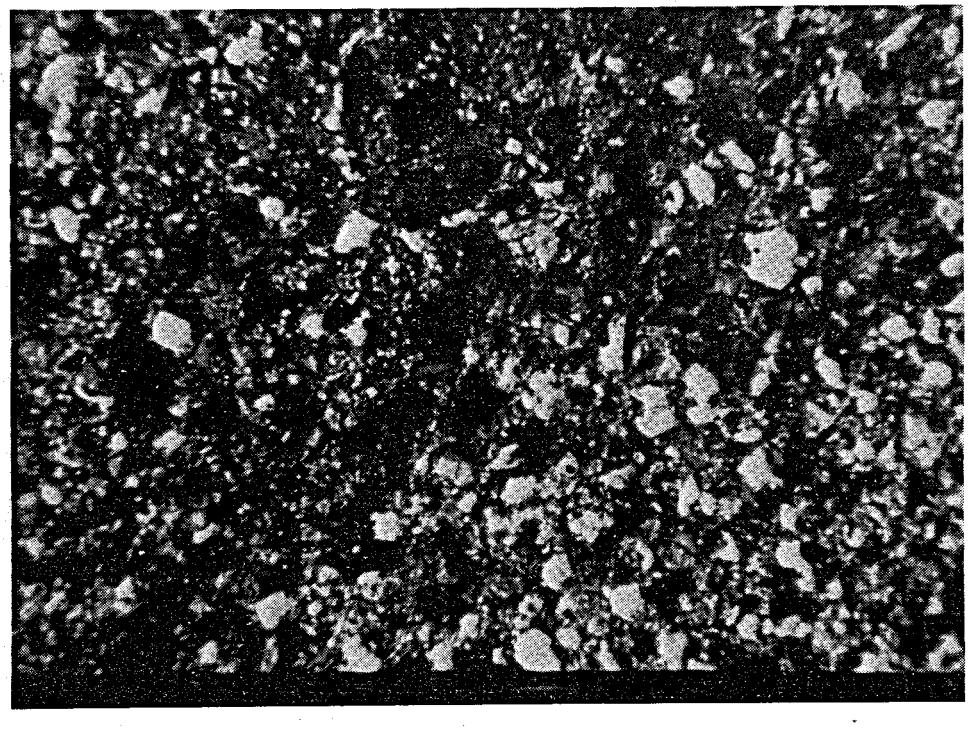

Figure 11d. Photomicrograph of thin section from Cerro Prieto well M-93. Magnification is 60x.

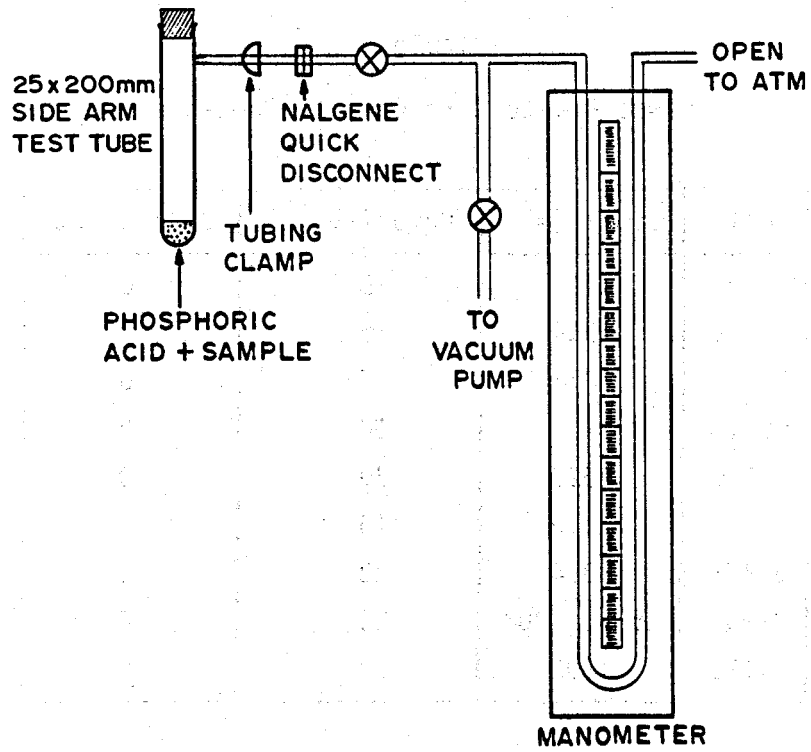

Figure 12. Apparatus for determination of calcite content by carbon dioxide evolution.

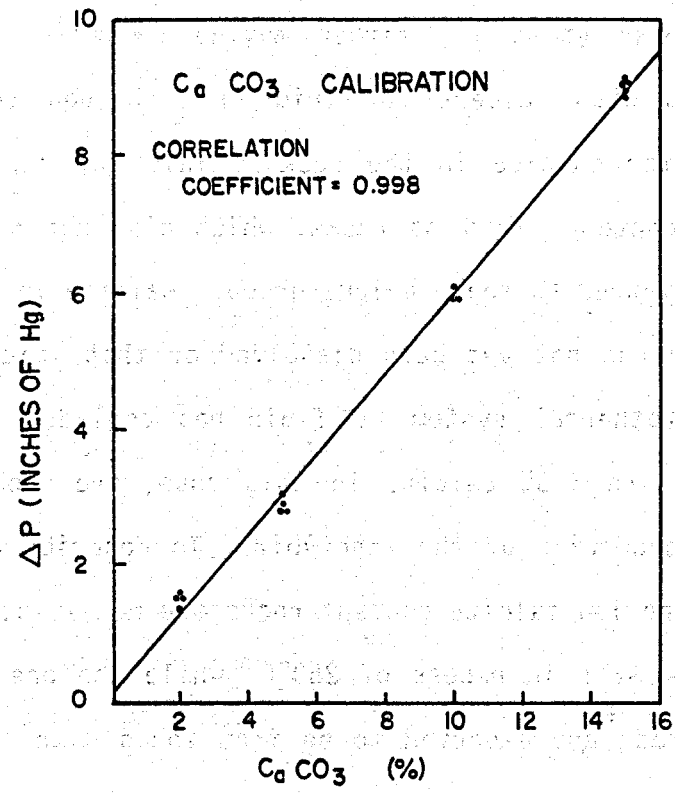

Figure 13. Calibration of carbon dioxide evolution apparatus showing the accuracy of method is about ±1/2 percent.

Table 5

Cerro Prieto Core Calcite Contents

Well	Depth (m)	Porosity (%)	Calcite (%)
M-107	2115	25	0
M-110	1644	15	0
M-127	1871	17	0
NL-1	2735	18	0
T-366	2522	20	0
M-7	1410	19	1
0-473	1384	23	1
M-93	1566, 1804	39	6
M-129	1802	17	8

replaced with minerals representative of alteration such as silica and epidote. This likely corresponds to the zero calcite content group of five rocks. With temperature decrease (that is, either moving upward in the reservoir, or moving downstream with respect to fluid flow through the reservoir), one begins to encounter calcite in the rocks. This may correspond to the one percent calcite content group of rocks, which also has somewhat less silica and epidote as compared to the previous group. Calcite in this group could be either that which has not yet been dissolved or that which has been redeposited in the hydrothermal system as fluid has cooled. The third group of rocks, or those with 6-8% calcite in this case, are probably rocks located near the upper boundaries of the reservoir. To describe all groups in terms of temperature, the low calcite content rocks may be expected to be from zones with temperatures well in excess of 250°C, while the one percent or greater calcite content rock are expected to be from zones with temperatures of less than 250°C.

It was not possible to obtain fluid or fluid information from all of the wells from which core was obtained at Cerro Prieto. Therefore, we use an average fluid chemistry as given by Reed (1976) and shown in Table 6. Data on many wells from the area from which fluids have been collected and analyzed indicate that there is not a large variation of these average values in the Cerro Prieto field.

2.4 Summary and Comparison of Cores and Fluids

Table 7 shows a comparison of average properties (values have been averaged from the previous tables) of the cores and fluids obtained from East Mesa and Cerro Prieto. A major difference to note between the rock from East Mesa and the rock from Cerro Prieto is that the East Mesa rock shows considerably less evidence of hydrothermal alteration. That is, there is less authigenic silica, less quartz overgrowth, less epidote, etc. as compared to Cerro Prieto material. Porosities and grain diameters, however, are similar, although there is possibly a trend to lower porosity for the Cerro Prieto rocks. This could be caused by the greater depth and greater degree of alteration in most of the rock that we have obtained from Cerro Prieto as compared to East Mesa. However, it should be pointed out that wells 78-30 and 58-30 are in the relatively cooler northern portion of the East Mesa reservoir and that more hydrothermal alteration may be present in other parts of the reservoir. The reservoir fluid that is typical of Cerro Prieto contains a higher content of dissolved solids than the fluid that we have obtained from East Mesa. However, this difference is not necessarily present for all of the fluids from the East Mesa and Cerro Prieto reservoirs.

A comparison of typical reservoir temperatures for Cerro Prieto and East Mesa is shown in Figure 14. Also plotted is the boiling point versus depth curve for a two percent NaCl solution. Note that the Cerro Prieto reservoir

Table 6

Cerro Prieto Brine Composition, Average

Constituent	
pH	5-6
Ca	370 ppm
Na	5,100
Cl	9,700
K	1,100
SiO_2	540
HCO_3	1,800
SO_4	20
TDS	15,000-20,000

Table 7

Average Properties of Cores and Fluids Obtained
From East Mesa and Cerro Prieto
(Minerals Given as Percent of Solids)

	East Mesa	Cerro Prieto
Quartz	75	65
Feldspar	7	10
Rock Fragments	6	10
Clays	5	10
Cement:		
Calcite	2	1
Silica	5	7
Epidote	-	7
Porosity	23%	21%
Fluid TDS	2,000 ppm	20,000 ppm
Reservoir Temperature	165°C	300°C

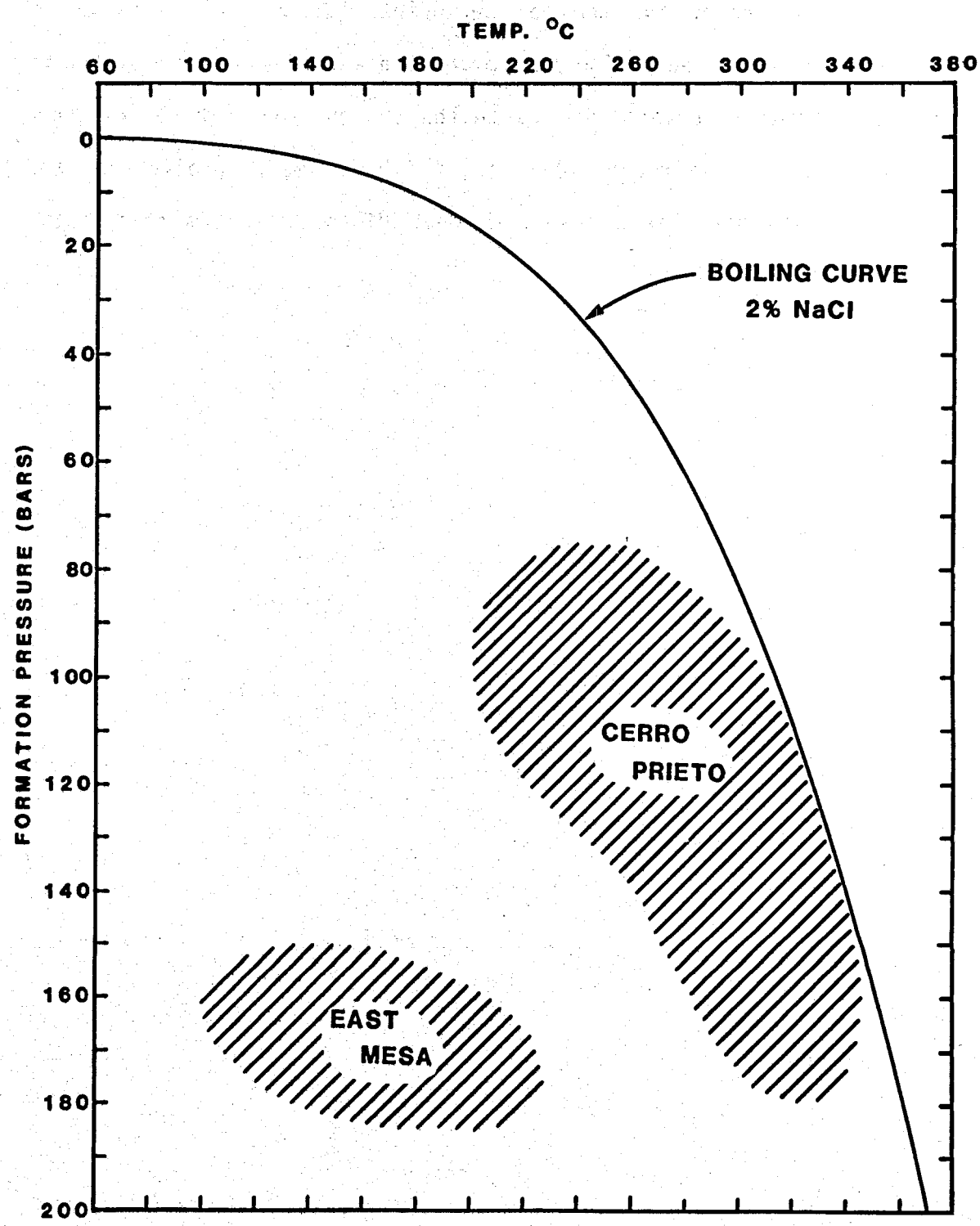

Figure 14. Approximate temperature ranges in the East Mesa and Cerro Prieto geothermal reservoirs. Shown for comparison is a boiling point versus depth curve for a two percent sodium chloride solution. Note that the Cerro Prieto reservoir is very near to or at the boiling point while the East Mesa reservoir is substantially away from the boiling point.

is at, or much nearer to, the boiling point. In general, rock and fluid compositions investigated during this program are representative of the hydrothermal/geothermal reservoirs in the Salton Trough area. There are, however, exceptions such as the Heber reservoir, which is less consolidated, and the Salton Sea Geothermal Field reservoir near Niland which is much higher in dissolved solids content.

3. TESTING EQUIPMENT AND PROCEDURES

3.1 General Information

Most of the equipment used for this program has been developed over a period of years at Terra Tek for purposes of testing at simulated in-situ conditions. In general, confining pressures of 60,000 psi, pore pressures of 30,000 psi, axial stresses of 150,000 psi (on two inch diameter specimens) and temperatures to 300°C, can be handled routinely. In special cases, more extreme conditions can be simulated. Fluids can be light acids, brine, or alkalis, and in special cases, stronger acids or alkalis and heavier brines. Some new equipment development was undertaken as part of this program to modify a test machine to be able to sustain constant test conditions for periods of weeks for the purpose of the creep measurements. In the following sections, test procedures and equipment will be described in the major categories of preliminary sample handling, basic testing, creep testing, fluid chemistry, and microstructural analysis.

3.2 Preliminary Sample Handling

The first step in sample handling was the acquisition of core. For East Mesa, a Terra Tek team was at the well site during coring and core was wrapped and preserved in a fresh state, boxed and shipped. Upon receipt at Terra Tek, core was logged in and kept preserved until time for testing. It was likely, therefore (aside from unknowns associated with the transport of core up the wellbore while in the core barrel and removal from the core barrel), that core from East Mesa was tested in an undisturbed state. For Cerro Prieto, core was selected from shelves at the storage warehouse at the geothermal field. With little exception, the core available had been stored dry on the shelf for a period of months to years. It was boxed and shipped to Terra Tek. Upon

receipt at Terra Tek, it was logged in and saved for testing. There were, therefore, unknown possibilities of sample handling disturbance and, due to drying, clay alteration in the Cerro Prieto material. However, the relatively small amount of clays in these materials and the stability of the products of hydrothermal alteration at room temperature lead us to feel confident that the Cerro Prieto material was received in a testable condition. As a check, some comparison tests for Cerro Prieto material were made on a small quantity of core that had been preserved, and resaturated core that had been previously dried. No discernible differences aside from normal random variations were seen in the mechanical properties results from these tests.

The test program for this project was designed to emphasize tests on sands from production zones, as these would see the greatest pore pressure decrease and probably have the greatest tendency to compact. A few shales from bounding zones were also selected to see if dewatering phenomena were detectable. Therefore, approximately 90% of the materials to be tested for this program were fine- to medium-grained reservoir sands. Approximately 10% of the materials selected were shales, clays, or silts.

To start, small pieces of material were chipped or cut off from cores near to the locations where test samples were to be cut. With these pieces, a wet density, a dry density, and a grain density were determined by immersion and gas pycnometer techniques. From these values, a porosity for each specimen was determined. Results are given later in the section on test results. Also, from similar pieces, samples were prepared for thin section and scanning electron microscope analyses. The thin section preparations were either conventional impregnations, blue stain impregnations for porosity determinations, or red stain impregnations for calcite determinations. The SEM specimens were chipped to provide a fresh tensile surface for viewing.

Samples for in-situ condition testing were prepared in the form of right circular cylinders. For basic testing, samples were generally 1-1/2 inches in diameter by 3 inches in length. For creep testing and permeability testing, samples were generally 2 inches in diameter by 4 inches in length. These samples were cut in a water spray and then the ends were ground to provide flat and parallel surfaces within ±0.005 inch. Test specimens were then placed between two cylindrical stainless steel end caps as shown in Figure 15. The end caps had provision for pore fluid connections to the test samples. The samples were encased in tubes of heat-shrinkable teflon and ends were sealed with stainless steel lock wire. The samples were then placed into the appropriate machine for testing. Details of procedures associated with fluid saturation, pore pressure control, and other pressure and temperature controls are described below in the individual section for each test procedure.

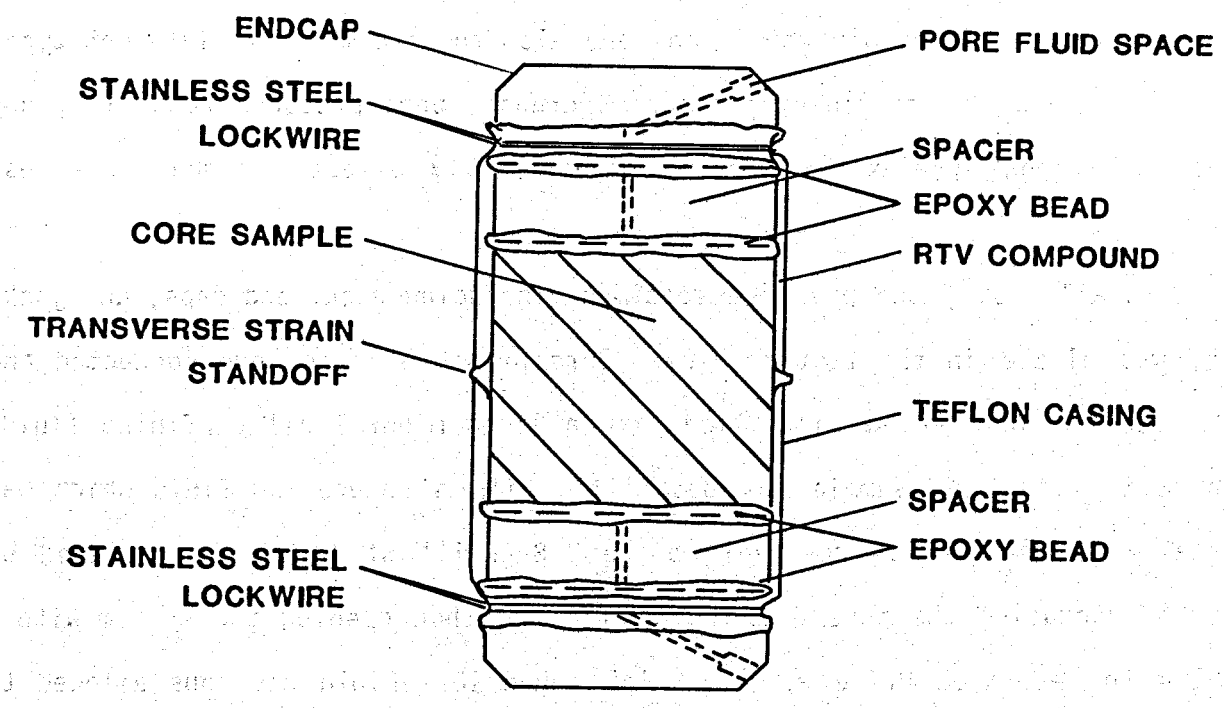

Figure 15. Schematic diagram of assembled test specimen showing sample, endcaps, jacket, and pore fluid connections.

3.3 Basic Testing

Most of the tests in the basic testing category were done on 1-1/2 inch diameter by 3 inch long specimens in the test machine shown in Figures 16 and 17. The machine capabilities are:

- Confining Pressure: 20,000 psi
- Axial Stress: 35,000 psi on a 1-1/2" specimen
- Pore Pressure: 6,000 psi
- Temperature: 175°C
- Specimen Diameter: 3/4" to 3"

This machine is externally heated and uses servocontrolled hydraulic systems for axial load and confining pressure.

The purpose of this part of the testing program was to fully characterize the materials from both reservoirs in terms of basic properties such as compressibility at reservoir conditions and also to determine if different types of testing such as confining pressure increase, pore pressure reduction, and one dimensional (uniaxial) strain, significantly affected comparative test results.

In all tests, the prepared specimen, including rock, end caps, and jacket, was placed in the test machine. Pore pressure lines were connected and the machine was sealed and filled with a light mineral oil confining fluid. In most tests, the sample was backfilled with a saturating fluid which was usually a simulant of reservoir brine. Backfill of fluid was achieved by first evacuating the pore pressure system and then opening the system with a valve to deaerated brine as shown in Figure 18. Fluid was thus allowed to flow back into the core and equilibrate in pressure as it filled the pore space. This has been found to be a consistent and adequate way of achieving

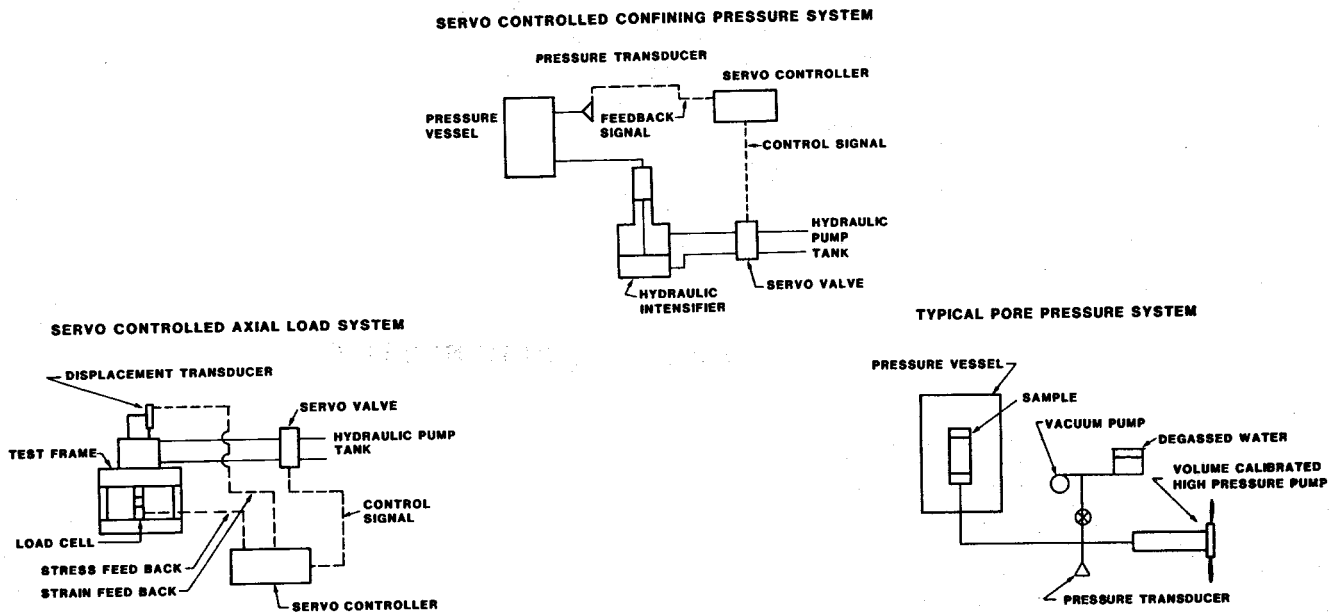

Figure 16. Schematic diagram of the high pressure, medium temperature system used for basic testing.

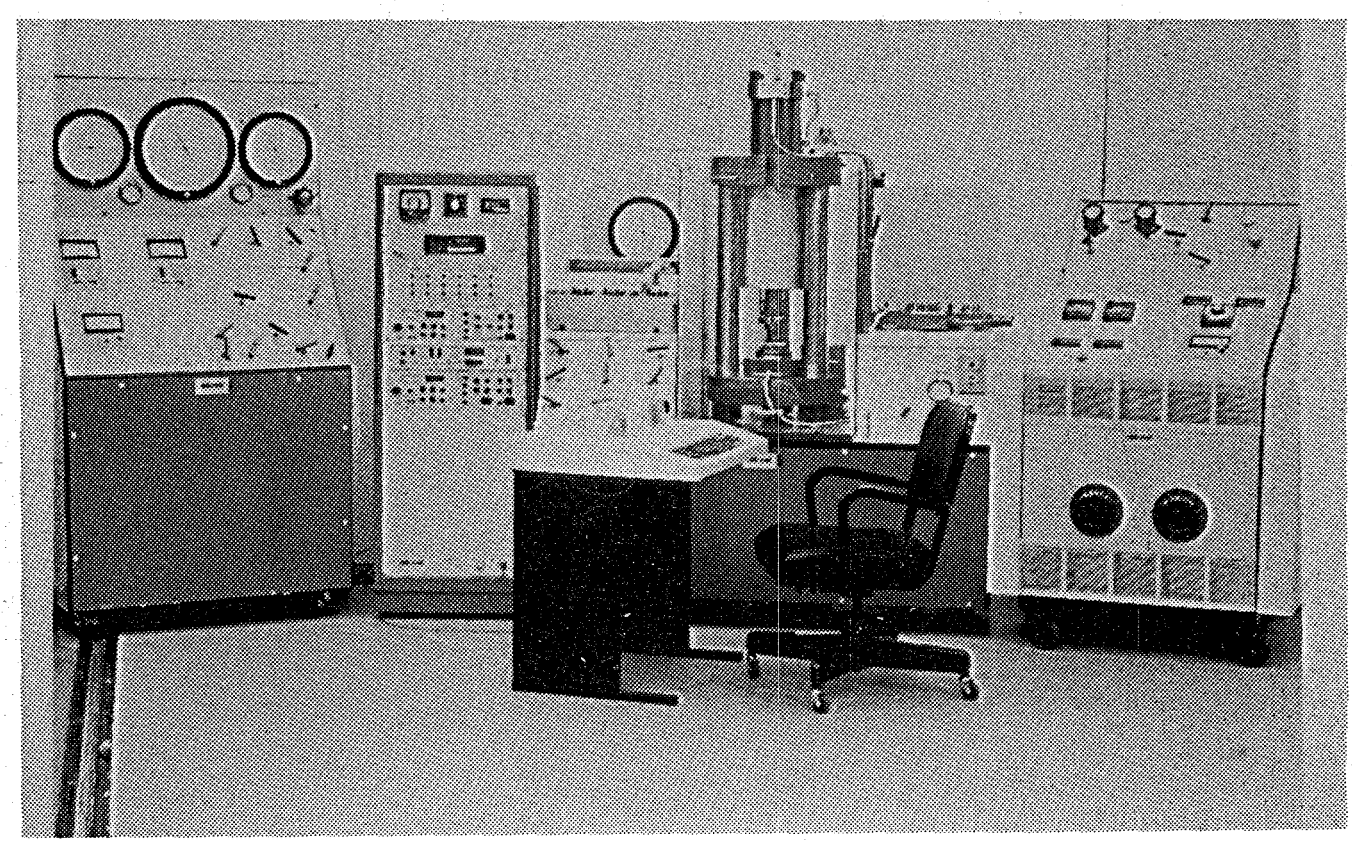

Figure 17. Photograph of system used for basic testing.

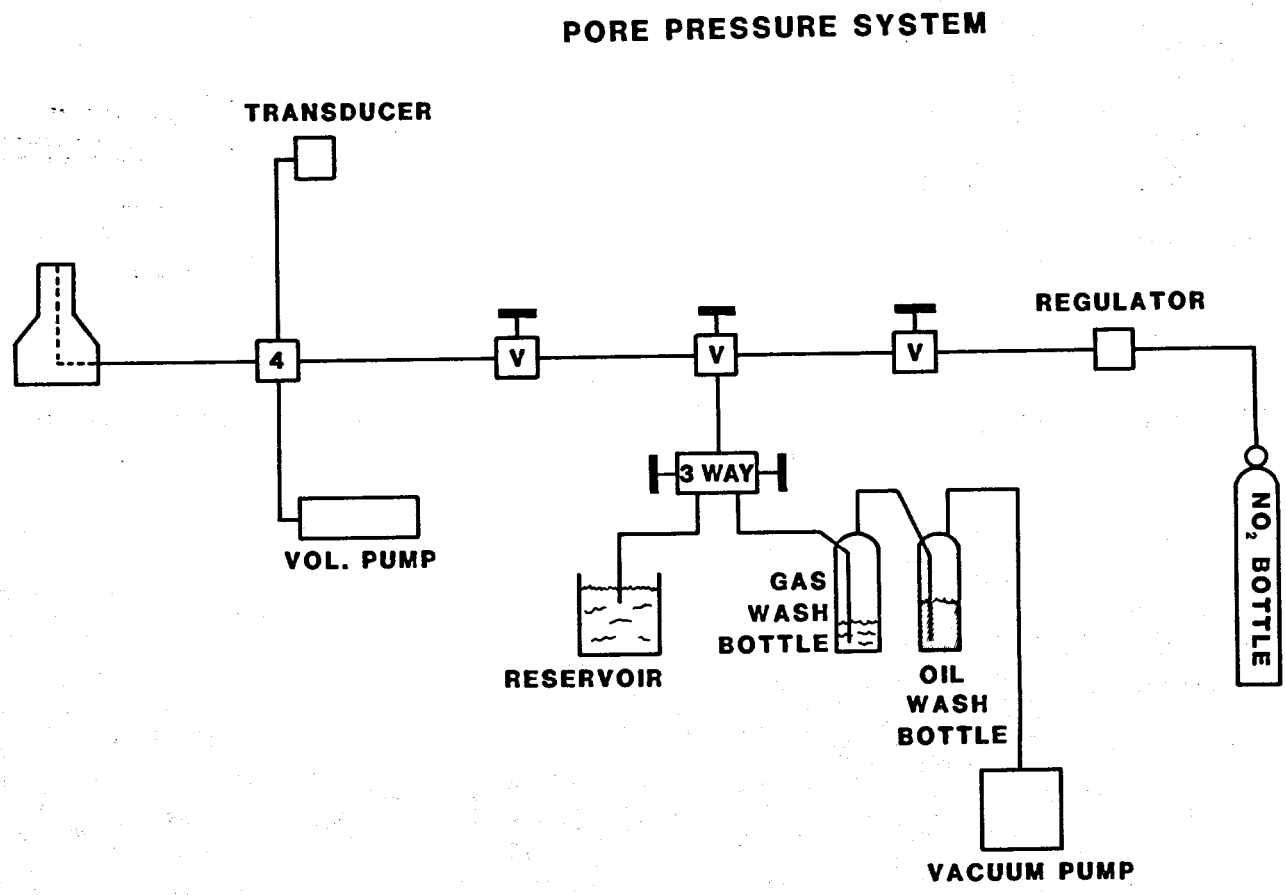

Figure 18. Diagram of pore pressure system used for basic testing.

at least 95% saturation in a material that has a permeability of more than a few millidarcies.

Once prepared in this manner, the specimen was tested. The test system was capable of applying and measuring confining pressure, pore pressure, axial stress, and temperature. Strains were also measured. In this system, both axial and transverse strains were measured by a cantilever system as shown in Figures 19 and 20. This system was calibrated at frequent intervals and was accurate to ±0.001 inch. In this case, this accuracy corresponds to a few hundredths of one percent strain or a volume strain of about one-tenth of one percent. Load, when applied to the specimens to create axial stress, was via a piston directly contacting the upper end cap. Load was measured by a strain-gaged load cell which was also frequently calibrated. The specific types of tests that were run are:

3.3.1 Drained and Undrained Hydrostatic Compression (Isotropic Compression)

Initial tests were run at room temperature. Specimens were prepared, saturated as described above, and then confining pressure was increased to approximate reservoir conditions. In some tests, during confining pressure increase, fluid was allowed to drain from the specimen at a small constant pore pressure. This test, termed a "drained test", was a measure of the rock skeleton compressibility or reservoir compressibility. In other tests, the pore pressure system was locked off and the pore pressure was allowed to increase as confining pressure was increased. This test, termed an "undrained test", was more nearly a test of rock grain compressibility*. Both of these

*Strictly speaking, only an undrained test where pore pressure equals confining pressure as a measure of grain compressibility. However, when pore pressure is allowed to increase as it will, as in the undrained tests described here, grain compression may be obtained from the difference between drained and undrained test results, provided that fluid compressibility is known.

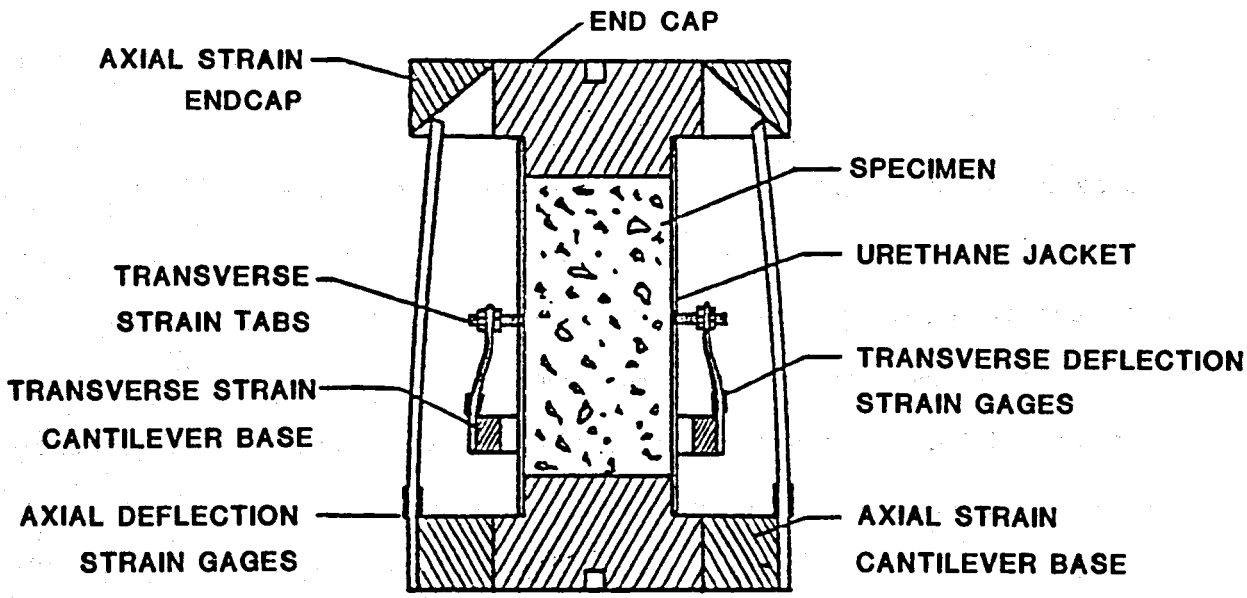

Figure 19. Schematic diagram of test specimen showing axial and transverse cantilever strain transducers.

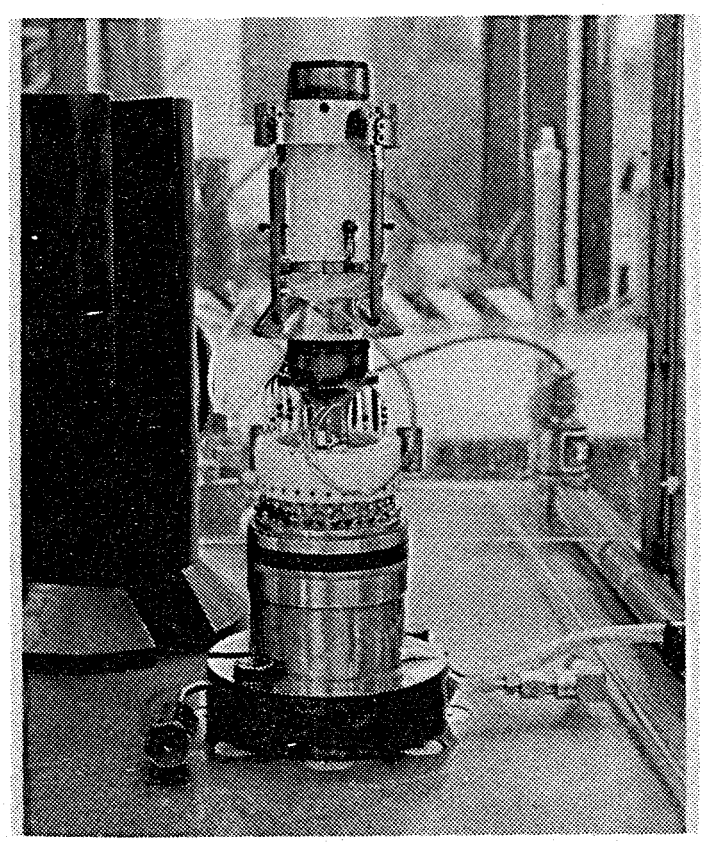

Figure 20. Photograph of assembled test specimen showing strain transducers.

test types were used to determine the appropriate concept of effective stress in these materials. Terra Tek uses the term "hydrostatic compression" for these types of tests. In the soils literature, "isotropic compression" is also sometimes used.

3.3.2 Room Temperature and High Temperature Drained Hydrostatic Compression

Following sample preparation and saturation as described above, drained hydrostatic tests were run on similar materials at both room and elevated temperatures. The purpose of these tests was to determine the effect of temperature variation on the response of these specimens. These results would thus be used to determine the importance of testing at elevated temperatures during the remainder of the program.

3.3.3 Cycling

Some tests were conducted with multiple cycles of pressure increase and decrease. This was to determine the amount of cycling-caused hysteresis and its effect on overall behavior. This could be an important factor for planning of reservoir production that involves alternate cycles of discharge and recharge.

3.3.4 Pore Pressure Reduction

During reservoir production, compaction is triggered by pore pressure reduction and the resulting increase of effective stress. This effect was studied during this program by bringing the rock to approximate reservoir conditions and then reducing pore pressure while measuring specimen compaction. Pore pressure reduction tests, instead of being hydrostatic, were done at appropriate "triaxial" conditions of axial load and confining pressure to approximate actual vertical and horizontal stress conditions in the reservoir.

3.3.5 Uniaxial Strain

For some compaction and subsidence models it is useful to measure, instead of hydrostatic compaction, a compaction that occurs for the case of uniaxial strain, that is, with no change in the transverse dimensions of the specimen. This test is sometimes also called "one-dimensional strain", or in the soils literature, a "consolidation test". Specimens for these tests were brought to reservoir conditions, and then pore pressure was reduced. However, instead of keeping stresses constant while reducing pore pressure, as in the hydrostatic and triaxial tests, the transverse strain and total axial stress were held constant. To do this, it was necessary to continually adjust confining pressure.

3.3.6 Ultrasonic Velocities

In combination with many of the above tests, ultrasonic compressional (P) and shear (S) wave velocities through the specimens were measured as effective stress was varied. This was done for field sonic log correlation and to determine if field-determined sonic velocities could be used as a measure of reservoir compaction.

3.4 Creep Testing

Each test in the basic testing sequence was accomplished in less than one day of machine time (not including set-up). Because of the long-term effects of elevated pressure and temperature, compaction could have significant time dependence that would not be recognized in such a short-term test. For this reason, it was decided to do a number of additional tests at reservoir conditions with pore pressure reduction for extended periods of time, up to several weeks.

To do this, it was necessary to modify a test machine in order to achieve stable conditions for long periods of time. That machine will be described

here. Also, with long-term equilibrium now being considered, great care was taken during these tests to understand the fluid chemistry phenomena that were occurring. As will be seen later, certain changes in fluid chemistry during creep tests were possibly linked to mechanisms of mechanical alteration. Also during this phase of work, permeabilities at reservoir conditions were measured.

The creep testing system, shown schematically in Figure 21 and by photograph in Figures 22 and 23, has the following basic capabilities:

- Confining Pressure: 15,000 psi
- Axial Stress: 60,000 psi on a 2 inch specimen
- Pore Pressure: 6,000 psi
- Temperature: 300°C
- Specimen Size: 2 inches diameter by 4 inches long

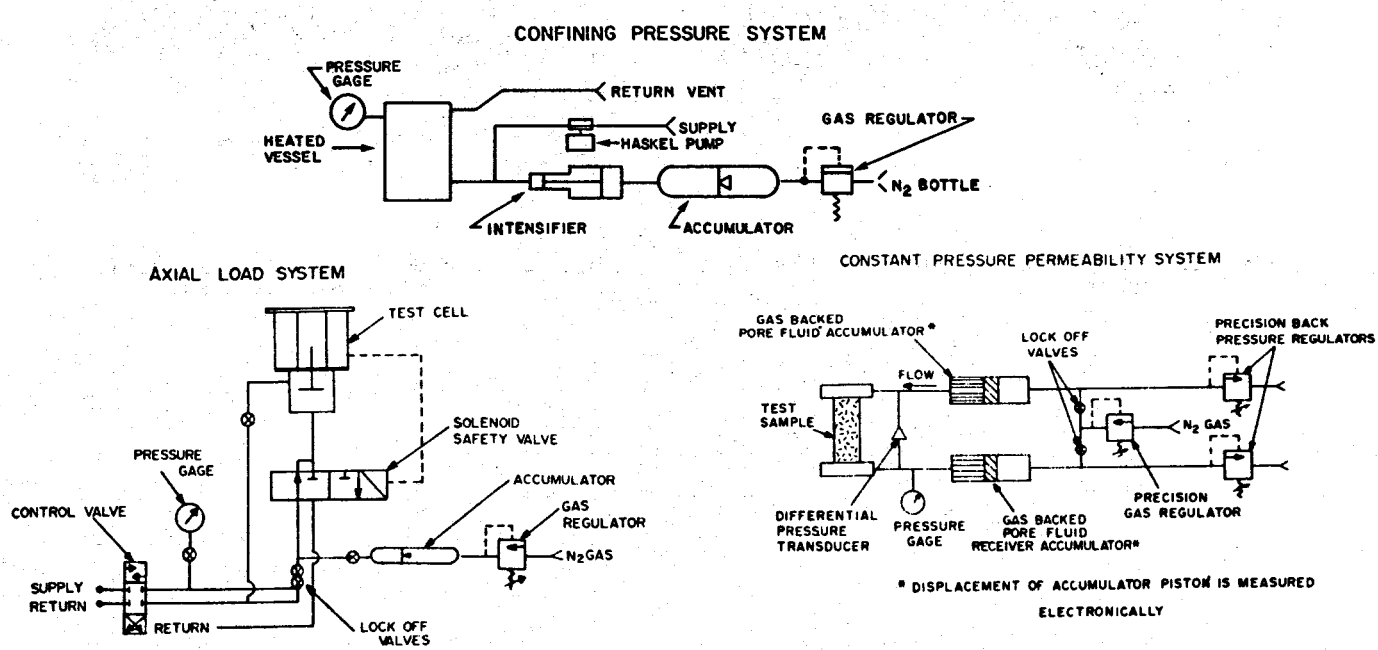

Figure 21. Schematic diagram of high temperature creep testing system. At top is the confining pressure system, at lower left is the axial load system, and at the lower right is the pore pressure/fluid flow system.

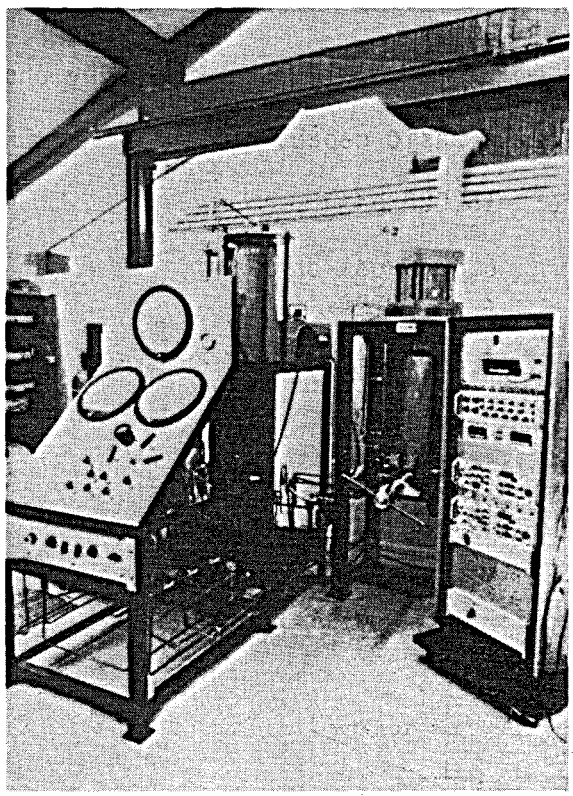

Figure 22. Photograph of high-temperature creep system.

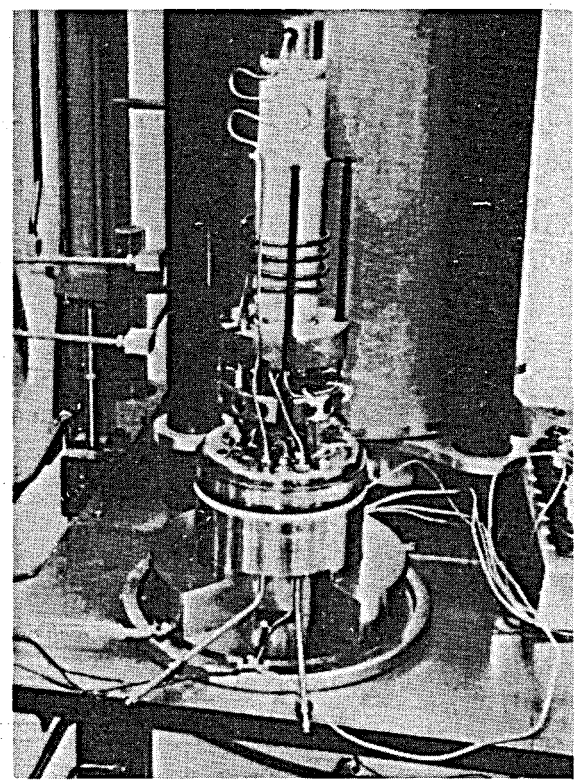

Figure 23. Photograph of sample assembly, for high temperature creep measurement.

The confining pressure system consists of a 15 gallon nitrogen-backed accumulator driving a 4 to 1 intensifier which in turn pressurizes the vessel. The confining fluid used is a light, highly-refined mineral oil that has been optimized for its heat transfer properties. The axial load system uses a 5 gallon nitrogen-backed accumulator to maintain load. The pore pressure system makes use of two 500 cc back-pressure regulated accumulators which maintain pressure or control flow. The test system is internally heated, where the sample is enclosed in a ceramic shroud. Set-up for testing on this system is more time-consuming than for the test machine that was used for basic testing. However, the higher temperatures that were attainable and the stability made it possible to do the creep tests that were necessary for this program.

Confining pressure, load, and temperature were monitored in this system. Additionally, measurements included transverse strain, axial strain, and in some cases, pore volume change. The axial strain measurements were achieved by direct measurement of sample length using two LVDTs (Linear Variable Differential Transformers). These were more accurate and stable than the cantilever system described previously. Sample length could be resolved to approximately ±0.005 inches. Also, on short-term tests, transverse strain measurements were achieved by use of strain-gaged cantilevers as described previously. The resolution of this system was approximately ±0.001 inch. Volume strain of the entire specimen could be resolved to better than 0.1%. Additionally, pore volume change could be measured by an LVDT system mounted on the pore pressure accumulator. A volume change of ±0.05 cm^3 could be resolved. For flow experiments, the differential pressure transducer allowed ±3 psi of differential pressure (across the specimen) to be resolved.

An outline of the creep testing procedure is given in Figure 24. Following acquisition, characterization, and preparation, the sample was placed into

CREEP TESTING PROCEDURE

PRE-TEST PROCEDURE

- ACQUISITIONS OF CORE AND RESERVOIR FLUID
- PHYSICAL AND CHEMICAL CHARACTERIZATION

TESTING SEQUENCE

- PREPARE SAMPLE, PUT IN MACHINE
- COLD FLUSH (PERMEABILITY)
- PRESSURIZE (INITIAL MODULI)
- HEAT SAMPLE
- HOT FLUSH (PERMEABILITY)
- REDUCE PORE PRESSURE
- MEASURE CREEP AS FUNCTION OF TIME
- RECOVER PORE FLUID (PERMEABILITY)

POST-TEST PROCEDURE

- PHYSICAL AND CHEMICAL CHARACTERIZATION

Figure 24. Outline of creep testing procedure.

the test machine. It was then saturated using a backfill procedure as described in the basic testing section. A small amount of confining pressure (usually 100 psi or less) was used at this point to assure intimate contact of jacket and specimen. Saturation was then guaranteed by flowing pore fluid through the specimen. In some cases, permeabilities were measured while fluid flowed through the specimen at these conditions.

Most of the specimens tested had residues of drilling muds and brine solids left in the specimen. To insure that these were all removed from creep test specimens, fluid was flushed through the sample and chemically analyzed at the output until composition of output fluid did not differ significantly from input fluid. It was thus determined that equilibrium had been achieved at low temperature. The sample was then raised to in-situ stress-simulating conditions of confining pressure, pore pressure, and axial load. Care was taken during this loading phase not to exceed the in-situ effective stress. This was achieved by increasing all quantities simultaneously, such that effective stress was monotonically increased to reservoir conditions. This cautious treatment was important, as it prevented pre-cycling of the sample in an unrealistic manner. Once at pressure, the fluid composition was adjusted to the proper chemistry by alteration of its CO_2 content, and the sample was again flushed. In some cases, permeability was again measured. At this point, the sample was slowly and carefully heated to reservoir temperature. Pressures were controlled carefully during this heating to account for thermal expansion effects. More fluid was then flushed through the specimen and in some cases, permeability was measured. Then, the sample was allowed to stabilize until it showed no strain fluctuations as caused by thermal equilibration of the machine.

The initial phase of creep testing took from one to several days to achieve. Then, creep was initiated by quickly lowering the pore pressure by

approximately 1000 psi, therefore simultaneously increasing the mean effective stress by approximately the same amount. During this effective stress increase, a short-term or "elastic" compressibility was determined for comparison with previous results obtained during basic testing. Shortly after creep initiation, another permeability was sometimes measured.

Care was taken to maintain constant stresses and temperature for the duration of the creep period. At the end of the creep period, in many cases, another permeability was measured in order to correlate permeability reduction with creep compaction. Finally, pore pressure was raised to its initial value and a final compressibility, and in some cases, permeability, was determined. A fluid sample was also obtained for chemical analysis. Then the sample was cooled, removed from the machine, and its jacket cut off. Small samples were taken for post-test thin section, and scanning electron microscope analyses.

3.5 Fluid Chemistry

Testing of fluid-bearing reservoir rock, whether it be for geothermal, oil and gas, or water reservoirs, should be done with fluids that are compatible with the rock structure and consistent with in-situ chemistries. The classic example of the validity of this procedural recommendation is the necessity to test a rock containing swelling clays with fluids that are in ionic equilibrium with the clays. Otherwise, non-equilibrium fluids would cause significant permeability and porosity alterations. Less is known about non-equilibrium fluid effects for the case of testing of geothermal reservoir rocks, however, it is certainly true that during long-term creep testing, fluid chemistry and rock-fluid equilibria can potentially affect the chemical and mechanical make-up of these rocks. Furthermore, with control and measurement of fluid chemistry, chemical information can be used to assist in determining the mechanisms of creep.

The objectives of fluid chemistry control and analysis for this program were to minimize chemically-induced rock response during testing procedures and to determine chemical indicators of mechanical creep-compaction mechanisms. To minimize undesired chemical reactions it was necessary to use as pore fluid either an actual geothermal brine or a synthetic brine with the correct composition. Both brine types have been used during this testing program. East Mesa brine was synthesized in the laboratory and Cerro Prieto brine was collected in the field but chemically adjusted in the laboratory to account for changes caused by collection at the depressurized and cooled well head.

To insure that chemical equilibrium was being approximated during testing in the laboratory, it was necessary to periodically sample the pore fluid and analyze it for major constituents. Analyses were performed both in Terra Tek's chemistry laboratory and in the geochemical laboratory at the University of Utah. The sampling procedure used in the laboratory is shown schematically in Figure 25.

The East Mesa brine in the production zone of Well 78-30 tested was of low salinity and silica concentration and easily synthesized in the laboratory. The in-situ brine composition has been estimated and is given in Table 8 along with the composition of the synthetic brine used for testing at Terra Tek. Except for bicarbonate (HCO_3^-) and sulfate (SO_4^{--}), the synthetic and in-situ brine compositions were similar. Bicarbonate was intentionally forced high to compensate for loss of carbon dioxide (CO_2) during storage and to allow for generation of the necessary aqueous CO_2 in the pore pressure system. Aqueous CO_2 was generated by partially filling an accumulator with brine, pressurizing the brine, and then injecting sulfuric acid (H_2SO_4) into the pressurized brine. By controlling the quantity of acid injected, the degree of conversion

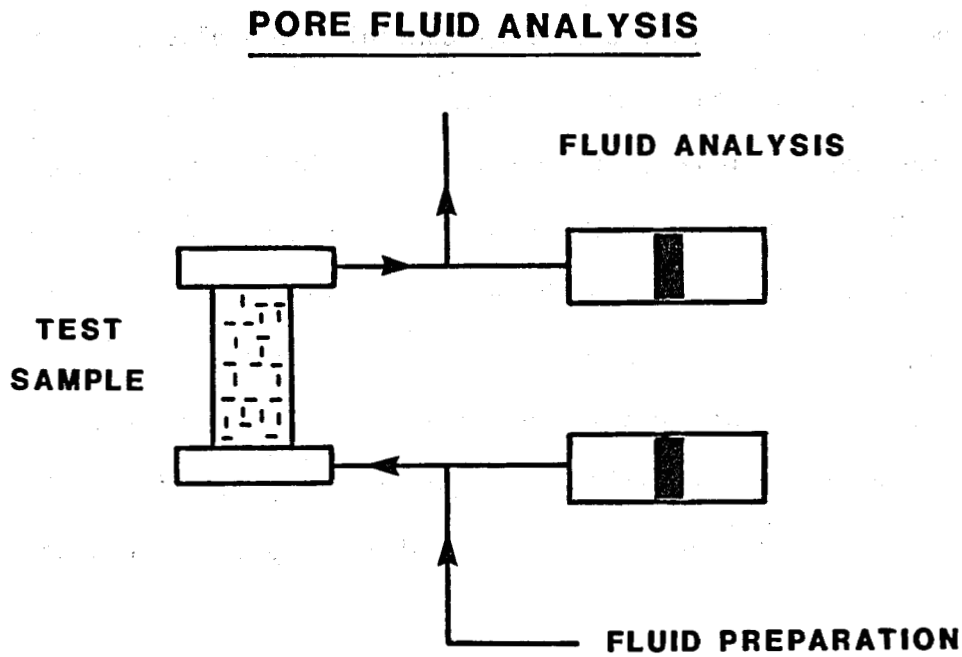

Figure 25. Schematic diagram of pore fluid sampling system used during high temperature creep testing.

Table 8

East Mesa Brine Composition
Well 78-30

Constituent	In-Situ	Synthetic Brine
pH	6-7	5.5 - 6.5
Ca	9 ppm	10 ppm
Na	510	650
Cl	420	350
K	25	30
SiO_2	170	180
HCO_3	420	780
SO_4	150	350
TDS	1700 - 2400	2400

of bicarbonate to carbon dioxide was controlled. The amount of acid required for the conversion also necessitated the originally low sulfate content in the synthetic brine. The procedure followed for this bicarbonate to carbon dioxide conversion is shown schematically in Figure 26. The resulting pH of the brine within a test specimen during testing was estimated to be between 5.0 and 7.0, but it is not actually known since there is no currently reliable method of measuring pH at high pressure and high temperature within a test vessel. Fortunately, in the actual geothermal reservoir, pore fluid pH is probably controlled by the amount of carbonate species present rather than the converse, i.e., the bicarbonate to carbon dioxide ratio is not defined by pH but rather it determines the pH. Since the estimated downhole pH was not measured but calculated from surface composition and temperature, our method probably achieved the pH at reservoir conditions more reliably than if pH were measured and adjusted at room conditions prior to testing.

When the fluid was sampled from the pore fluid system, the pressure on the emerging fluid was reduced to atmospheric and carbon dioxide was released as a gas. This gas was trapped and bubbled through six normal sodium hydroxide to dissolve the carbon dioxide and convert it to carbonate (CO_3). The sampled brine and sodium hydroxide were then tested for bicarbonate and carbonate concentration by sulfuric acid titration. In this way, the total bicarbonate composition of the removed brine was measured.

The fluid used in the Cerro Prieto tests originated from brine sampled at the geothermal field. The brine was collected from well M129 downstream of the separator and was consequently concentrated with respect to dissolved solids due to the loss of 30-40% by weight of steam. In the field, the sampled fluid was acidified with nitric acid to a pH of about 2, to minimize precipitation of silica and calcium carbonate during storage. Analyses of

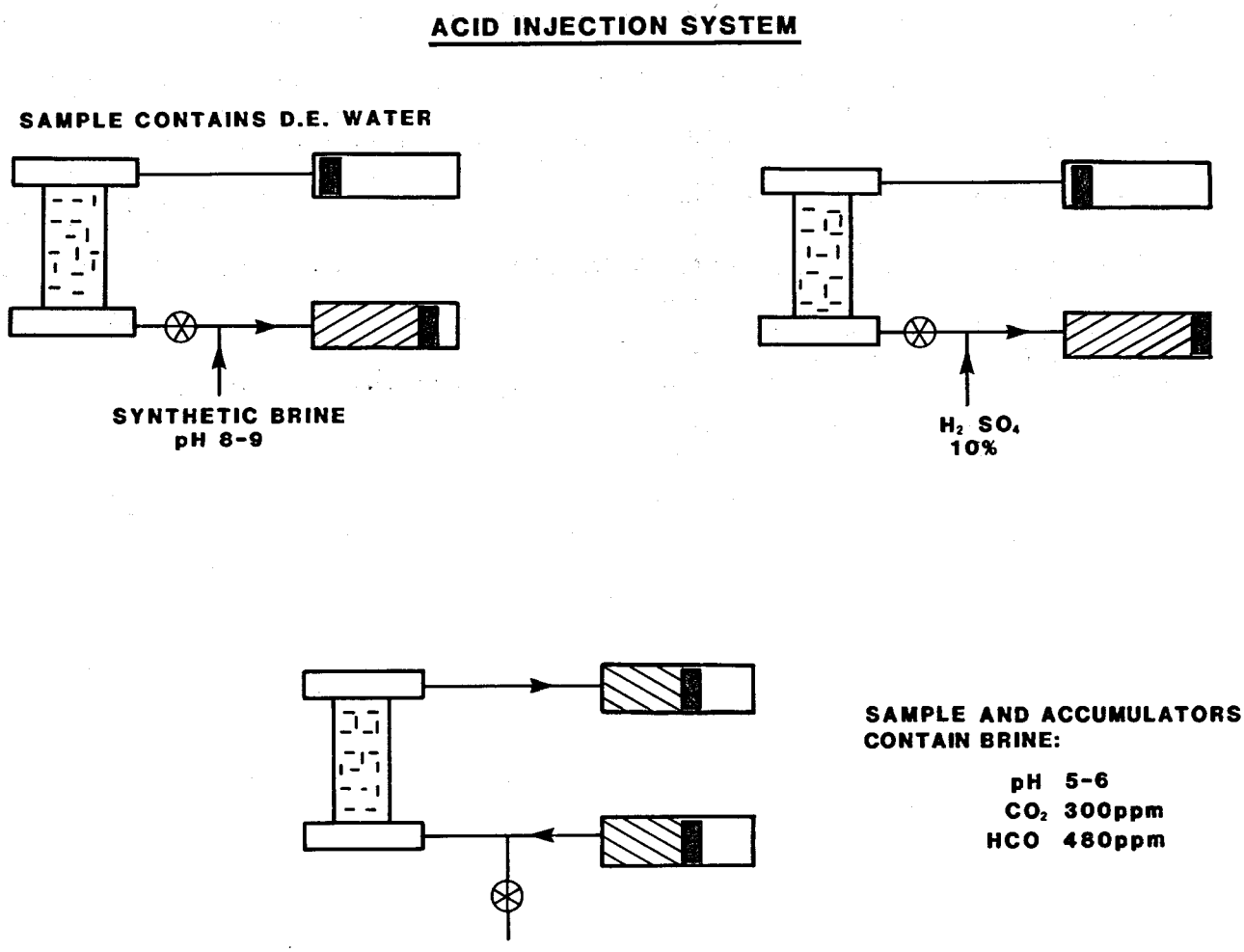

Figure 26. Schematic diagram of acid injection system used to achieve carbonate equilibrium and correct pH for high temperature, high pressure testing.

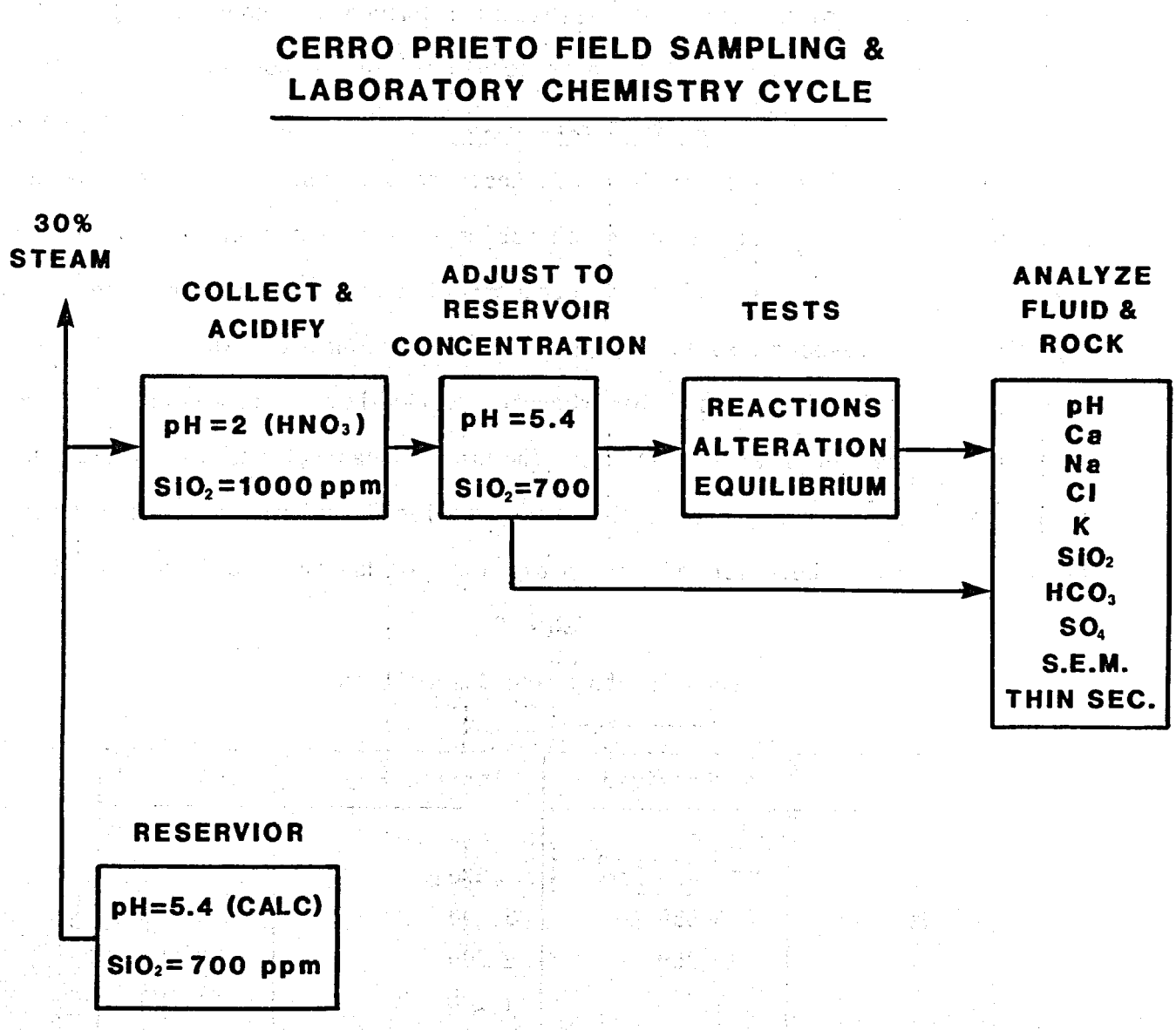

Figure 27. Flow chart of cycle through which fluid from the Cerro Prieto reservoir was taken between sampling at the wellhead and final analysis after testing.

this fluid have shown that the acidified brine can be stored for months with very little alteration.

The field sampling and fluid treatment sequence is shown in Figure 27. Immediately prior to use in the laboratory (within 24 hours), two to four liters of stabilized brine were diluted with deionized water and pH-adjusted with sodium hydroxide to approximate downhole conditions. The values for the major constituents for the concentrated, adjusted and estimated in-situ brines are given in Table 9. Although the concentrations in the fluid used in testing did not correspond exactly to the estimated downhole values, they were, with the exception of calcium bicarbonate, well within the range of values observed at the Cerro Prieto field. The low concentrations of calcium and bicarbonate were probably due to the precipitation of calcium carbonate during flashing and the liberation of carbon dioxide gas due to acidification. Once

Table 9

Cerro Prieto Brine Composition

Constituent	As Received [1]	In-Situ [2]	Test Cell
pH	1 - 2	5.4	5 - 6
Ca	430 ppm	370	270
Na	6,550	5,100	6,000
Cl	16,700	9,700	13,000
K	1,550	1,100	1,200
SiO_2	990	540	650
HCO_3	0	1,800 (Aq. CO_2)	0
SO_4	0	20	0
TDS	28,220	17,000 - 20,000	20,000

[1]Brine used in testing is actually sampled from The Cerro Prieto Field. As received fluid is sampled after the separator, and thus is concentrated due to flashing off of 30 - 40% of liquid.

[2]Source: Reed, 1976. Average of 12 wells.

the fluid was prepared for the test, it was introduced to the pore pressure system and pressurized in an accumulator. Any further modification of the fluid, similarly as done to the East Mesa brine, was performed at this stage.

For creep tests on both East Mesa and Cerro Prieto samples considerable flushing prior to actual testing was done, as described above in the creep testing section. Analyses have shown that flushing primarily removes salts and drilling mud residues left by the coring operation. The flushing procedure is shown schematically in Figure 28. After initial flushing, when downstream chemistry was acceptable, the specimen was brought to in-situ conditions and allowed to stabilize. The pore fluid was again sampled and compared to the input fluid. If the chemistry was not acceptable, additional flushing was performed at in-situ conditions; otherwise, the test proceeded. At the conclusion of the test, a volume of pore fluid equal to approximately one-half to three-fourths of a pore volume (20-30 cubic centimeters) was sampled and analyzed for the constituents as given in Table 10. These values are compared to those for the original input fluid to give insight to the degree of equilibrium acheived, completeness of flushing, and alteration to the specimen.

Table 10 also gives the method of analysis used for each constituent. The first method given is the primary method used, and other methods listed are performed occasionally to check the accuracy of the primary method and also, in the case of atomic absorption, when sample volume obtained was inadequate for other methods. The experimental accuracy of each determination is given in Table 11. This uncertainty is separated into two parts, analytical and sampling. The analytical accuracy is determined by factors such as meter and probe stability, dilution, and quality of standards. This uncertainty is generally smaller than that caused by sampling. Sampling errors include precipitation and dissolution within the system, mixing with brine or water

Table 10

Pore Fluid Chemistry Analysis

Constituent	Method
pH	Analog pH - Specific ion meter with solid state electrode
Sodium	Solid state ion electrode Atomic absorption
Chloride	Solid state ion electrode Silver nitrate titration
Potassium	Liquid ion exchange electrode Atomic absorption
Calcium	Liquid ion exchange electrode Atomic absorption EDTA titration
Sulfate	Spectrophotometer
Silica	Spectrophotometer Atomic absorption
Bicarbonate	Acid titration
Total dissolved solids	Gravimetric determination

Table 11

Experimental Accuracy

Constituent	Analytical Error	Sampling Error
pH	±0.1	±0.2
Sodium	10%	10%
Chloride	5%	10%
Potassium	5%	10%
Calcium	10 ppm or 10%	10%
Sulfate	10 ppm or 10%	10%
Silica	5%	15%
Bicarbonate	5%	50%

residue in the lines, and flashing when exposed to atmospheric pressure. In the case of the carbonate species, additional uncertainties were introduced by the gaseous CO_2 phase and contact between the brine and atmospheric CO_2.

The brine sampling system is shown in Figure 28. Pore fluid was sampled from the test vessel at a point directly below the endcap on the specimen. Lines were flushed with deionized water and then with nitrogen gas before the brine was sampled. A low nitrogen gas pressure was kept on the system while it was flowing to minimize loss or pick-up of carbon dioxide gas. The liquid and gaseous phases were separated in the brine trap and the off gases are bubbled through two columns of sodium hydroxide to dissolve any carbon dioxide. Some sampling uncertainties were introduced by the volume of fluid retained in the lines and the non-perfect efficiency of the carbon dioxide trap.

In general, the chemical analysis procedures, as can be seen from the above descriptions, are quite complex and therefore costly. For this reason, they were done for the creep tests only, where chemical factors were likely to be most important. During several creep tests, there were occurrences that caused chemical data to become inaccurate, such as some flashing in the system or other extremely non-equilibrium situations. In these cases, complete chemical procedures were reduced in scope accordingly.

3.6 Microstructural Analyses

Three procedures were used for microstructural analyses: thin section petrographic analysis, x-ray diffraction, and scanning electron microscope analysis. In most cases, samples were studied with one or more procedures both before and after creep testing. The main objective of post-test analysis was to identify microstructural mechanisms of creep compaction. Thin sections were prepared and studies of basic mineralogy of the specimens were done at

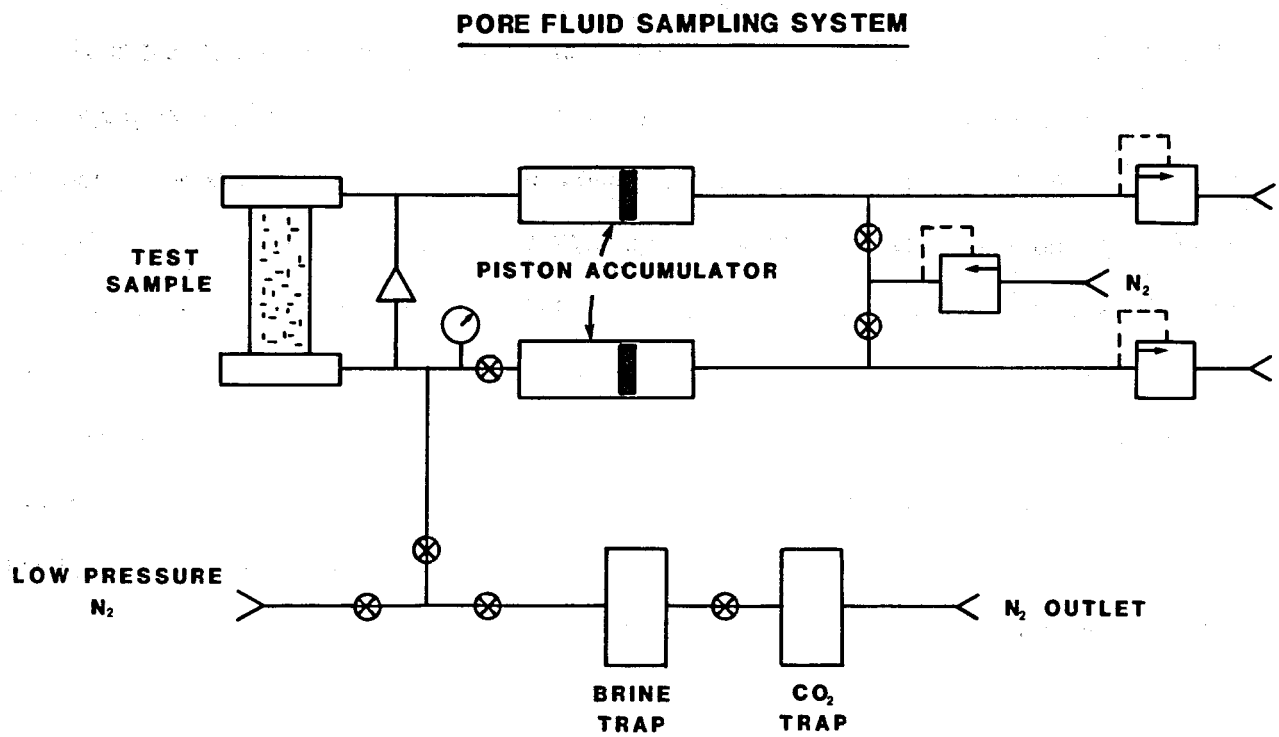

Figure 28. Schematic diagram showing flushing procedure used to achieve fluid equilibrium prior to creep testing.

Terra Tek. These were especially valuable for study of the pre-test materials. For post test studies, although thin sections were useful, it was found that the scanning electron microscope was much more informative. X-ray diffraction was done on both pre- and post-test specimens to study clay alterations. The x-ray diffraction was carried out with Cu K- alpha radiation at 40 KV accelerating potential and 20 MA current. In general, three sets of scans were done for each sample, the first on an air-dried specimen, the second on a specimen exposed to ethylene/glycol vapor for several hours, which caused expansion of swelling clays, and the third on a sample heated to 550°C, which destroyed any kaolinite present. These methods allowed separation of clay types. Results will be described later. SEM samples were prepared by tensile fracturing and mounted on a sample holder followed by ultrasonic cleaning. In addition, the SEM used had a computerized energy dispersive analysis by X-ray (EDAX) system, which allowed a quick determination elemental composition along with each SEM frame. The SEM work was used to characterize porosity and pore throat structures, to identify dissolution of minerals during tests and to look for possible growth of authigenic phases caused by testing.

4. BASIC TESTING RESULTS

In this chapter results will be presented in the form of graphs of mean stress versus volume strain, where mean stress is defined as the average of the three principal stresses. In the case of the hydrostatic test, the mean stress is exactly equal to the confining pressure. In the case of any test where additional axial stress has been applied (triaxial, uniaxial), the mean stress is the confining pressure plus one-third of the additional axial stress applied. In tests where pore pressure has been applied and measured, stress values will be presented in terms of mean effective stress. In this case, we will use the Terzaghi mean effective stress, defined as the total mean effective stress (as given above) less the pore pressure. Graphs of mean effective stress versus volume strain may easily be interpreted in terms of specimen compressibility. This will be the best way of comparing data from test to test. Volume strain is the sum of the three principal strains. In this case, engineering strains are used, so all strains are with reference to the initial sample dimensions. Compressibility is defined as the ratio of incremental volume strain to incremental pressure (or incremental mean effective stress).

4.1 East Mesa

4.1.1 Drained Hydrostats

Drained hydrostats are a basic measure of skeletal deformation. These tests were done on saturated specimens that were allowed to drain during the tests at essentially atmospheric pore pressure. Results are given in Figures 29-32 for the three characteristic types of material that were obtained from the East Mesa reservoir: overlying caprock, the intermediate depth production sand, and the deep production sand. All of the results demonstrate non-linearity and irreversible compaction that are typical of porous rocks when

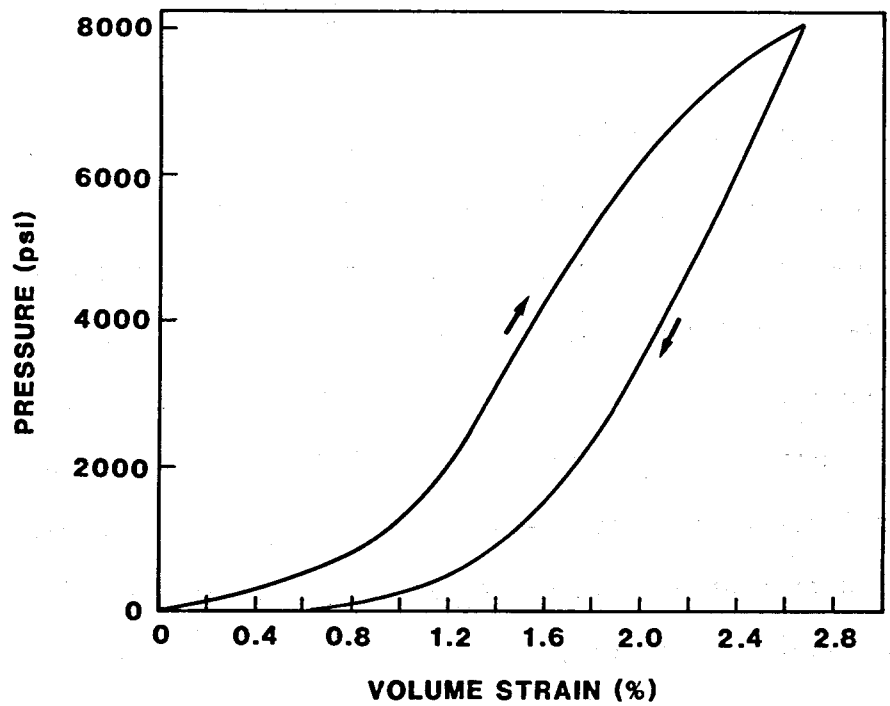

Figure 29. Drained hydrostat on caprock material from East Mesa well 58-30, depth 3,268', porosity 18.4%, test temperature 25°C, compressibility at 2000 psi 2.3×10^{-6} psi^{-1}.

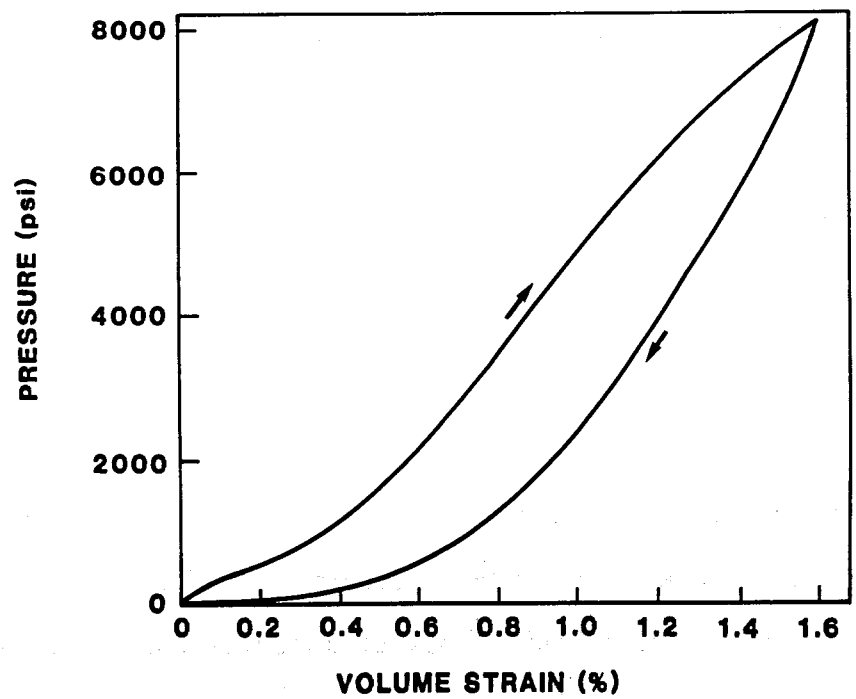

Figure 30. Drained hydrostat on caprock material from East Mesa well 58-30, depth 3,270', porosity 18.0%, test temperature 25°C, compressibility at 2000 psi 2.4×10^{-6} psi^{-1}.

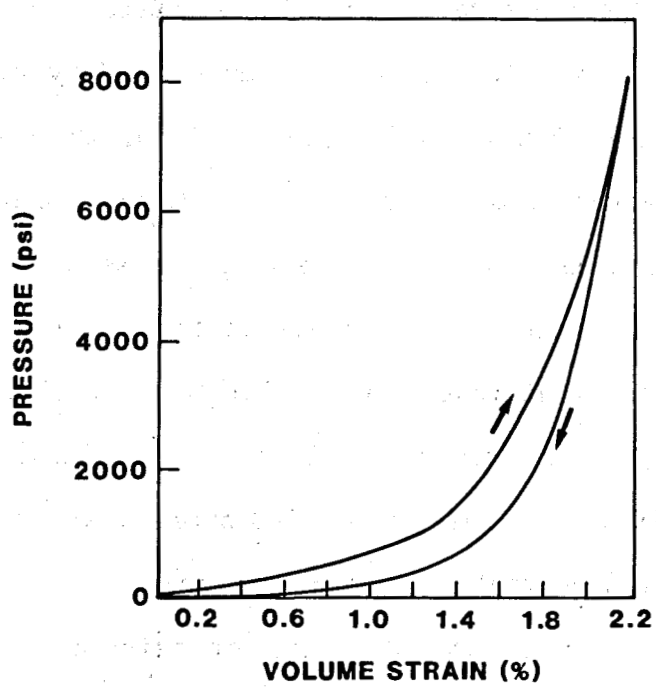

Figure 31. Drained hydrostat on reservoir material from East Mesa well 78-30, depth 5,500', porosity 18.5%, test temperature 25°C, compressibility at 2750 psi 1.6×10^{-6} psi^{-1}.

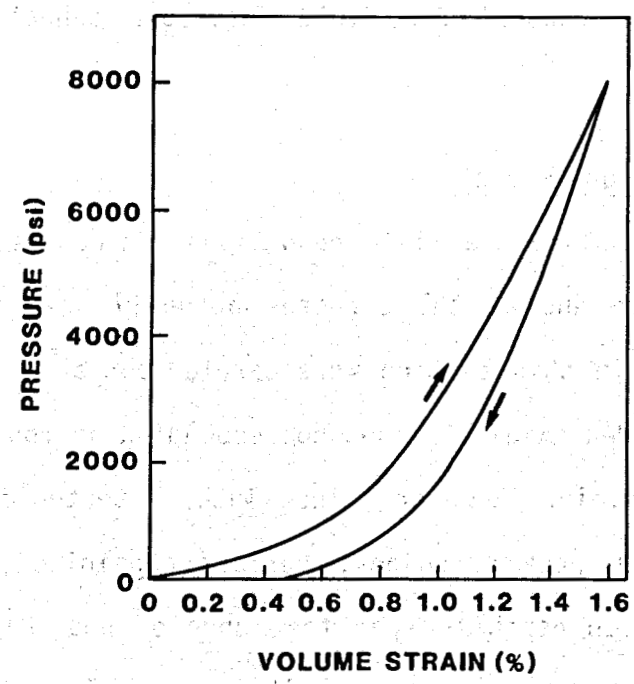

Figure 32. Drained hydrostat on reservoir material from East Mesa well 78-30, depth 7,150', porosity 17.3%, test temperature 25°C, compressibility at 3600 psi 1.3×10^{-6} psi^{-1}.

stressed beyond their natural in-situ stress state. In this case, the caprock silt-clay material was the softest. Compressibility at reservoir conditions was in the range of 2.5 to $3x10^{-6}$ psi^{-1}. Also, there were considerable hysteresis and permanent compaction upon unloading, as can be seen in Figures 29 and 30. Moving deeper into the reservoir, as seen in Figure 31, hysteresis diminished somewhat and the materials stiffen, having a compressibility of about $1.6x10^{-6}$ psi^{-1} at reservoir conditions. Finally, at the deepest point, as seen in Figure 32, compressibility was the least at $1.3x10^{-6}$ psi^{-1} at reservoir conditions. These tests indicated that the caprock was a quite plastic material, and that the reservoir rock becomes increasingly less plastic with depth. Severe overstressing of material, that is, loading well beyond reservoir conditions, caused extreme softening only in the case of the caprock and not in the case of the reservoir material. The reservoir rock itself appeared to behave as a reasonably well-consolidated sandstone. Its behavior was not unusual for fluid reservoir sandstones in this porosity range.

4.1.2 Pore Pressure Reduction

To truly simulate the field conditions, it was necessary to test at elevated temperature and at the stresses actually seen in the reservoir. The tests described in this section were carried out at elevated temperatures and at total overburden axial stresses corresponding approximately to those existing in the reservoir. However, since lateral tectonic stresses vary and are mostly unknown in these regions, various confining pressures were used on material from each depth to span the range of possible ratios of lateral to vertical in-situ stress. These conditions are given in Table 12. The tests were conducted by first carefully bringing the rock to the approximated reservoir conditions while taking care to not exceed the mean effective stress at

Table 12

Initial Conditions, East Mesa
Pore Pressure Reduction Tests

Depth (ft)	Stress or Pressure (psi)			Temperature (°C)
	Confining	Pore	Axial	
3300	2200	1380	1100	150
	2750	1380	550	
	3300	1380	0	
5600	3710	2300	1890	165
	4660	2300	940	
	5600	2300	0	
7200	4760	2930	2470	175
	5980	2930	1220	
	7200	2930	0	

reservoir conditions prior to the pore pressure cycling part of the test. Then, pore pressure was reduced by 1000 psi to simulate well production. The pore pressure was cycled three times to investigate hysteresis effects that would be caused by alternate pressure reduction and recharge. In some cases, conditions were held constant for periods of up to about 30 minutes to investigate the primary phase of creep behavior for later use in creep testing. Results, in terms of mean effective stress versus volume strain, are shown in Figures 33-41.

Looking first at Figures 33, 34 and 35, which show the pore pressure cycling results for the clay-silt caprock, we see that, with an increased ratio of load to confining pressure, there was a corresponding increase of compressibility. This is consistent with the increasing deviatoric stress (resulting in higher interval shear stresses) that had been applied to the

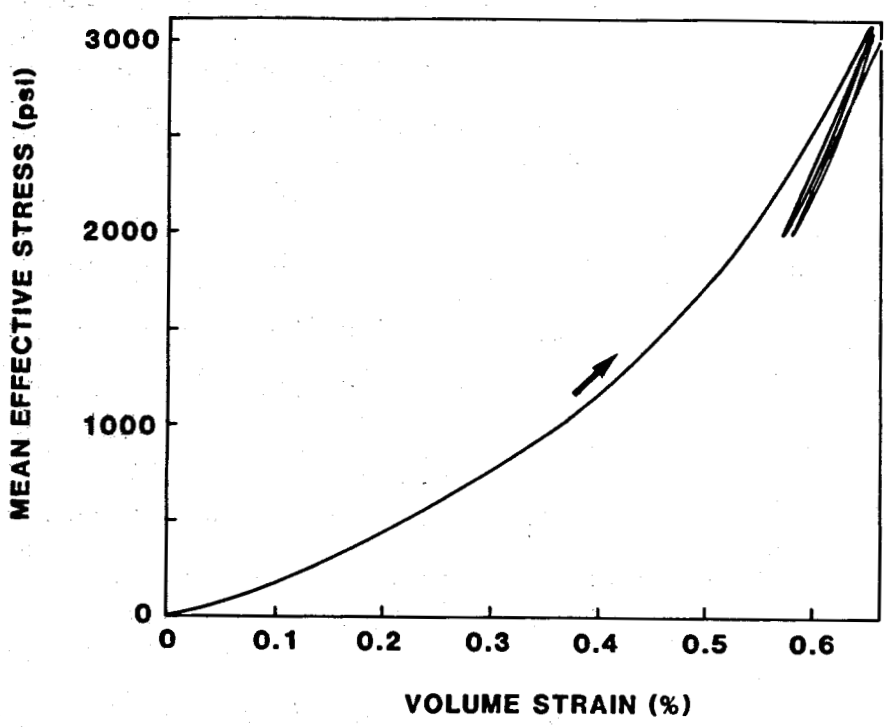

Figure 33. Pore pressure cycling test on caprock material from East Mesa 58-30, depth 3,280', porosity 19.3%, test temperature 150°C, no shear stress. Compressibility is 1.1×10^{-6} psi^{-1} for effective stress increase and 0.7×10^{-6} psi^{-1} for effective stress decrease.

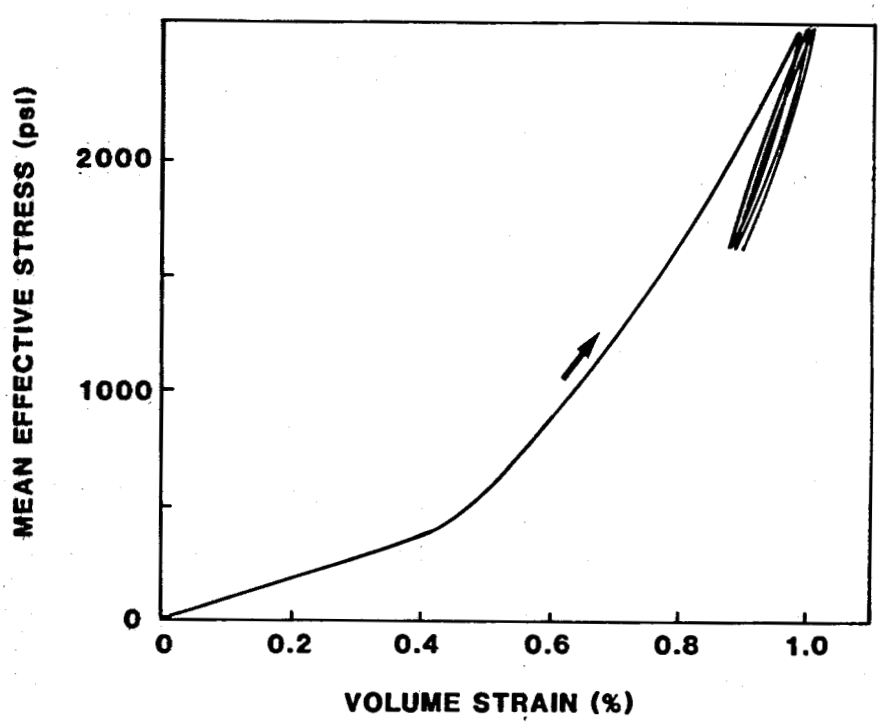

Figure 34. Pore pressure cycling test on caprock material from East Mesa 58-30, depth 3,280', porosity 20.0%, test temperature 150°C, intermediate shear stress. Compressibility is 1.9×10^{-6} psi^{-1} for effective stress increase and 1.1×10^{-6} psi^{-1} for effective stress decrease.

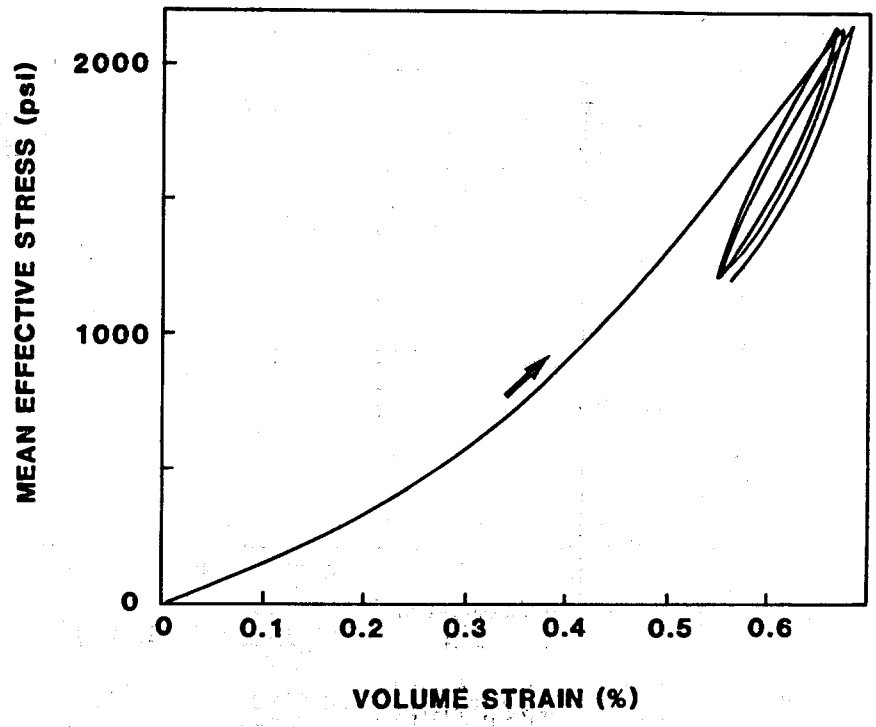

Figure 35. Pore pressure cycling test on caprock material from East Mesa 58-30, depth 3,280', porosity 19.7%, test temperature 150°C, high shear stress. Compressibility is 2.1×10^{-6} psi^{-1} for effective stress increase and 1.4×10^{-6} psi^{-1} for effective stress decrease.

rock and its effect on enhancement of compaction. We see also that the rock was about 60% stiffer on the second and subsequent cycles of compaction. This is consistent with the rather plastic nature of this caprock material.

The material from the intermediate depth production zone, shown in Figures 36, 37 and 38, was quite stiff with respect to pore pressure reduction when a large axial stress had not been applied. However, with application of deviatoric stress this material becomes, in comparison, quite soft. This intermediate-depth reservoir rock might, therefore, be termed somewhat stress sensitive. Average compressibility reduction caused by cycling was about 52%.

The deep reservoir sand, shown in Figures 39, 40 and 41 was easily the stiffest material of this group. Also, on average, it showed the least hysteresis with cycling, although there was some indication of softening and

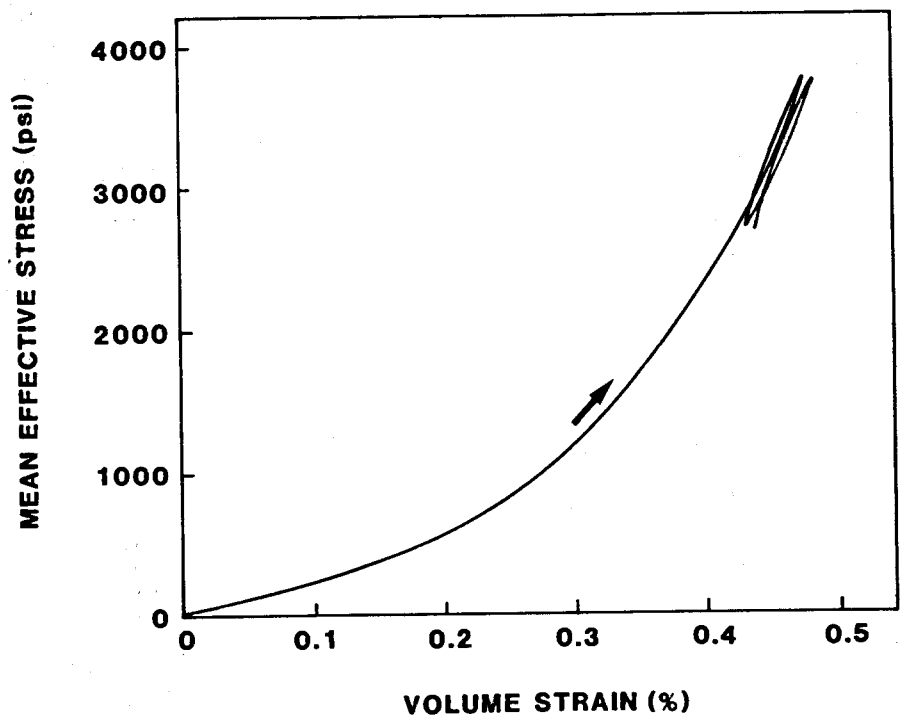

Figure 36. Pore pressure cycling test on reservoir material from East Mesa 78-30, depth 5,500', porosity unknown, test temperature 150°C, no shear stress. Compressibility is 0.5×10^{-6} psi^{-1} for effective stress increase and 0.4×10^{-6} psi^{-1} for effective stress decrease.

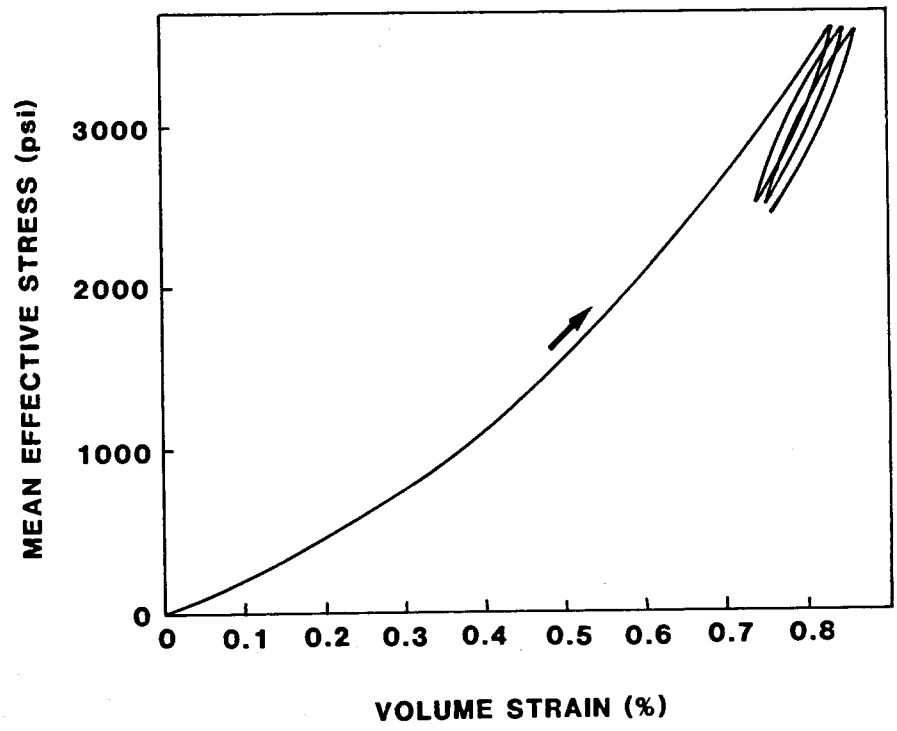

Figure 37. Pore pressure cycling test on reservoir material from East Mesa 78-30, depth 5,500', porosity 19.9%, test temperature 150°C, intermediate shear stress. Compressibility is 1.5×10^{-6} psi^{-1} for effective stress increase and 0.8×10^{-6} psi^{-1} for effective stress decrease.

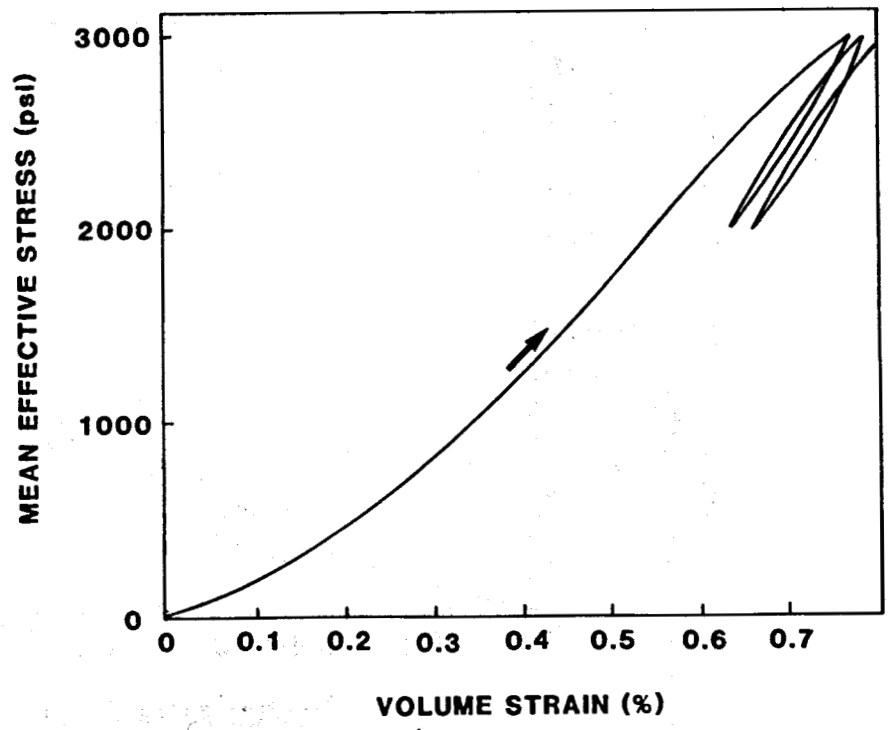

Figure 38. Pore pressure cycling test on reservoir material from East Mesa 78-30, depth 5,500', porosity 20.3%, test temperature 150°C, high shear stress. Compressibility is 2.3×10^{-6} psi^{-1} for effective stress increase and 1.6×10^{-6} psi^{-1} for effective stress decrease.

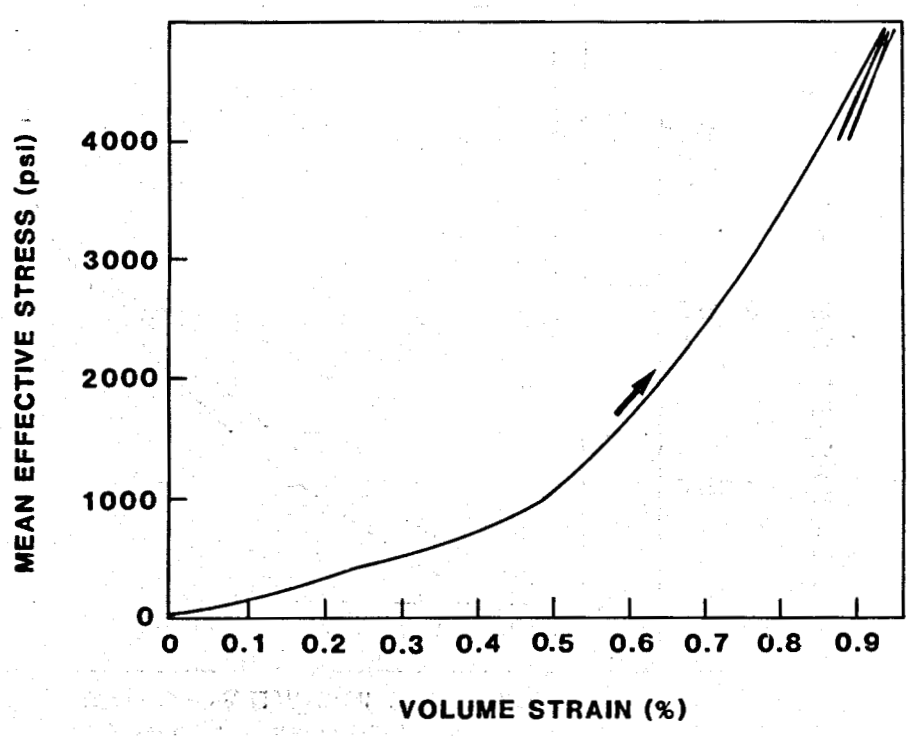

Figure 39. Pore pressure cycling test on reservoir material from East Mesa 78-30, depth 7,150', porosity 16.9%, test temperature 150°C, no shear stress. Compressibility is 0.8×10^{-6} psi^{-1} for effective stress increase and 0.6×10^{-6} psi^{-1} for effective stress decrease.

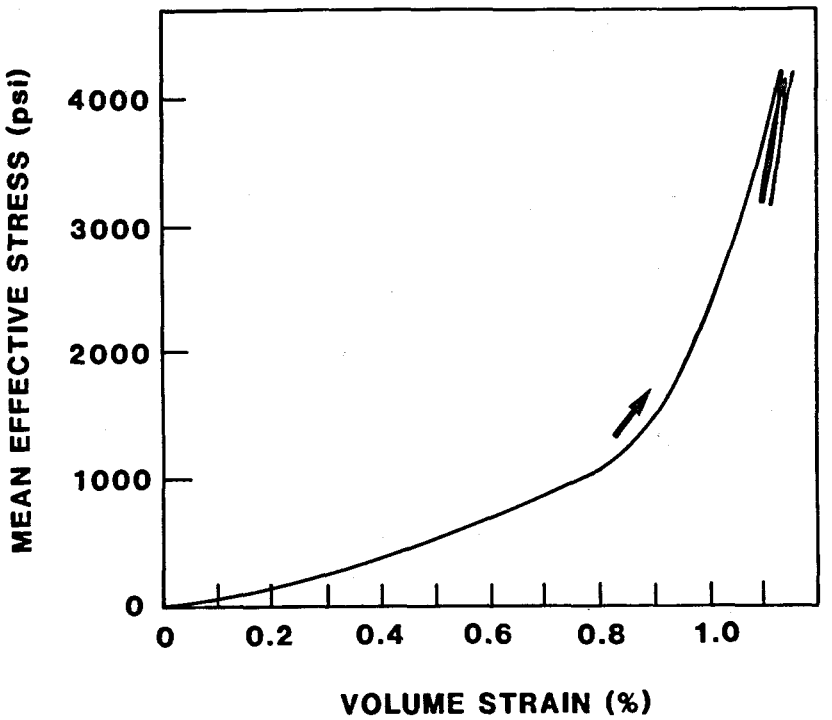

Figure 40. Pore pressure cycling test on reservoir material from East Mesa 78-30, depth 7,155', porosity 15.0%, test temperature 150°C, intermediate shear stress. Compressibility is 0.7×10^{-6} psi^{-1} for effective stress increase and 0.5×10^{-6} psi^{-1} for effective stress decrease.

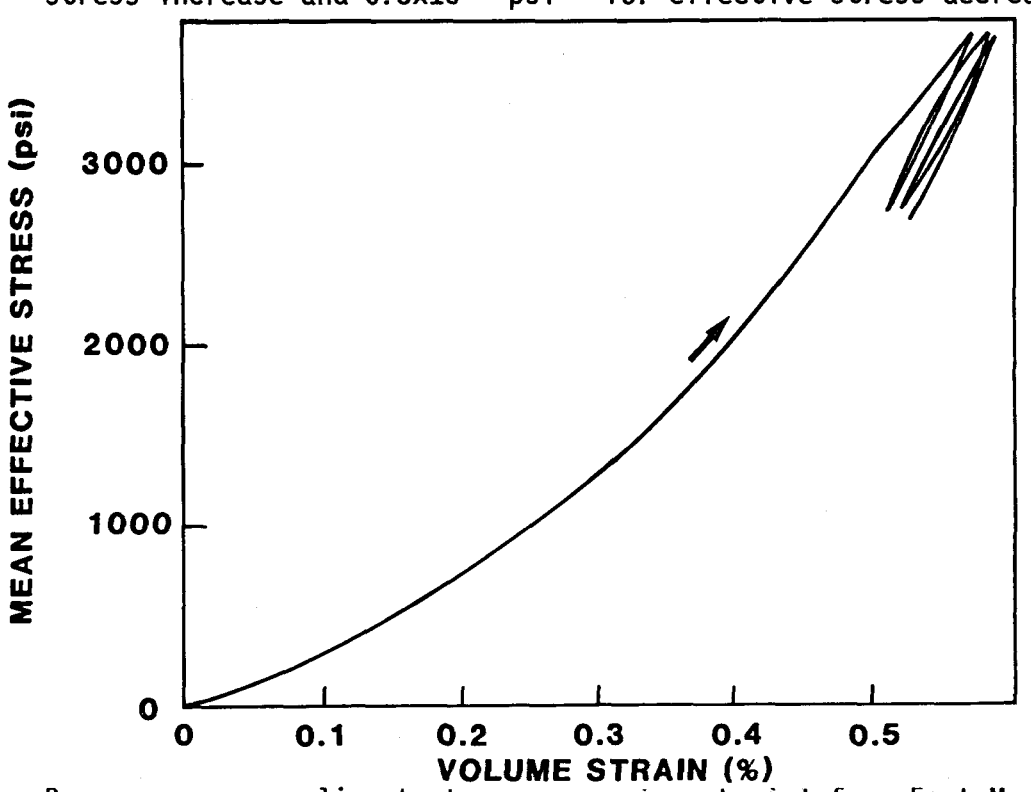

Figure 41. Pore pressure cycling test on reservoir material from East Mesa well 78-30, depth 7,150', porosity 15.2%, test temperature 150°C, high shear stress. Compressibility is 1.0×10^{-6} psi^{-1} for effective stress increase and 0.6×10^{-6} psi^{-1} for effective stress decrease.

larger hysteresis at the highest deviatoric stress ratio. Average compressibility with cycling was about 46%.

Viewing all of the pore pressure cycling results for East Mesa material, we see confirmation of the general trend observed earlier (during hydrostatic testing) to a stiffening of material with depth. However, now that deviatoric stresses have been applied to specimens (in the form of an axial stress to confining pressure ratio) to simulate vertical to horizontal stress ratios in the field, we observe that the intermediate reservoir material becomes somewhat more stress sensitive than the deep reservoir material. All material shows increased compaction at comparable mean stress but with increased deviatoric stress as would be expected for a porous solid that is undergoing plastic deformation.

4.1.3 Confining Pressure Cycling and Uniaxial Compaction

The remaining basic tests on material from East Mesa are a combination of two types of testing. For this testing, specimens were brought to conditions of elevated pressure and temperature as before, but then, instead of reducing pore pressure, confining pressure was increased by 1000 psi and cycled. This procedure served the purposes of checking the trends of previous data and also of studying the accuracy of the Terzaghi effective law as applied to this material. Following the confining pressure cycling, a final effective stress increase was produced by reduction of pore pressure as in the previous section. However, in this case, confining pressure was adjusted to maintain zero incremental transverse strain during the pore pressure reduction cycle. This was done to obtain a compressibility coefficient for uniaxial compaction. Results of these tests are given in Figures 42-47. Stress conditions to start these tests were the same as for the intermediate shear stress tests of the previous section.

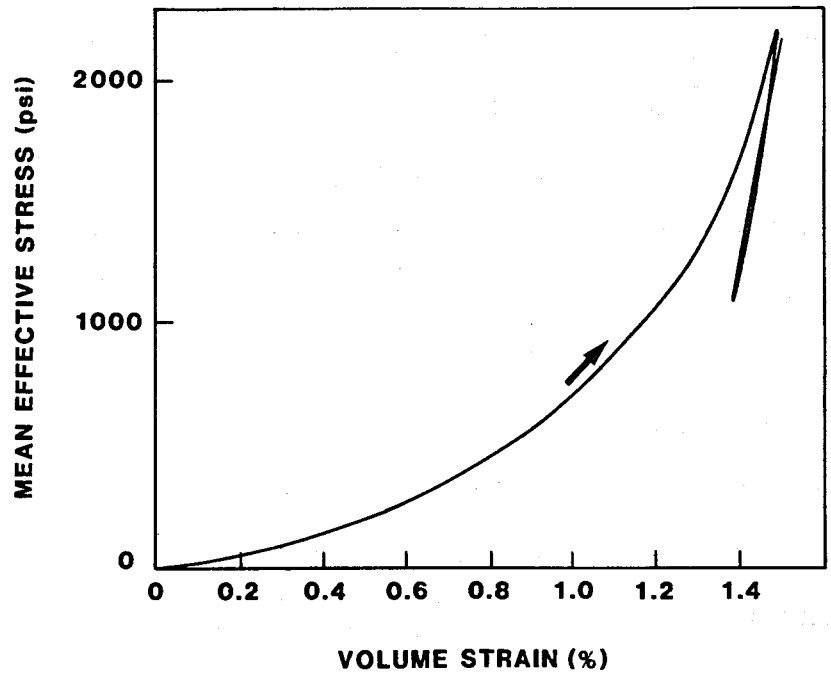

Figure 42. Confining pressure cycling test on caprock material from East Mesa well 58-30, depth 3,280', porosity 17.7%, test temperature 150°C. Compressibility is 2.0×10^{-6} psi^{-1} for effective stress increase and 1.0×10^{-6} psi^{-1} for effective stress decrease.

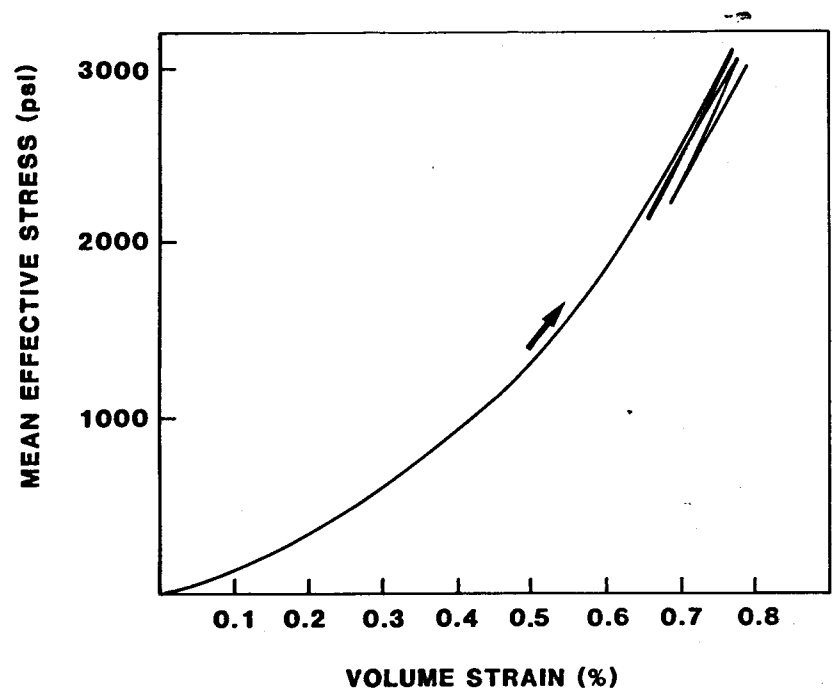

Figure 43. Confining pressure cycling test on caprock material from East Mesa well 78-30, depth 5,500', porosity 20.4%, test temperature 150°C. Compressibility is 1.3×10^{-6} psi^{-1} for effective stress increase and 1.3×10^{-6} psi^{-1} for effective stress decrease.

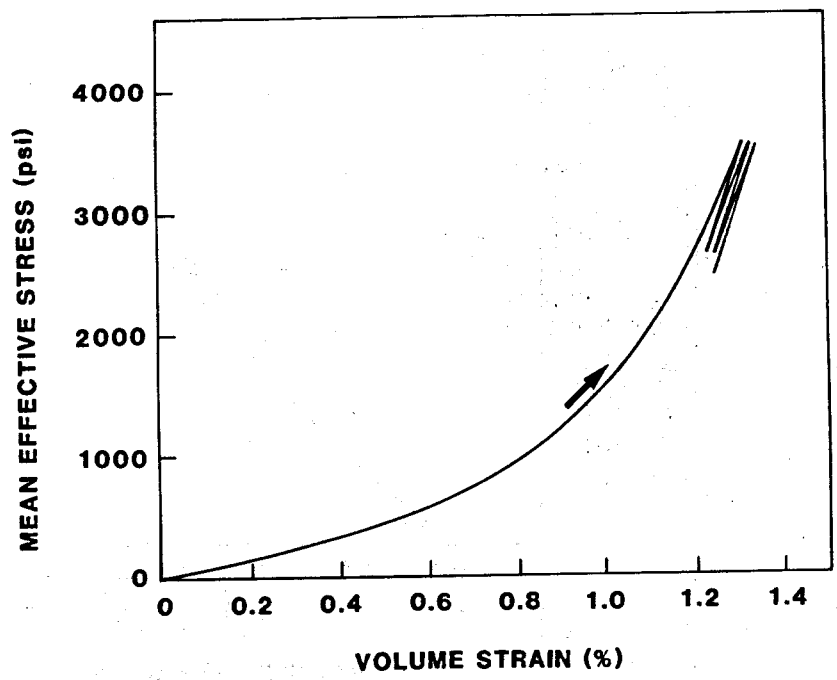

Figure 44. Confining pressure cycling test on reservoir material from East Mesa well 78-30, depth 7,150', porosity 17.3%, test temperature 150°C. Compressibility is 1.2×10^{-6} psi^{-1} for effective stress increase and 1.1×10^{-6} psi^{-1} for effective stress decrease.

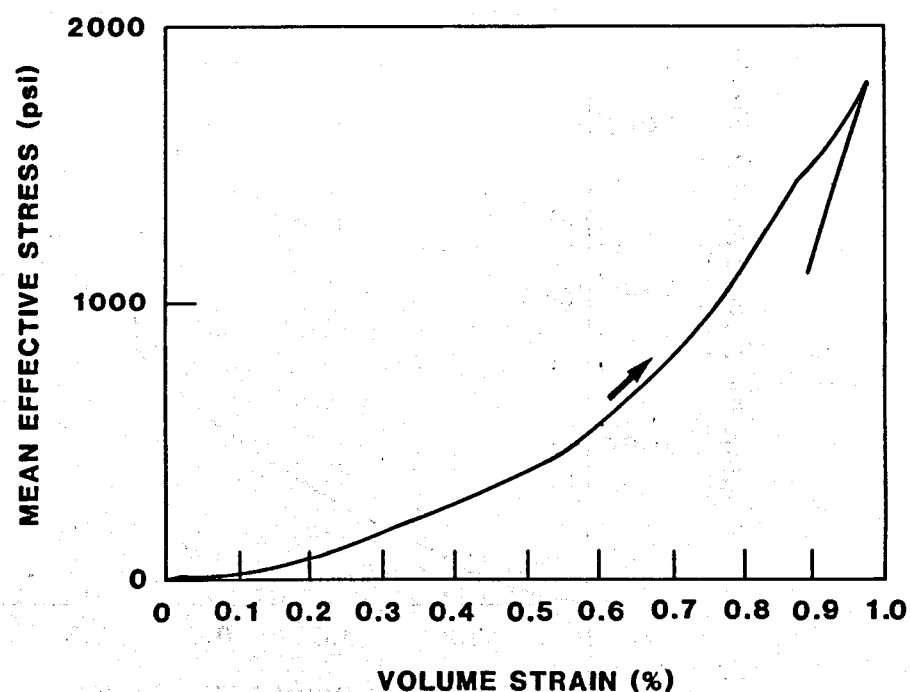

Figure 45. Uniaxial compaction test on reservoir material from East Mesa well 58-30, depth 3,280', porosity 18.6%, test temperature 150°C. Compressibility is 3.0×10^{-6} psi^{-1} for effective stress increase and 1.2×10^{-6} psi^{-1} for effective stress decrease.

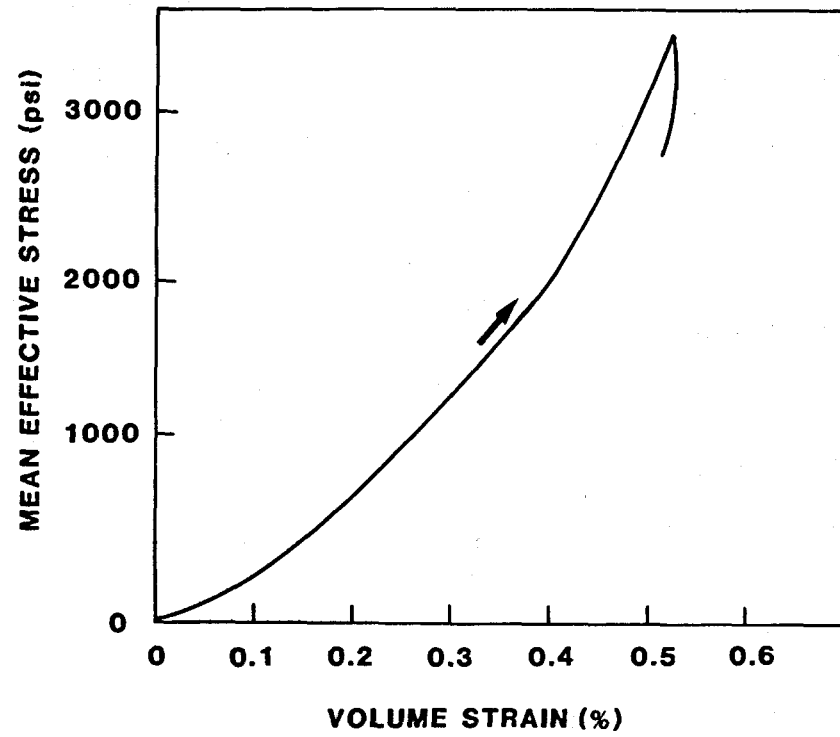

Figure 46. Confining pressure cycling test on reservoir material from East Mesa well 78-30, depth 5,510', porosity 14.8%, test temperature 150°C. Compressibility is 0.9×10^{-6} psi^{-1} for effective stress increase and 0.3×10^{-6} psi^{-1} for effective stress decrease.

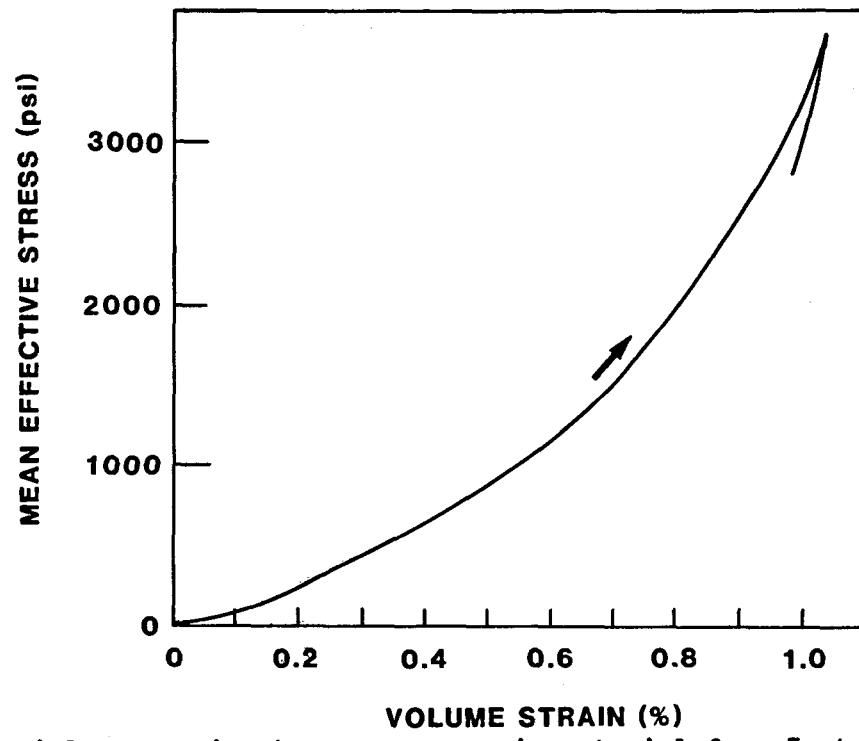

Figure 47. Uniaxial compaction test on reservoir material from East Mesa well 78-30, depth 7,150', porosity 15.9%, test temperature 150°C. Compressibility is 1.2×10^{-6} psi^{-1} for effective stress increase and 0.8×10^{-6} psi^{-1} for effective stress decrease.

Confining pressure cycling results, shown in Figures 42, 43 and 44, indicate the same trends as before towards stiffening with depth, and greater plasticity in the caprock. If these results are compared with their pore pressure cycling counterparts, shown in Figures 34, 37 and 40, differences are observed that are probably not significant with respect to the expected range of variation from rock sample to rock sample. We therefore conclude that the simple Terzaghi effective stress is a useful concept in this case.

Uniaxial compaction cycling experiments are shown in Figures 45, 46 and 47. When compared to the previous tests, interpretation is uncertain. The caprock material compacted more severely in uniaxial strain; the intermediate depth reservoir rock compacted less severely; and the deep reservoir rock behaved about the same as before. However, note that the porosity of the particular specimen selected from the intermediate depth reservoir was rather low and this could account for the unusual stiffness of this material. If this result is disregarded, then one sees again that the deep reservoir material behaved most elastically. It did not change much in its response to uniaxial strain testing as compared to previous testing. In contrast, the caprock, again the most plastic material, responded to the shearing caused by deviatoric stress during this test in a more inelastic manner.

4.2 Cerro Prieto

The basic testing plan for Cerro Prieto material was similar to that for East Mesa material. Testing began with a number of drained hydrostats under various conditions to investigate the effects of temperature, saturation with different types of fluid, etc. Then, testing continued with pore pressure cycling, confining pressure cycling, and uniaxial compaction tests. The major difference in the testing plan for Cerro Prieto material was that samples were

chosen from many different wells rather than from several depths in only two wells.

4.2.1 Drained Hydrostats

Results of basic testing are shown in Figures 48-53. Drained hydrostats at room temperature on material from well M123 are shown in Figures 48 and 49. These results are typical for porous sandstone. Compressibilities were about $1x10^{-6}$ psi^{-1} at reservoir pressures and some hysteresis was evident. Figures 50 and 51 show hydrostatic compression of material from well T366 from a depth of greater than 8,200 feet. Note, however, that porosity was greater than for the previous well, and that these tests were at elevated temperature. Despite the differences in depth and temperature, the compressibilities at reservoir conditions were approximately the same as those of the previous well. Figure 51 shows, additionally, the effect of pressure cycling. The degree of plasticity was moderate with some hysteresis. Figures 52 and 53 show two more drained hydrostats at elevated temperatures on material from the same well, T366. However, this material was from a slightly different location and had considerably less porosity. Note that compressibilities were comparable to those obtained in the previous tests which could indicate that the material causing the lowering of porosity is a soft material that does not contribute to strengthening or stiffening of the structure. The six tests described in this section have demonstrated the repeatability of our test technique when used for similar rocks. They also show that, in basic properties, the reservoir rocks from East Mesa and Cerro Prieto at the locations chosen, did not significantly differ in their compressibilities.

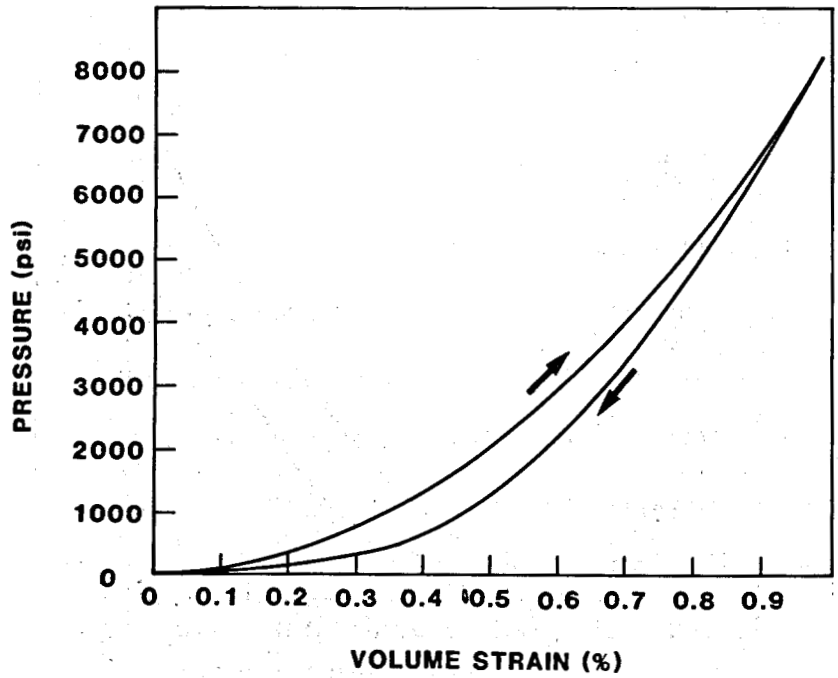

Figure 48. Drained hydrostat on material from Cerro Prieto well M-123, depth 5,200', porosity 14.0%, test temperature 25°C, compressibility at 1000 psi 1.0×10^{-6} psi^{-1}.

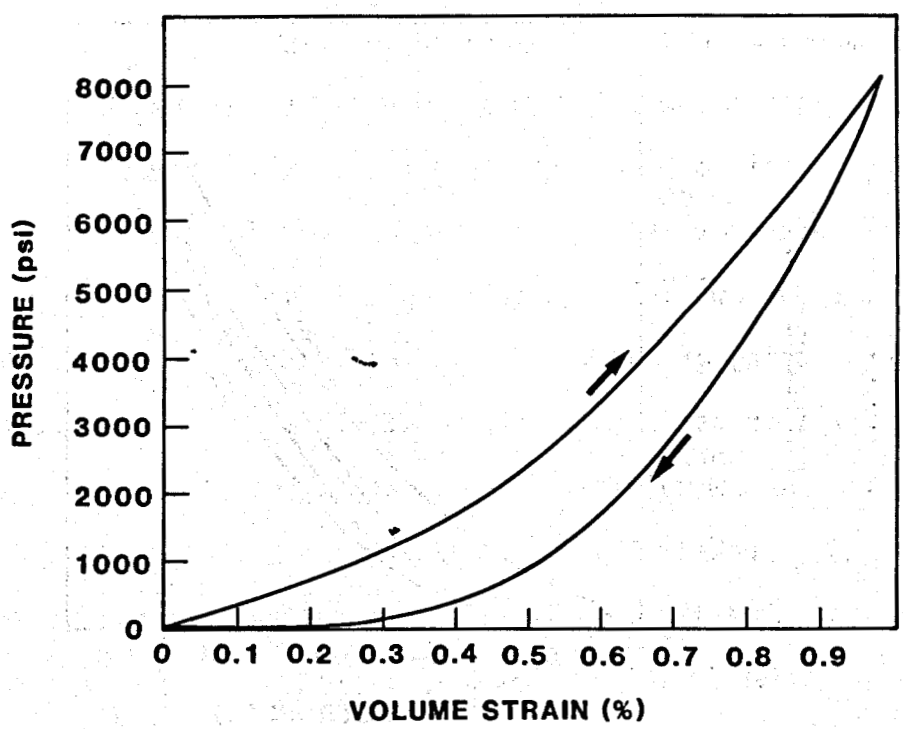

Figure 49. Drained hydrostat on material from Cerro Prieto well M-123, depth 5,200', porosity 14.9%, test temperature 25°C, compressibility at 3000 psi 1.1×10^{-6} psi^{-1}.

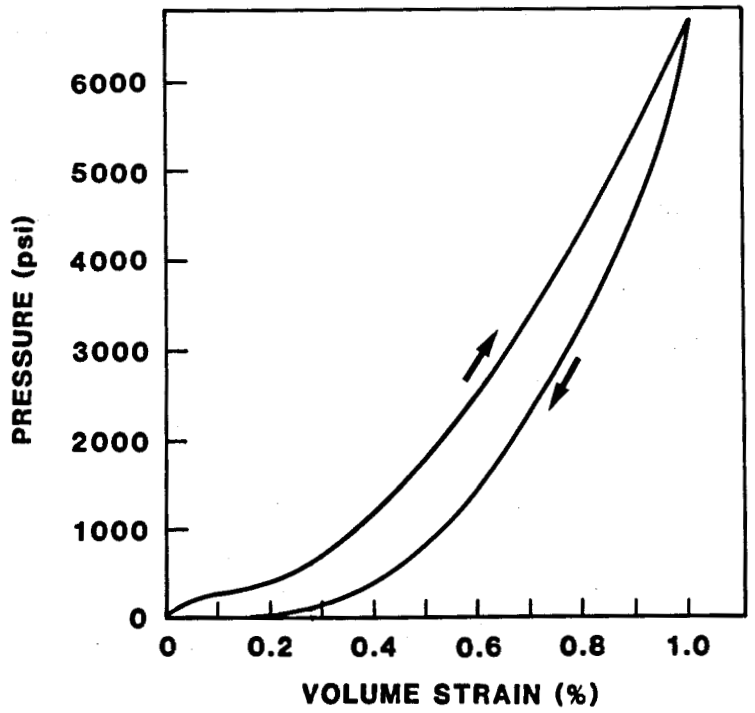

Figure 50. Drained hydrostat on material from Cerro Prieto well T-366, depth 8,269', porosity 19.8%, test temperature 90°C, compressibility at 5000 psi 1.1×10^{-6} psi^{-1}.

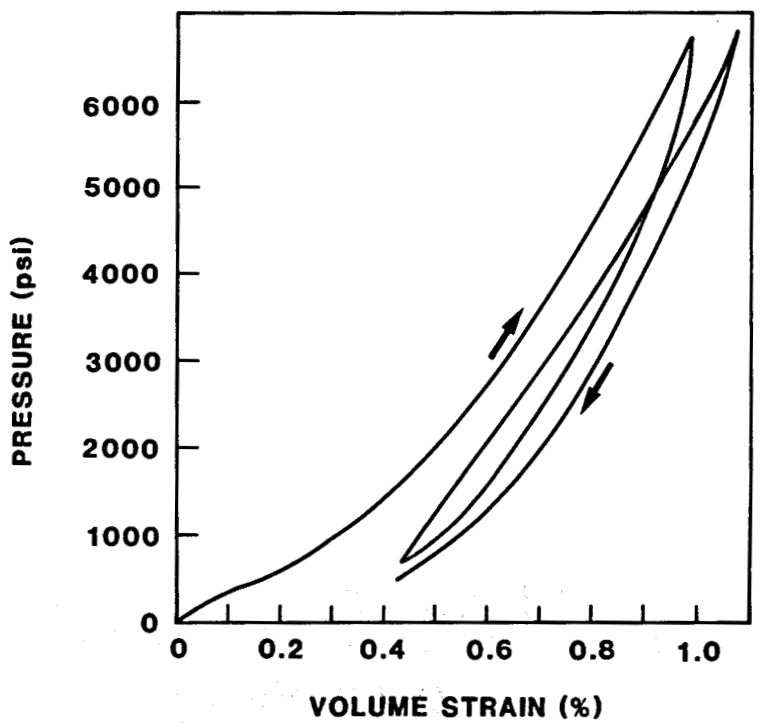

Figure 51. Drained hydrostat on material from Cerro Prieto well T-366, depth 8,269', porosity 19.7%, test temperature 90°C, compressibility at 5000 psi 1.0×10^{-6} psi^{-1}.

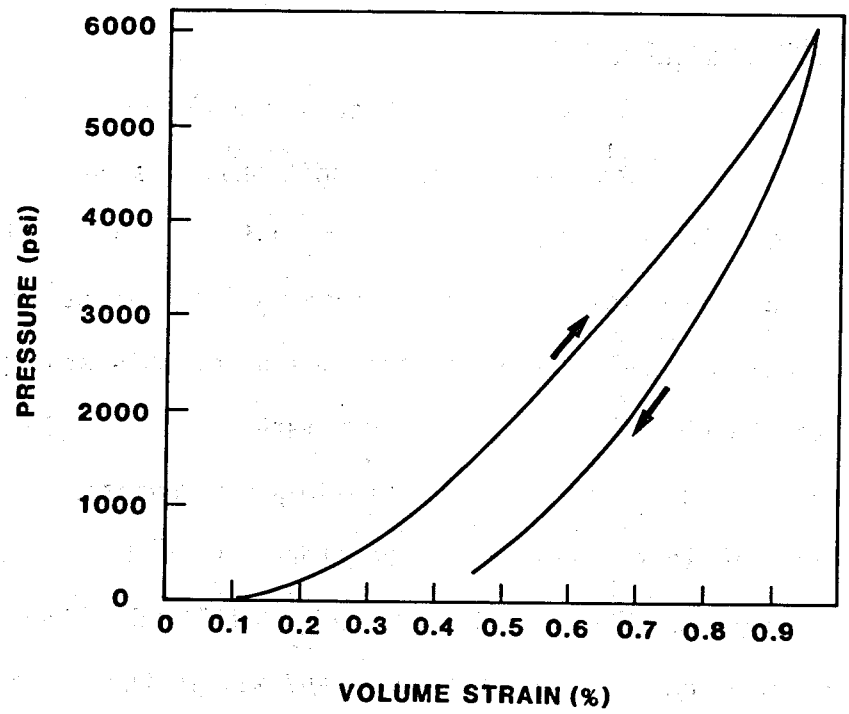

Figure 52. Drained hydrostat on material from Cerro Prieto well T-366, depth 8,269', porosity 13.8%, test temperature 90°C, compressibility at 5000 psi 1.0×10^{-6} psi^{-1}.

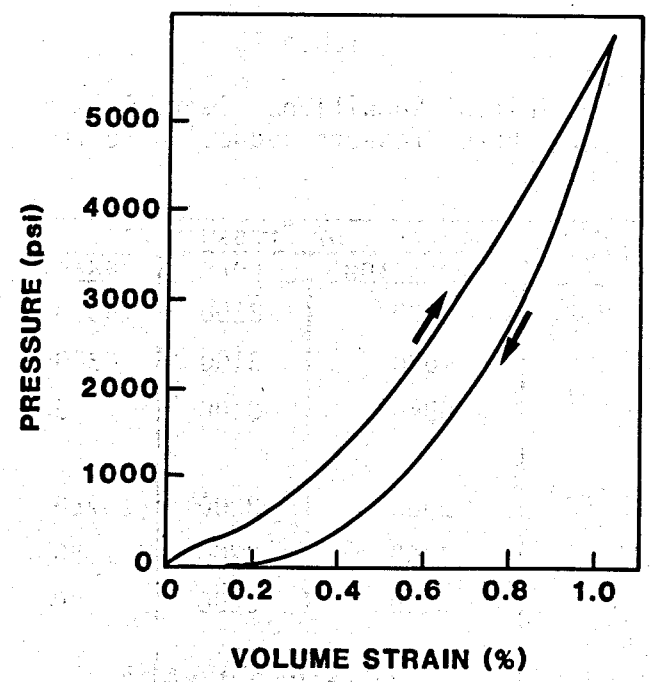

Figure 53. Drained hydrostat on material from Cerro Prieto well T-366, depth 8,269', porosity 13.7%, test temperature 90°C, compressibility at 5000 psi 1.2×10^{-6} psi^{-1}.

4.2.2 Pore Pressure Reduction

As in the tests for East Mesa, three materials were selected which were then subjected to the choices of test conditions as shown in Table 13. They were zero, intermediate, and high ratios of additional axial stress to confining pressure, corresponding to low, moderate, and large amounts of shear stress. Material was selected from three wells for this study; well M107 with material from 7,067 feet, well M127 with material from 7,136 feet, and well T366 with material from 8,010 feet. The highest deviatoric stress generally caused failure of test specimens. Therefore, only the low and intermediate deviatoric stress results are shown in Figures 54-59. Compressibilities in these three wells were quite comparable, and all in the range 0.6 to 0.9×10^{-6} psi^{-1}. There was no significant trend to increased plastic behavior as deviatoric stresses were increased, nor was there any significant hysteresis caused by cycling. These observations, coupled with the tendency for failure at the

Table 13

Initial Conditions, Cerro Prieto
Pore Pressure Reduction Tests

Well	Depth (ft)	Stress or Pressure (psi)			Temperature (°C)
		Confining	Pore	Axial	
M-107	7070	2300	3100	4630	150
		4630	3100	2300	
		6940	3100	0	
M-127	7140	2380	3200	4760	150
		4760	3200	2380	
		7140	3200	0	
T-366	8010	2670	3600	5340	150
		5340	3600	2670	
		8015	3600	0	

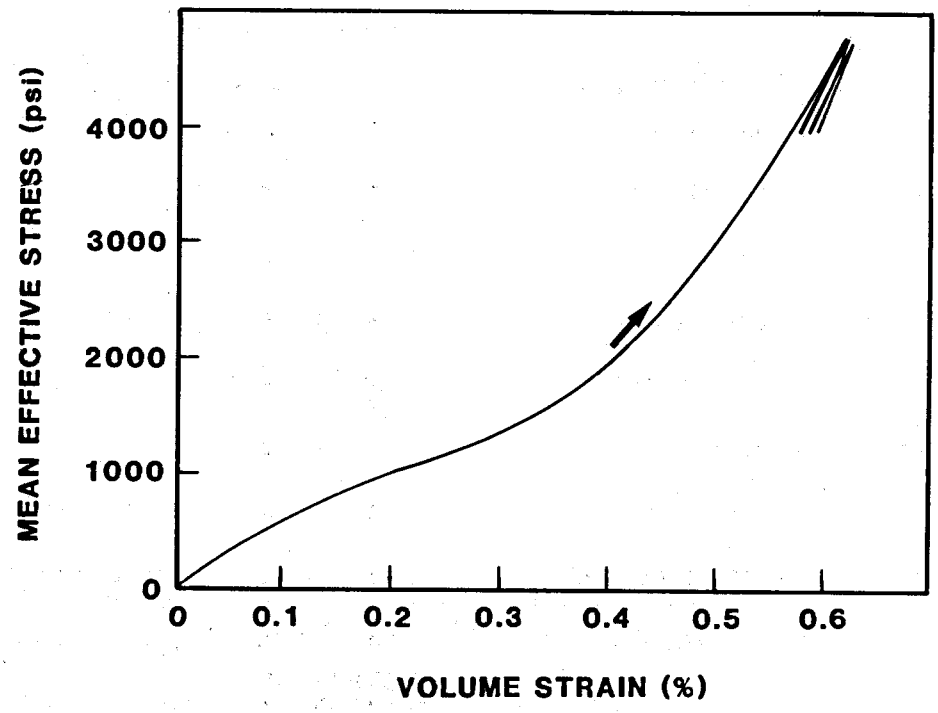

Figure 54. Pore pressure cycling test on material from Cerro Prieto well M-107, depth 6,936', porosity 18.9%, no shear stress, test temperature 150°C. Compressibility 0.6×10^{-6} psi^{-1} for effective stress increase and 0.5×10^{-6} psi^{-1} for effective stress decrease.

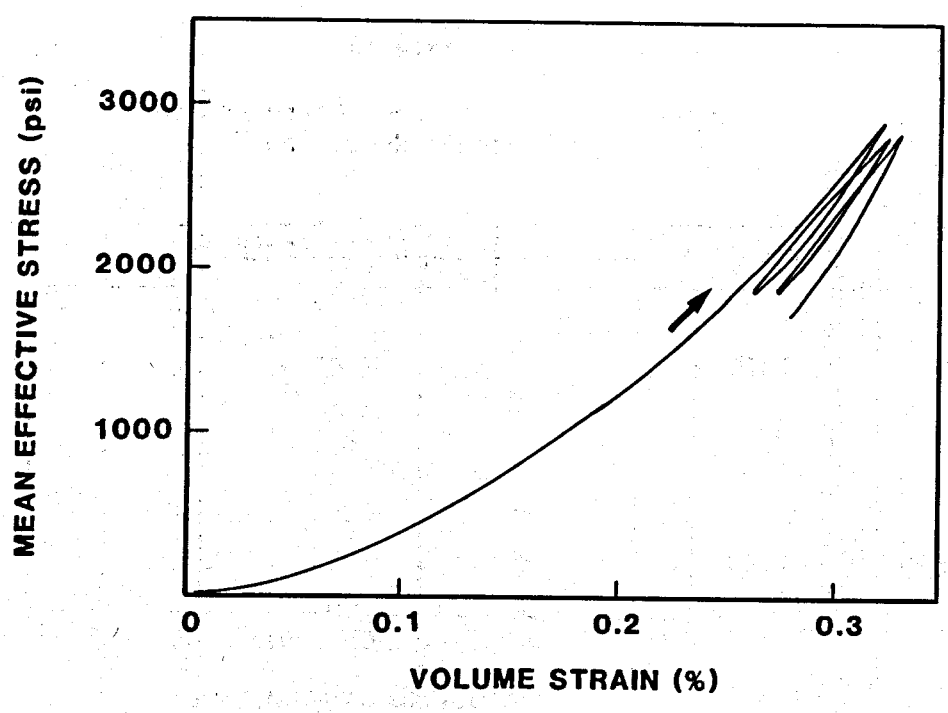

Figure 55. Pore pressure cycling test on material from Cerro Prieto well M-107, depth 6,936', porosity 18.6%, intermediate shear stress, test temperature 150°C. Compressibility 0.7×10^{-6} psi^{-1} for effective stress increase and 0.5×10^{-6} psi^{-1} for effective stress decrease.

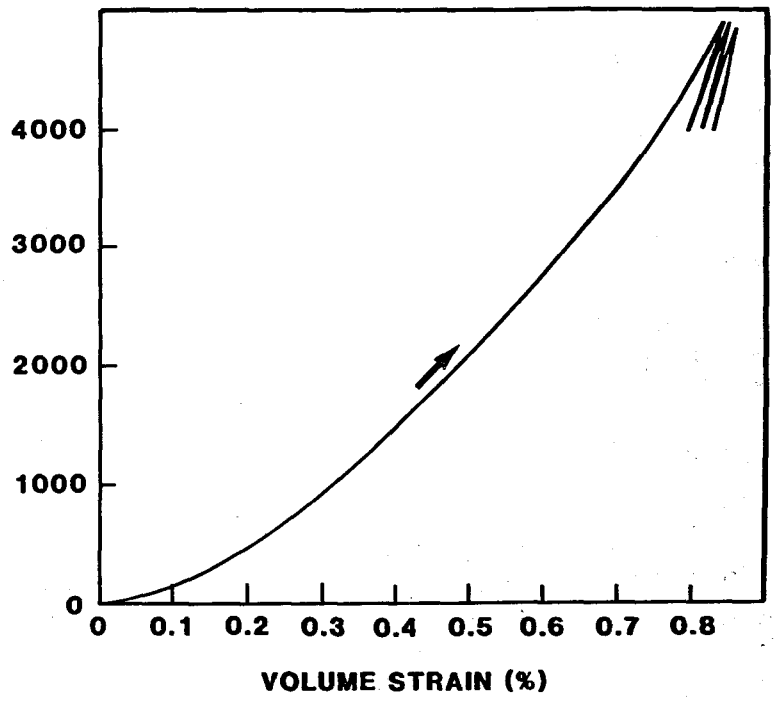

Figure 56. Pore pressure cycling test on material from Cerro Prieto well M-127, depth 7,136', porosity 19.6%, no shear stress, test temperature 150°C. Compressibility 0.8×10^{-6} psi^{-1} for effective stress increase and 0.4×10^{-6} psi^{-1} for effective stress decrease.

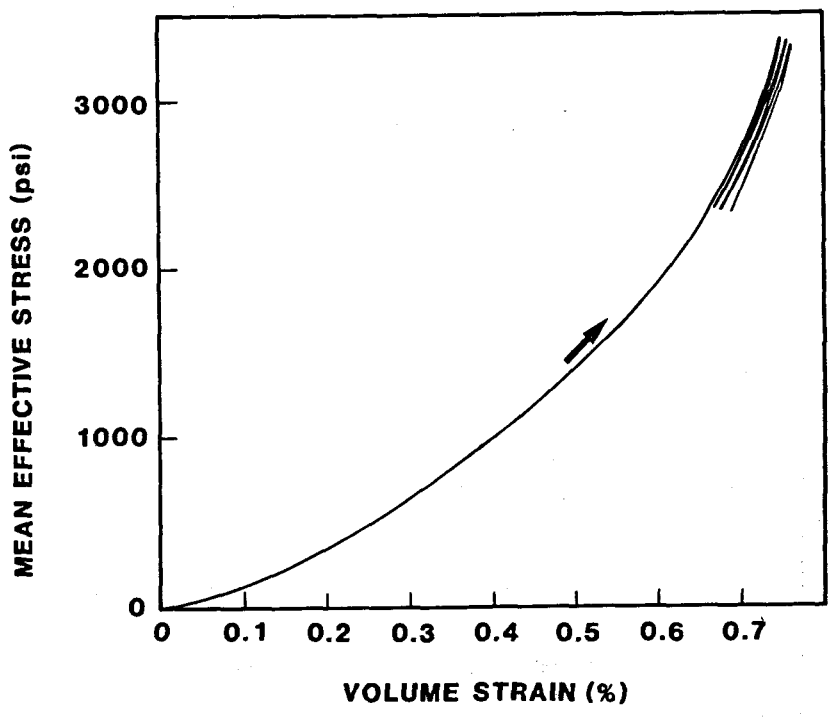

Figure 57. Pore pressure cycling test on material from Cerro Prieto well M-127, depth 7,136', porosity 19.4%, intermediate shear stress, test temperature 150°C. Compressibility 0.9×10^{-6} psi^{-1} for effective stress increase and 0.7×10^{-6} psi^{-1} for effective stress decrease.

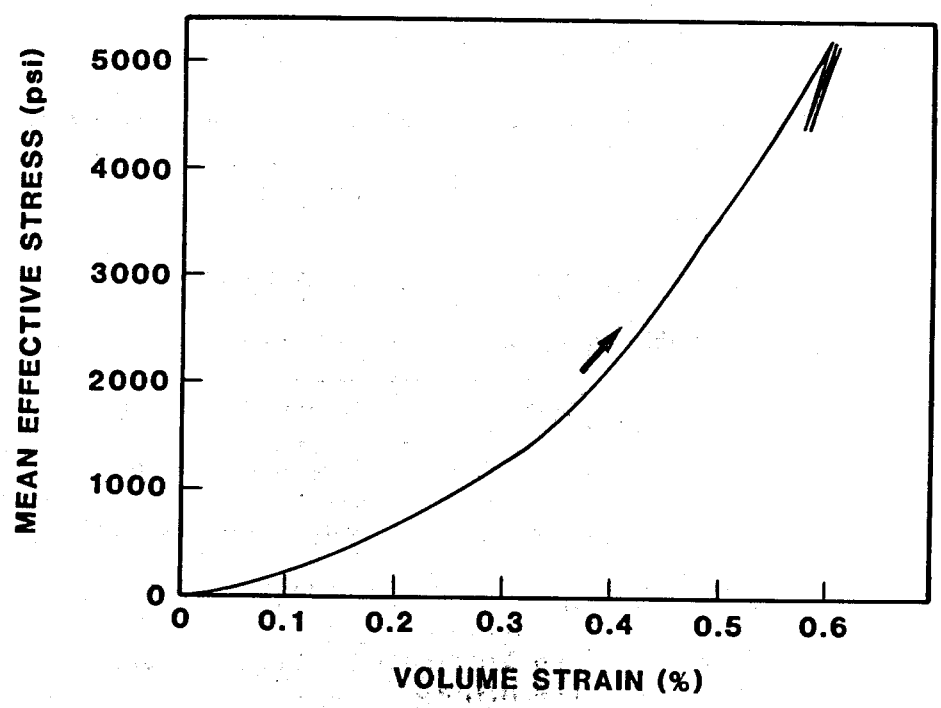

Figure 58. Pore pressure cycling test on material from Cerro Prieto well T-366, depth 8,010', porosity 19.6%, no shear stress, test temperature 150°C. Compressibility 0.6×10^{-6} psi^{-1} for effective stress increase and 0.3×10^{-6} psi^{-1} for effective stress decrease.

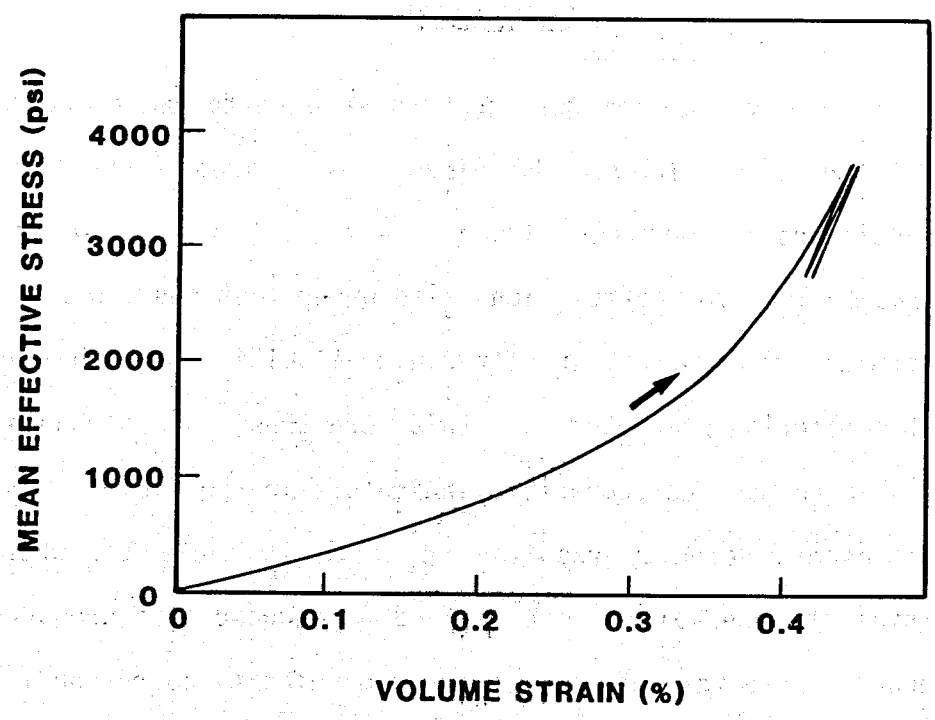

Figure 59. Pore pressure cycling test on material from Cerro Prieto well T-366, depth 8,010', porosity 19.3%, intermediate shear stress, test temperature 150°C. Compressibility 0.5×10^{-6} psi^{-1} for effective stress increase and 0.3×10^{-6} psi^{-1} for effective stress decrease.

highest deviatoric stress values, indicated that these sandstones were essentially elastic-brittle in nature as compared to the East Mesa material previously tested.

4.2.3 Confining Pressure Cycling and Uniaxial Compaction

Three tests on the same material, as described also in the previous section, for the case of intermediate load and confining pressure cycling are shown in Figures 60, 61 and 62. Results were similar to the previous results. There was possibly a small trend to larger compressibility, which would be consistent with a non-zero grain compressibility which would alter the Terzaghi effective stress. Uniaxial compaction results, shown in Figures 63, 64 and 65 indicated a slight tendency to greater compressibility; however, the change was not marked and it was consistent with the relatively elastic short-term response of the Cerro Prieto material tested.

4.2.4 Ultrasonic Velocities

Ultrasonic velocities measurements were performed on Cerro Prieto material from the three wells as described above. These were done both at reservoir conditions and at reduced pore pressure. The purpose of these measurements was to look for correlations with other test results and, in particular, to determine the extent that ultrasonic velocities might be sensitive indicators of compaction phenomena. If this were true, then downhole sonic measurements could be used as compaction indicators in the field.

Ultrasonic velocity results are shown in Table 14, where P and S wave velocities at reservoir conditions and at reduced pore pressure (by 1000 psi) are shown. There was a change in average velocity corresponding to compaction of 1-2%. This change, although significant, was probably not large enough to be readily discernible downhole, considering the perturbing influences of

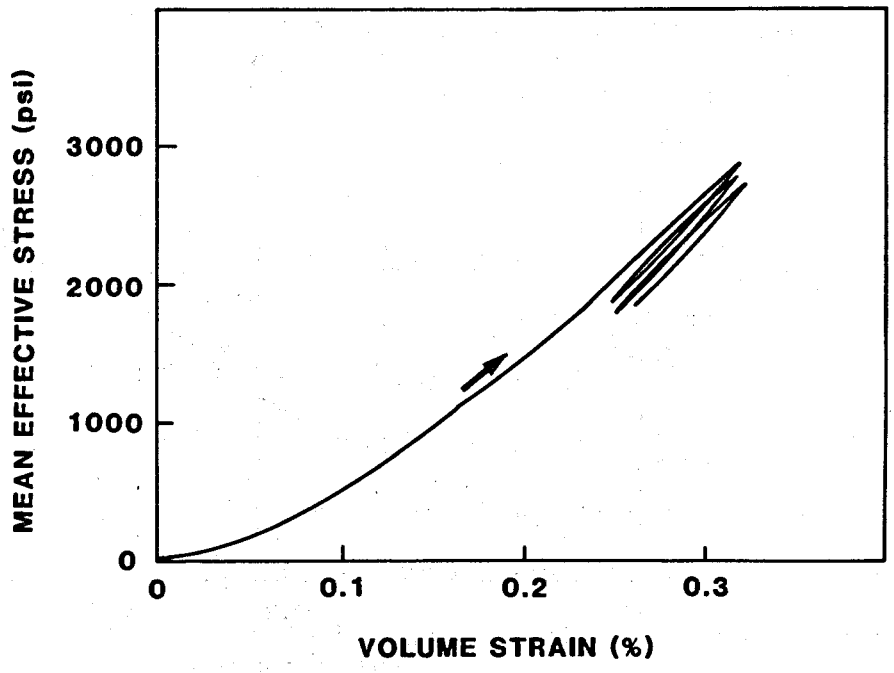

Figure 60. Confining pressure cycling test on Cerro Prieto material from well M-107, depth 6,936', porosity 18.3%, test temperature 150°C, intermediate shear stress. Compressibility 0.8×10^{-6} psi^{-1} for effective stress increase and 0.6×10^{-6} psi^{-1} for effective stress decrease.

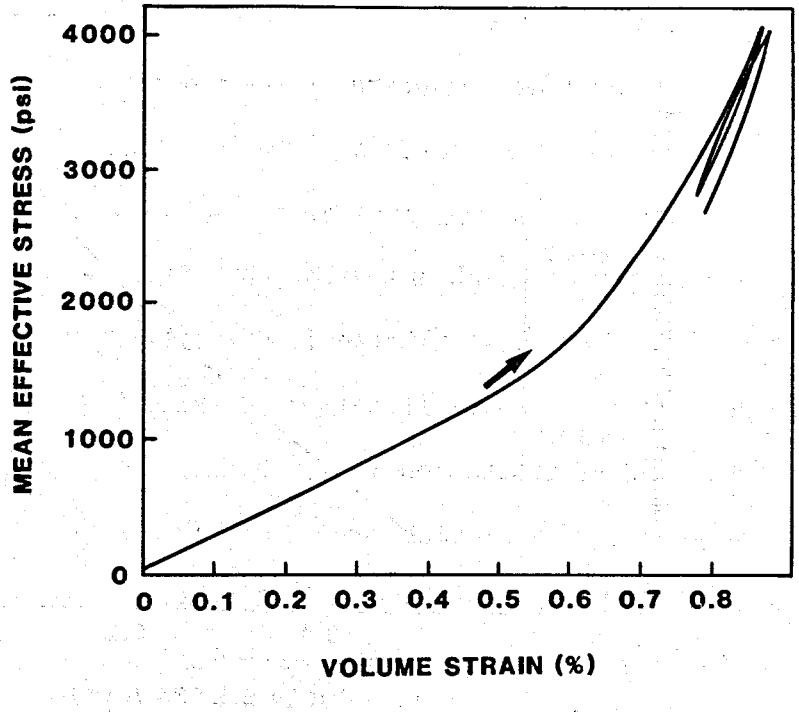

Figure 61. Confining pressure cycling test on Cerro Prieto material from well M-127, depth 7,136', porosity 20.4%, test temperature 150°C, intermediate shear stress. Compressibility 1.0×10^{-6} psi^{-1} for effective stress increase and 0.7×10^{-6} psi^{-1} for effective stress decrease.

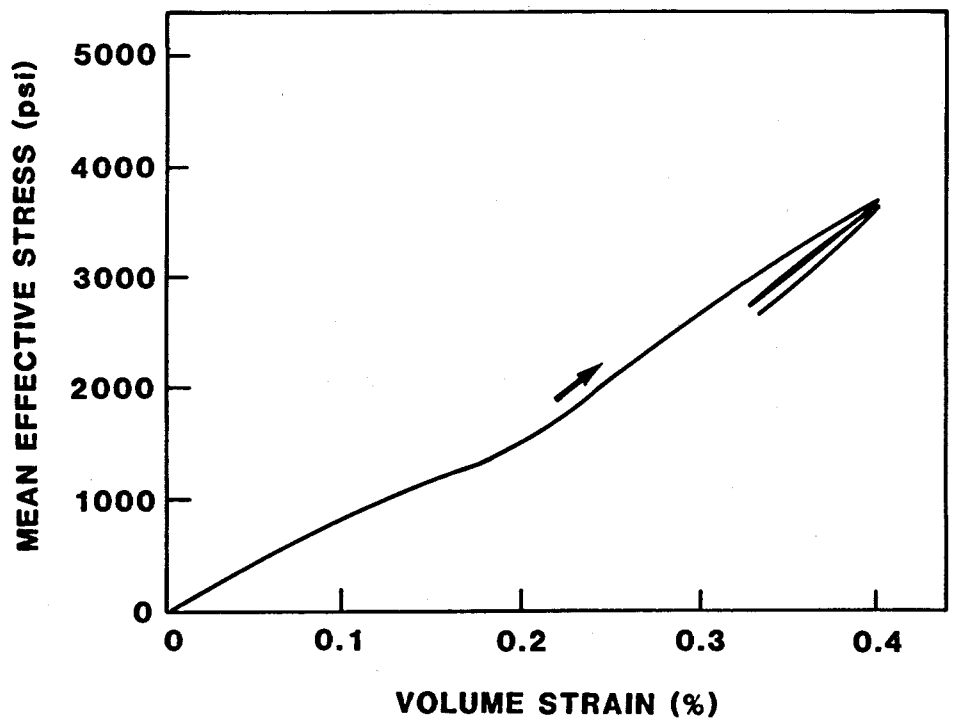

Figure 62. Confining pressure cycling test on Cerro Prieto material from well T-366, depth 8,010', porosity 19.8%, test temperature 150°C, intermediate shear stress. Compressibility 1.0×10^{-6} psi^{-1} for effective stress increase and 0.8×10^{-6} psi^{-1} for effective stress decrease.

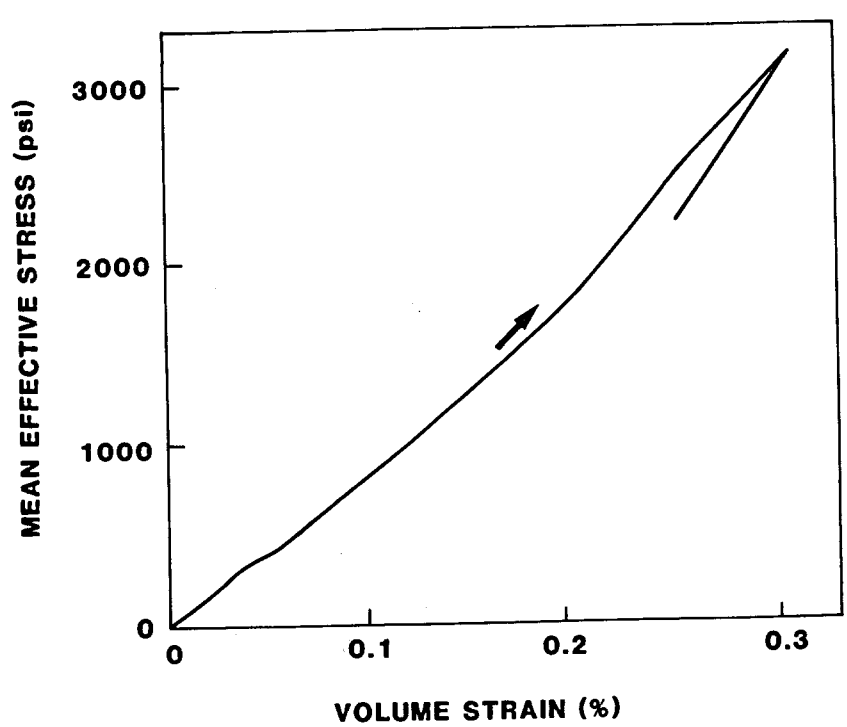

Figure 63. Uniaxial compaction test on material from Cerro Prieto well T-366, depth 8,010', porosity 19.3%, test temperature 150°C, compressibility 0.8×10^{-6} psi^{-1}.

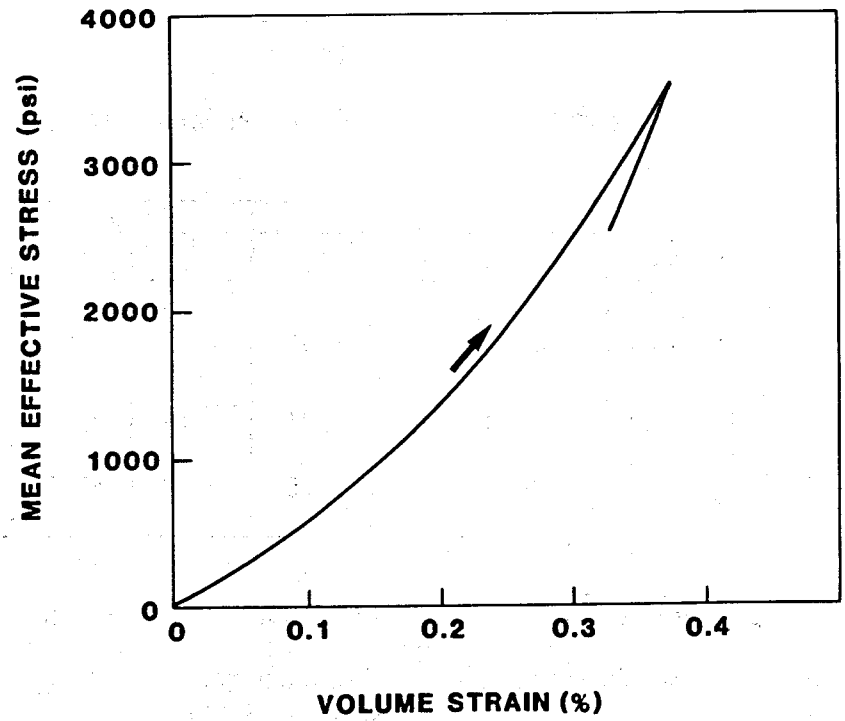

Figure 64. Uniaxial compaction test on material from Cerro Prieto well M-127, depth 7,136', porosity 21.6%, test temperature 150°C, compressibility 0.7×10^{-6} psi^{-1}.

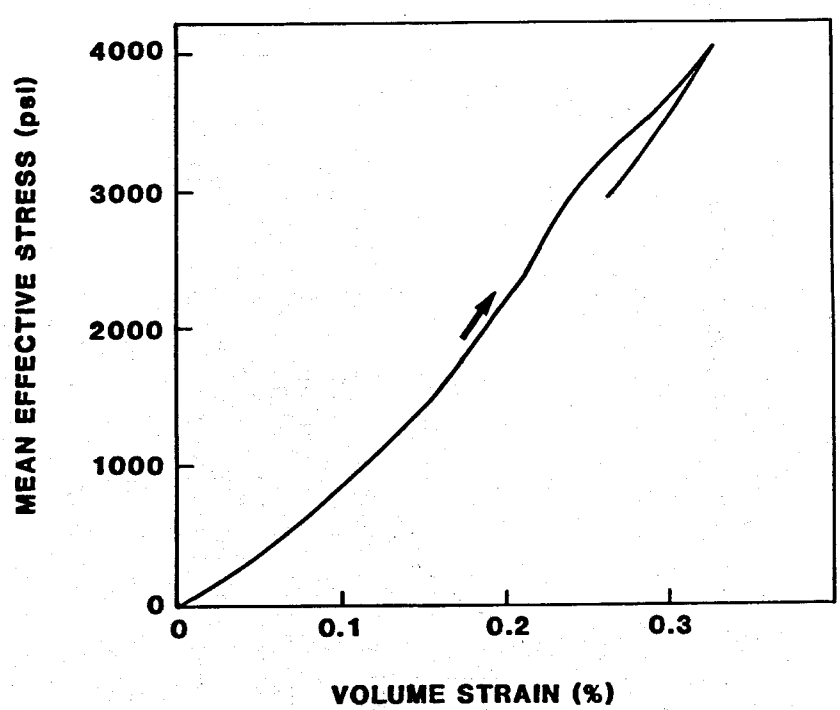

Figure 65. Uniaxial compaction test on material from Cerro Prieto well M-107, depth 6,936', porosity 18.4%, test temperature 150°C, compressibility 0.9×10^{-6} psi^{-1}.

Table 14

Ultrasonic Velocities, Cerro Prieto (km/s)

	M-107		M-127		T-366		Average	
	V_p	V_s	V_p	V_s	V_p	V_s	V_p	V_s
Reservoir Conditions	4.01	2.52	3.82	1.96	4.03	2.61	3.95	2.36
Reduced P_p	4.06	2.57	3.90	2.01	4.05	2.66	4.00	2.41
Change (%)	+1.1	+2.0	+2.1	+2.5	+0.4	+1.7	+1.3	+2.2

other mechanisms, such as noise caused by fluid flow, tectonics, thermal fluctuations, etc. Nevertheless, in the laboratory, the change was consistent, easily measurable, and repeatable.

5. CREEP TESTING RESULTS

Basic testing, as described in the previous chapter, succeeded in determining the short-term compressional response properties of Cerro Prieto and East Mesa cores. The loading duration of these short-term tests was, in most cases, less than one hour. Some evidence of time-dependent inelastic response was observed. This suggested long-term creep compaction might be observed if large effective stresses were maintained for long periods of time. The purpose of creep testing, therefore, was to determine the extent that compaction is time-dependent, thus making long-term effective compressibilities larger than those measured in short-term tests. Additionally, since reservoir permeabilities may be affected by long-term compaction, several creep tests also included measurements of permeability.

A summary of creep tests that were completed is shown in Table 15. The first group of four tests, on material from the East Mesa reservoir (labeled EM-1 thorugh EM-4), were primarily debugging tests for the modified creep machine and new jacketing procedures. The next group of nine tests on Cerro Prieto material (labeled CP-1 through CP-9) were tests with considerable emphasis placed on measurements of permeability. The final group of tests (labeled EM-5 through EM-8, and CP-10 through CP-12) were long-term creep tests. Individual results for each of these tests are given in separate sections below.

Tests of East Mesa material were generally run at temperatures in the range 150°C to 160°C. For Cerro Prieto material, tests were generally run in the range 250°C to 300°C. In the cases where tests are labeled "triaxial", total overburden stress was set equal to one psi per foot of burial, pore pressure was set by assuming a normal hydrostatic gradient, and confining

Table 15

Creep Test Summary

Test I.D.	Well	Test Type	Duration	Creep Data	Permeability Data					Rock Class
					High P Low T	High P High T	Pre Creep	Post Creep	Final	
EM1	78-30	Triax	1 day	√						Fine Grained Sandstone
EM2	78-30	Triax	120 min	√						Fine Grained Sandstone
EM3	78-30	Triax	1 day	√						Fine Grained Sandstone
EM4	78-30	Triax	1 day	√						Fine Grained Sandstone
CP1	M127	Triax	450 min	√	√	√	√			Fine Grained Sandstone
CP2	M110	Triax	500 min	√	√	√	√			Fine Grained Sandstone
CP3	0473	Triax	550 min	√	√		√	√	√	Very Fine Grained Sandstone
CP4	T366	Triax	350 min			√	√	√	√	Very Fine Grained Sandstone
CP5	M7	Triax	160 min	√			√	√		Medium Grained Sandstone
CP6	M107	Triax	130 min	√	√	√	√	√	√	Coarse Grained Sandstone
CP7	M129	Triax	170 min	√			√	√		Coarse Grained Siltstone
CP8	NL1	Triax	120 min	√	√	√	√	√	√	Fine Siltstone
CP9	M93	Triax	220 min	√	√	√		√		Medium Grained Sandstone
EM5	78-30	Triax	3 days	√						Medium Grained Sandstone
EM6	78-30	Hydro	4 days		√					Fine Grained Sandstone
EM7	78-30	Hydro	19 days		√	√				Fine Grained Sandstone
EM8	58-30	Hydro	10 days							Very Fine Grained Sandstone
CP10	M127	Hydro								Fine Grained Sandstone
CP13	M107	Hydro	5 days	√	√					Coarse Grained Sandstone

pressure was set so that the ratio of effective oveburden to effective lateral stress was approximately three to two. For the tests labeled "hydrostatic", confining pressure was set equal to one psi per foot of burial and pore pressure was assumed to be hydrostatic. In most cases, only axial strains were measured during the creep tests*. Resolution of creep strain was about $1x10^{-4}$/day or $1x10^{-9}$/sec ($1x10^{-7}$ %/sec). Creep results are presented here as curves of volume strain versus time. For constant grain volume and small strains, the volume strain versus time curves may be treated also as porosity change versus time curves.

5.1 Initial Creep Tests, East Mesa

The results of the first four creep tests are given in Figures 66-69. The drop in volume strain seen at zero time is the initial reduction caused by a 1000 psi pore pressure reduction from initial in-situ conditions. Note the similarity among test results. There is an initial, somewhat rapid creep rate, which then tapers off to what appears to be a steady-state creep rate. Caution in interpretation is necessary. The apparent steady-state could be the early part of an extremely long-duration time-dependent curve and this would be difficult to discern. If the test that was aborted early due to machine difficulties (shown in Figure 67) is ignored, the average long-term creep rate for these tests is $4.1x10^{-9}$/sec. At this rate, the instantaneous strain seen in this rock as caused by initial pore pressure reduction would be doubled by creep effects in approximately three days time and all porosity would be removed in approximately 500 days time. These tests indicate that creep is a significant phenomenon in these rocks.

*Early creep testing indicated that the lateral strain system, which utilized strain-gauged cantilevers, was subject in some cases to more long-term drift than the axial strain system, which utilized LVDT's. Therefore, to obtain maximum resolution for purposes of creep compaction measurement, only the higher resolution axial strain LVDT measurements were used.

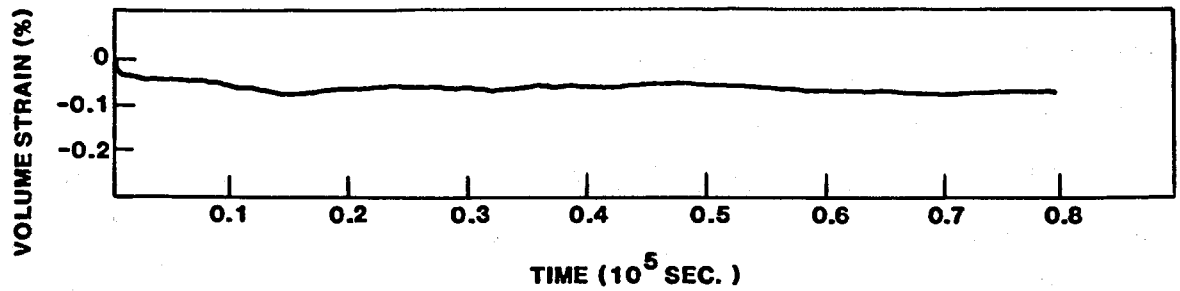

Figure 66. Creep compaction test on material from East Mesa well 78-30, depth 7,142', creep rate approximately 3.3×10^{-9} sec^{-1}.

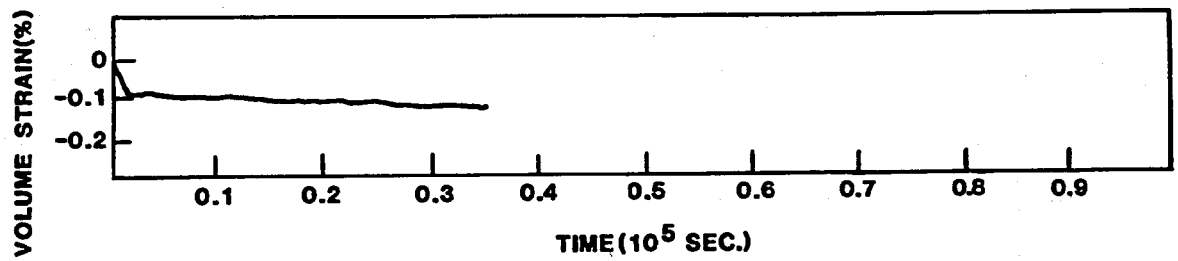

Figure 67. Creep compaction test on material from East Mesa well 78-30, depth 7,144', creep rate approximately 15.0×10^{-9} sec^{-1}.

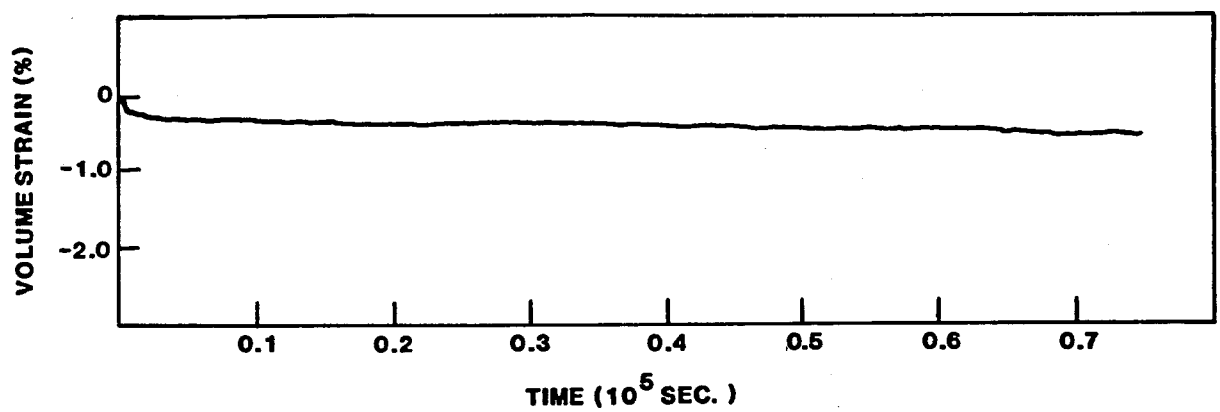

Figure 68. Creep compaction test on material from East Mesa well 78-30, depth 5,510', creep rate approximately 2.4×10^{-9} sec^{-1}.

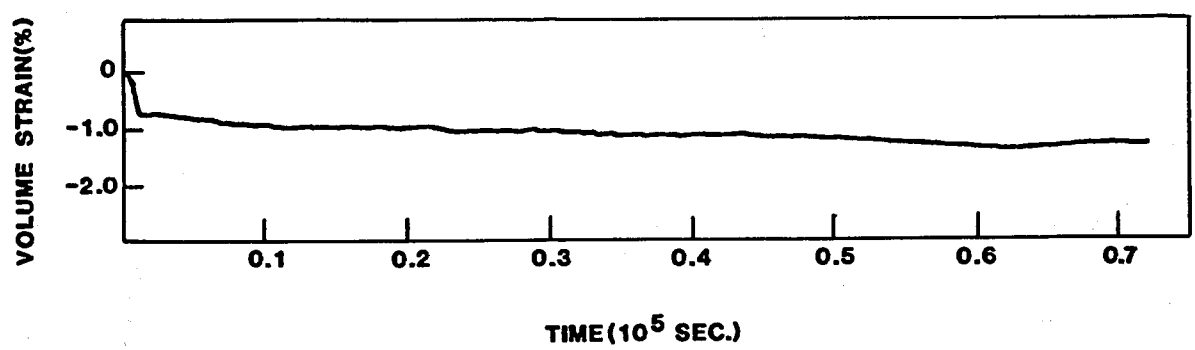

Figure 69. Creep compaction test on material from East Mesa well 78-30, depth 5,500', creep rate approximately 6.7×10^{-9} sec^{-1}.

5.2 Initial Creep Tests, Cerro Prieto

The next eight tests were conducted on material from nine different wells at Cerro Prieto. Creep duration ranged from 120 minutes to 550 minutes and permeabilities were measured several times during each test. The description of results will be separated into two subsections: the first describing volume strain results, and the second describing permeability results.

5.2.1 Volume Strain Results

The volume strain results are given in Figures 70 through 77. For sandstones, as material becomes coarser-grained, creep becomes more noticeable. All siltstones tended to creep at greater rates; however, results are highly variable. Creep amounts in these materials vary from little or none in rocks from Wells M-127, M-110, 0473 and NL-1. Note that these materials all contain little or no calcite (see Table 5). Higher creep rates are observable in samples from wells M-7, M107 and M-129. These all tend to be siltstones coarser-grained sandstone materials. Finally, an extremely high creep rate is observed in the sample from well M-93. This sample was fine grained sand, very friable, had high fines fraction and porosity, and was clearly different from other materials obtained from wells at Cerro Prieto. In fact, with its high initial creep rate, it perhaps behaved more as a soil than as a rock. When all results except well M-93 are averaged, the observed creep rate is 7.2×10^{-9}/sec, which is somewhat greater than the rate observed for East Mesa material. However, the duration of creep for these tests was less than for the East Mesa tests previously shown. Since observed creep was more rapid at earlier times, the greater rates for Cerro Prieto rocks may be somewhat misleading. If one considers only at the longer-term Cerro Prieto tests, as shown in Figures 70, 71 and 72, the average creep rate is somewhat less than

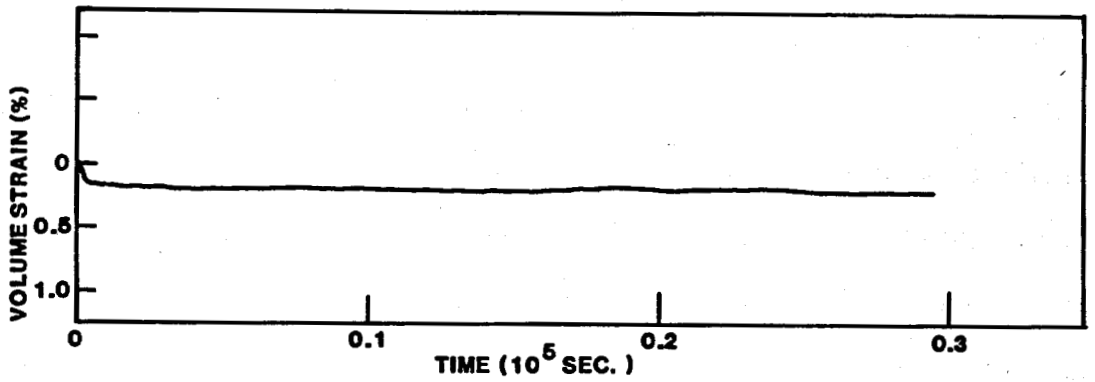

Figure 70. Creep compaction test on material from Cerro Prieto well M-127, creep rate is less than 2.0×10^{-9} sec^{-1}.

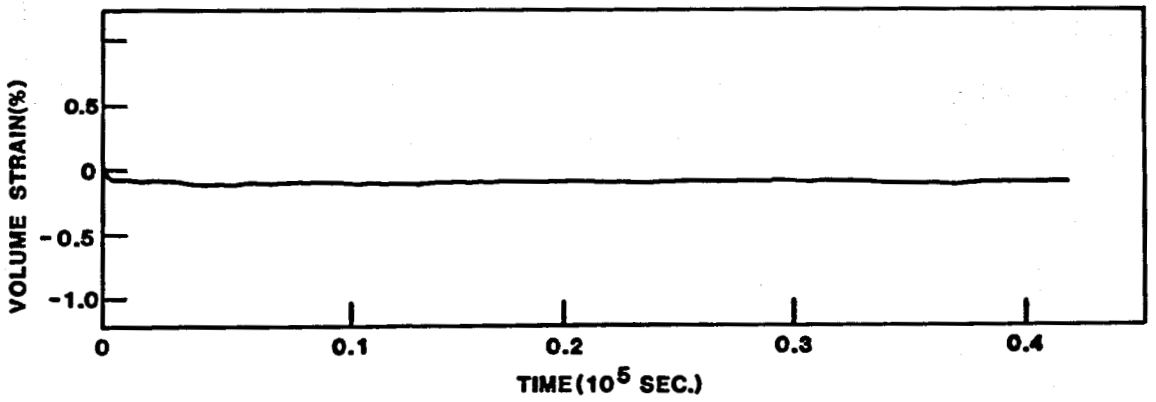

Figure 71. Creep compaction test on material from Cerro Prieto well M-110, creep rate is less than 2.0×10^{-9} sec^{-1}.

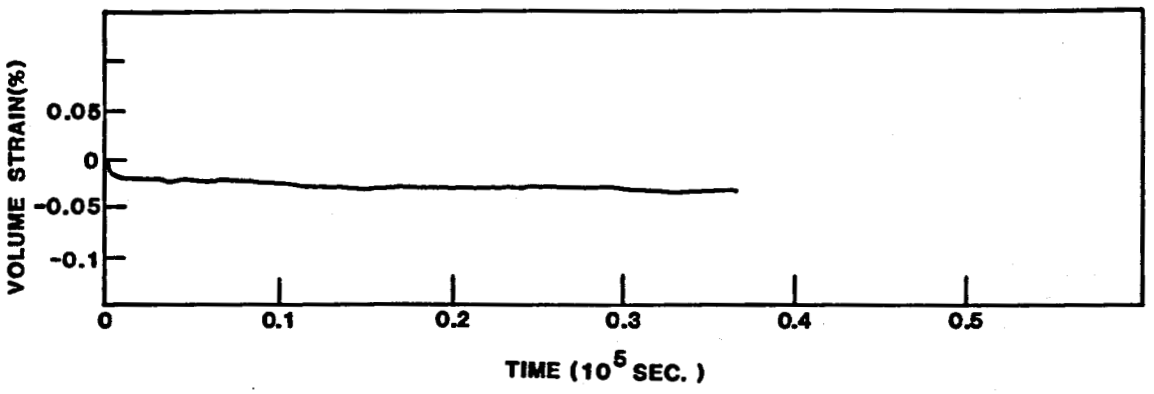

Figure 72. Creep compaction test on material from Cerro Prieto well 0473, creep rate is approximately 1.7×10^{-9} sec^{-1}.

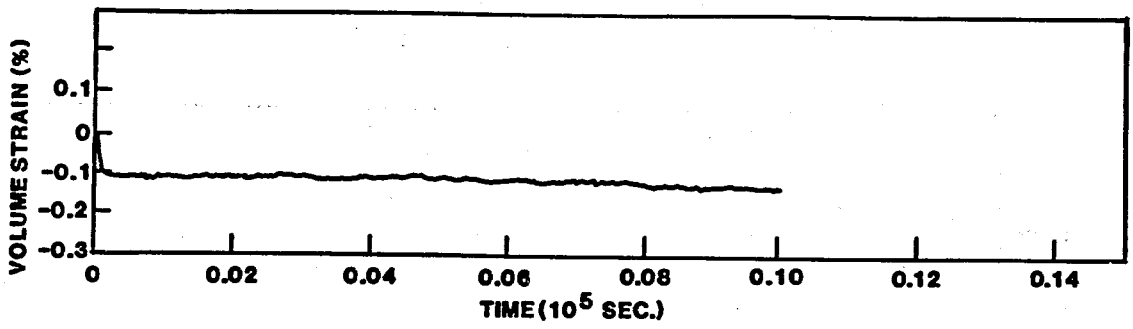

Figure 73. Creep compaction test on material from Cerro Prieto well M-7, creep rate is approximately 10.0×10^{-9} sec^{-1}.

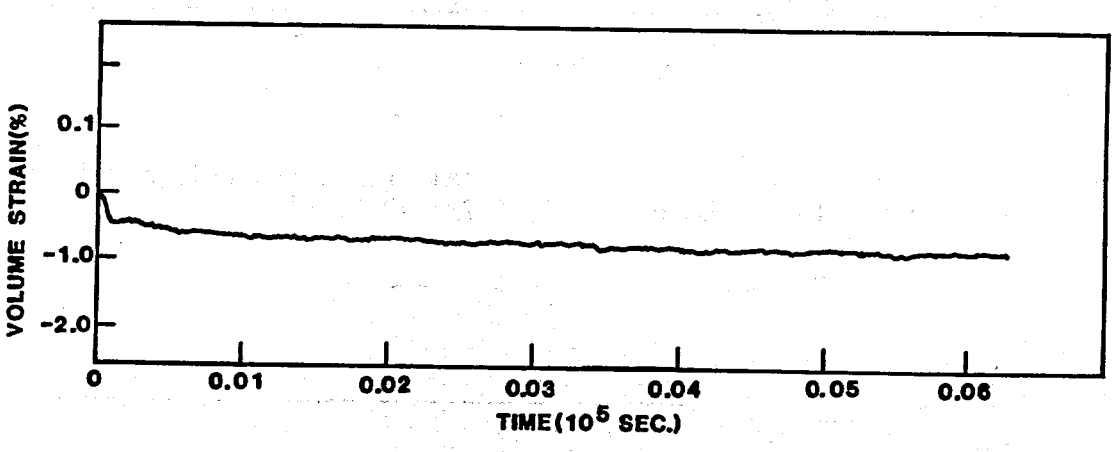

Figure 74. Creep compaction test on material from Cerro Prieto well M-107, creep rate is approximately 18.6×10^{-9} sec^{-1}.

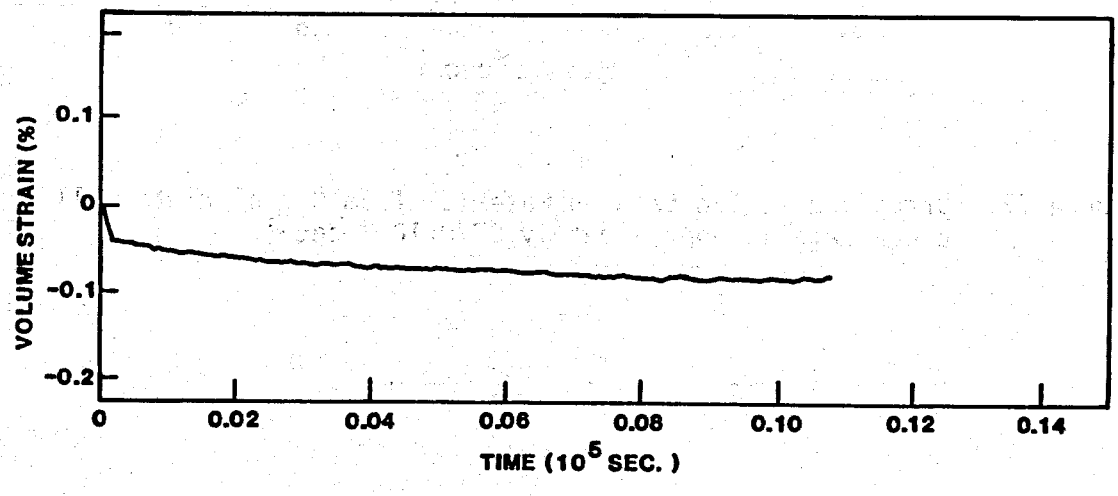

Figure 75. Creep compaction test on material from Cerro Prieto well M-129, creep rate is approximately 13.3×10^{-9} sec^{-1}.

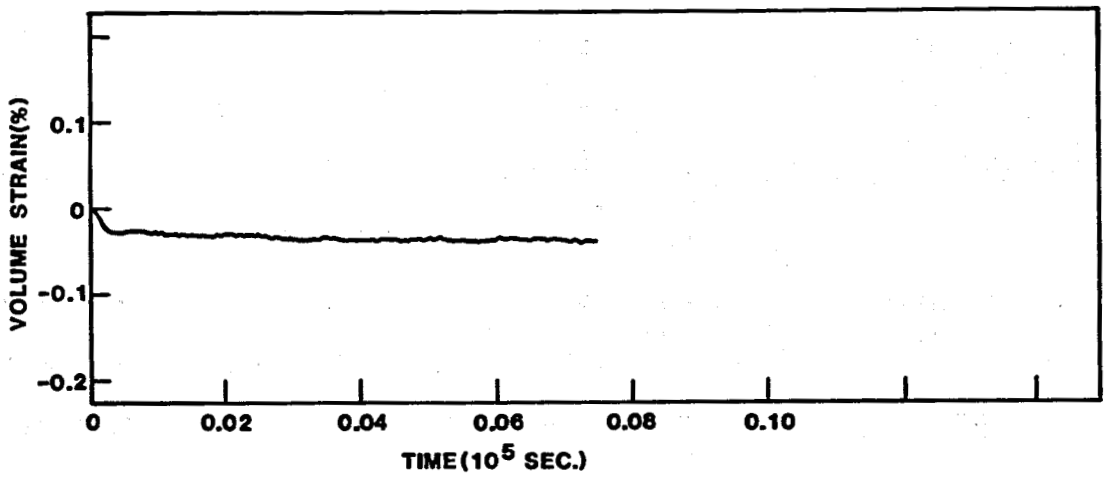

Figure 76. Creep compaction test on material from Cerro Prieto well NL-1, creep rate is approximately 2.7×10^{-9} sec^{-1}.

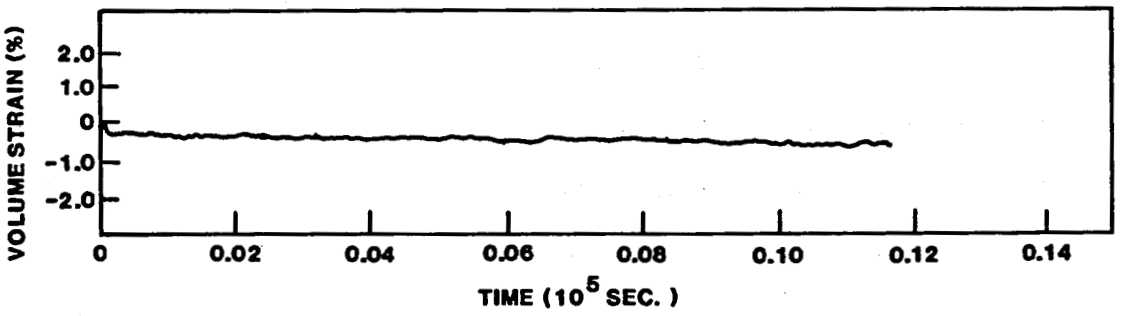

Figure 77. Creep compaction test on material from Cerro Prieto well M-93, creep rate is approximately 87.0×10^{-9} sec^{-1}.

$2x10^{-9}$/sec, which is less than half of that which was observed for the East Mesa material.

In general, the results for Cerro Prieto material are more variable than those for East Mesa material, which should not be surprising considering the greater number of wells from which material was obtained for testing from Cerro Prieto. For longer terms, the Cerro Prieto material perhaps exhibits less creep than the East Mesa material, with the notable exception of the unconsolidated material from Cerro Prieto well M-93, which shows more than an order of magnitude greater creep than the average of all materials tested here.

5.2.2 Permeability Results

The permeability results, which are shown in Table 16, are quite variable. During permeability testing, it became evident that fluid chemistry was playing an important role in the fluid-flow related behavior of this material. As will be seen in the fluid chemistry results section, this was particularly noticeable in the case of rocks that contained relatively large amounts of calcite. The carbonate equilibrium seemed to control the amount of fines that could be released from the rock. As a result, there were extreme problems with plugging of high carbonate rock in permeability tests. Results are averaged in the last line of Table 16 and are shown in terms of initial average values and changes from those average as percentages from the previous value. The average permeability measured was about 4 millidarcies. With increased temperature, there was a reduction of permeability by about 40%. One standard deviation of this value is about 23%, so this reduction is moderately significant. With pore pressure reduction to increase effective stress, there is no significant change in permeability. With creep, there was a reduction of approximately 39 ± 18%, which is significant. With final pore

Table 16

Permeabilities, Cerro Prieto (md)
(All at In Situ Pressures)

	Room Temp.	Elev. Temp.	Pp Red.	Post Creep	Pp Inc.	Comments
CP1 M127	1.8	1.7	1.3	--	--	Low Calcite
CP2 M110	1.0	0.7	0.8	--	--	Low Calcite
CP3 0473	3.0	--	0.14	0.07	0.13	
CP4 T366	--	0.70	0.76	0.37	0.40	Low Calcite
CP5 M7	--	--	6.0	3.0	--	
CP6 M107	0.5	0.22	0.21	0.11	0.20	Low Calcite
CP7 M129	--	--	0.25	0.23	--	
CP8 NL1	3.0	1.2	1.2	0.9	0.9	Low Calcite
CP9 M93	14.5	7.3	--	5.8	--	
Avg.	4.0	Temp Chg. -40% ± 23%	Pp Chg -1% ± 15%	Creep Chg -39% ± 18%	Pp Inc. +44% ± 46%	

pressure increase, there was considerable scatter in results, but with statistical significance, there was no change in permeability from post-creep values.

To summarize, we have seen that in rocks from Cerro Prieto, permeability is reduced by increase of temperature to near in-situ conditions by creep, but not reduced in conjunction with the instantaneous reduction of pore pressure. This is interesting because for the duration of these creep tests the total creep strains were not larger than the instantaneous strains caused by pore pressure reduction. There are two possible explanations for this. One is that the permeability reductions associated with creep are somewhat anomalous having been caused by particulate plugging as a result of chemical non-equilibrium effects. However, indications of non-equilibrium were small for the tests on low-calcite material. Therefore, the second reason that creep causes high stress concentration areas in the vicinity of pore throats to selectively close is perhaps plausible at least for low-calcite material. In this case, creep would be expected to reduce permeability more than quasi-elastic deformation.

5.3 Long-Term Creep Tests, East Mesa

Four long-term creep tests were run on the material from the East Mesa reservoir. Three were on material from the production zones of Well 78-30 and one was on the fine-grained caprock material from well 58-30. The average duration of these tests was 9×10^5 seconds or about 10 days. In these tests, the production zone material creeped at a rate of about 1×10^9/sec causing total deformation at the end of the tests that was more than twice that of the instantaneous deformation at the beginning of the tests. The fine grained caprock material from well 58-30, however, ceased to apparently creep after about two to three days (although its initial creep rate was large). It

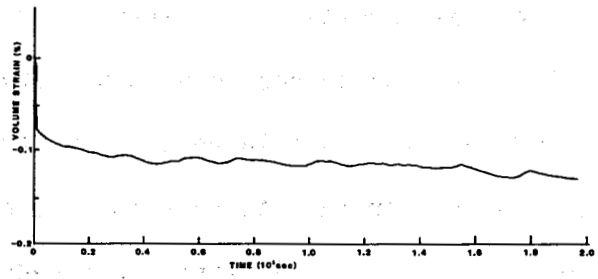

Figure 78. Long-term creep test on material from East Mesa well 78-30, creep rate is approximately 1.3×10^{-9} sec^{-1}.

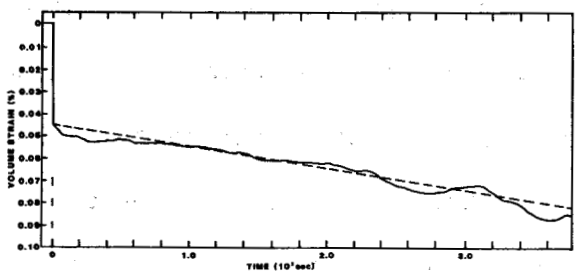

Figure 79. Long-term creep test on material from East Mesa well 78-30, creep rate is approximately 1.0×10^{-9} sec^{-1}.

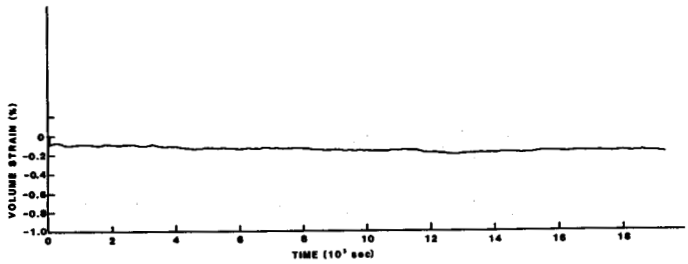

Figure 80. Long-term creep test on material from East Mesa well 78-30, creep rate is approximately 0.6×10^{-9} sec^{-1}.

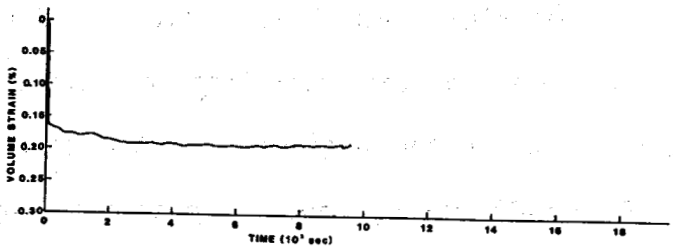

Figure 81. Long-term creep test on material from East Mesa well 58-30, creep rate is approximately 0.0×10^{-9} sec^{-1}.

cannot be ascertained whether creep truly stopped or whether the final creep rate in this material was below the resolution of the equipment. These results are summarized in Figures 78 through 81. Permeabilities were measured on these materials and did not differ significantly from the previously measured permeabilities.

5.4 Long-Term Creep Tests, Cerro Prieto

Although several tests were attempted, the extremely high temperatures commonly caused premature jacket failure and, in general, prevented the running of an extremely long creep test at temperatures near 300°C. One successful test was run on material from Well M-107 to about five days duration, as shown in Figure 82. The creep rate at the end of this time was quite small. Permeabilities of this material did not differ significantly from previous values.

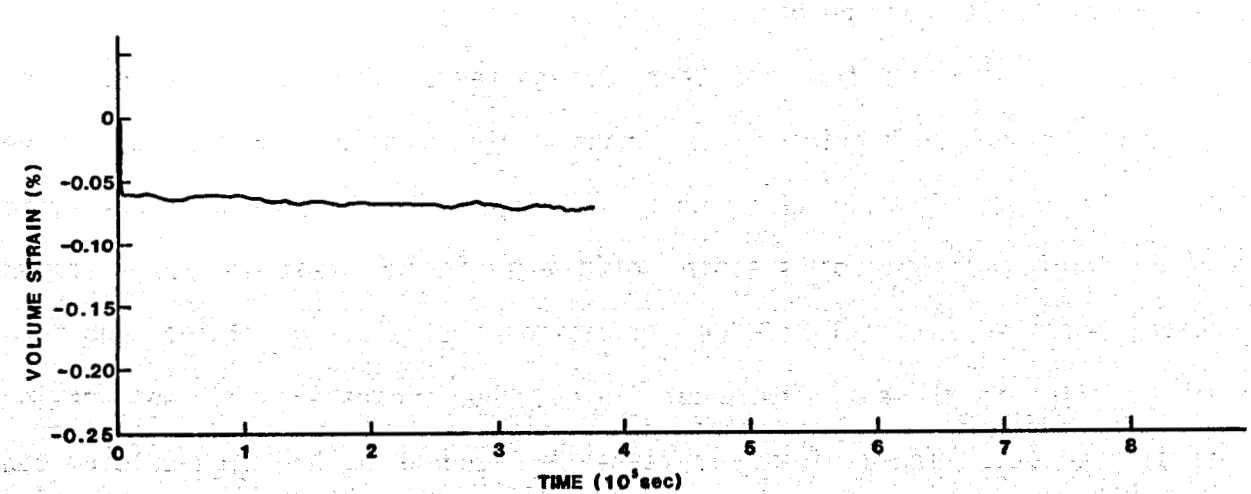

Figure 82. Long-term creep test on material from Cerro Prieto well T-366, creep rate is approximately 0.3×10^{-9} sec^{-1}.

6. FLUID CHEMISTRY RESULTS

Results of analyses performed on fluids from the East Mesa and Cerro Prieto tests are given in Tables 17 and 18, respectively. Test conditions are also listed. The most interesting information in the East Mesa table is the correlation between the pre-test flushing of fluid through the specimen and fluid chemistry. Tests EM-1 through EM-4 were flushed with two or three pore volumes of fluid prior to testing and tests EM-5 through EM-8 were flushed with several tens of pore fluid prior to testing. The effect of pre-test flushing is borne out by the change in sodium and bicarbonate pick-up between the two sets of tests. Clearly, considerable salt residue is left in these cores upon recovery and only a few pore volumes of flushing is not sufficient to remove it from the core. This result led us to decide, for all remaining procedures, to use flushings of several tens of pore volumes of fluid before the test sequences were begun.

Analyses of fluid from the Cerro Prieto tests, shown in Table 18, give a good overview of rock-brine interactions during testing. Excluding the results from tests CP-4 and CP-5, where problems with the pore pressure system caused brief occasions of flashing of the fluid to steam in the specimen, sodium, potassium and chloride concentrations in the output fluids tend to be quite similar to those in the input fluids, thus indicating that most residue was cleaned out. The fluids from tests CP-7 and CP-9 show high calcium concentrations, which correspond to the very high calcium carbonate contents in the rock (6-8% $CaCO_3$). These values emphasize the importance of choosing good rock-brine matches for high temperature testing.

The most critical fluid constituents, from the viewpoint of brine-rock mechanical interactions, are silica, calcium and bicarbonate. Table 19 sum-

Table 17

East Mesa
Fluid Chemistry Summary

	Test Number	EM1	EM2	EM3	EM4	EM5	EM6	EM7	EM8	Input Fluid
	Rock I.D.	A9	B56	B54	A11	A17	A18	B55	C35	
TEST CONDITIONS	Confining Press., psi	3700	4800	4800	3700	3700	5600	7200	3400	
	Axial Load, psi	1900	2400	2400	1900	1900	0	0	0	
	Pore Press. psi	1300	1300	1900	1300	1300	1300	1900	380	
	Temperature °C	165	175	175	165	22	175	175	150	
	Duration Days	2	2	2	2	5	14	26	16	
	Comments	Jacket Failure	Possibly Flashed			Only Low Temp. Test	500 ml Flush	500 ml Flush	Low Perm.	Synthetic Brine
FLUID PROPERTIES	pH	8.7	6.7	7.1	7.7	--	8.7	5.2	--	5.5-6.5
	Sulfate SO, ppm	--	--	--	--	--	1500	1400	--	350
	Calcium Ca^{++}, ppm	--	--	--	--	--	≤10	≤10	--	10
	Sodium Na^{+}, ppm	2000	1000	3000	3000	--	340	300	--	650
	Chloride Cl^{-}, ppm	--	--	--	--	390	680	760	--	350
	Potassium K^{+}, ppm	--	--	--	--	--	30	80	--	30
	Silica SiO_2, ppm	--	--	--	--	--	75	100	--	180
	Bicarbonate HCO_3^{-}, ppm	--	--	7500	7700	--	1400*	800*	--	780

*Bicarbonate was converted to aqueous CO_2 by injecting acid into the pressurized brine.

Tolerances:		
	pH	±0.3
	SO_4	20%
	Ca	10 ppm
	Na	15%
	Cl	10%
	K	10%
	SiO_2	20%
	HCO_3	50%

Table 18

Cerro Prieto
Fluid Chemistry Summary

	Test Number	CP1	CP2	CP3	CP4	CP5	CP6	CP7	CP8	CP9	CP10	CP13*	Fluid In
	Rock I.D.	M127	M110	0473	T366	M7	M107	M129	NL1	M93	M127	T366	
TEST CONDITIONS	Confining Press., psi	2710	3250	2750	4950	2800	4150	3550	5400	3050	7400	7400	
	Axial Load, psi	0	1650	1750	2450	1400	2050	1750	2700	1550	0	0	
	Pore Press. psi	1370	1450	1650	2700	1100	2100	1650	3050	1300		2700	
	Temperature °C	250	250	250	250	250	250	250	250	250	250	250	
	Duration Hours	8	11	11	6	3	3	3	2	4	11 days	18 days	
	Comments	Jacket Failure			Flashed the Fluid	Flashed the Fluid					Jacket Failed Before Creep	Flushed With Two Liters of Fluid	Brine from the Cerro Prieto Field
	$CaCO_3$ In Rock %	0	0	1	0	1	0	8	0	6	0	0	
FLUID PROPERTIES	pH	--	--	7.2	7.1	6.7	7.5	6.7	7.0	6.7	--	7.5	5.5-6.5
	Calcium Ca^{++}, ppm	--	--	--	280	20	350	480	230	640	--	920	270
	Sodium Na^{+}, ppm	--	--	7000	6200	5900	8200	7300	6700	6600	--	27600	6000
	Chloride Cl^{-}, ppm	--	--	27000	11000	10000	14000	14000	12000	10000	--	35600	13000
	Potassium K^{+}, ppm	--	--	--	1300	1100	1500	1900	1400	540	--	3020	1200
	Silica SiO_2, ppm	--	--	610	290	440	3100	3300	2500	2300	--	150	650
	Bicarbonate HCO_3^{-}, ppm	--	--	850	470	340	800	420	620	1550	--	--	0

*CP11 and 12 experienced jacket failures before creep and before any fluid was sampled. The test conditions were identical to those for CP13.

Tolerances:		
	pH	±0.3
	Ca	20%
	Na	15%
	Cl	10%
	K	10%
	SiO_2	20%
	HCO_3	50%

Table 19

Silica and Carbonate Chemistry

Test I.D.	Fluid Detention Time	Silica		Calcium		Bicarbonate		$CaCO_3$ In Rock
		In	Out	In	Out	In	Out	
EM3	1/2 Day	--	--	--	--	100	2200	
	2 Days	--	--	--	--	100	2200	
EM4	2 Days	--	--	--	--	100	2200	
EM6	14 Days	180	75[1](490)[2]	10	<10	780	1400	
EM7	26 Days	180	220[2]	10	<10	780	>750	
CP3	11 Hours	1000	600	--	--	~0	850	1%
CP4[3]	1 Hour	680	380	300	320	0	180	0%
	6 Hours	680	290	300	280	0	470	0%
CP5[3]	3 Hours	680	440	300	20	0	340	1%
CP6	1 Hour	620	170	270	660	0	550	0%
	3 Hours	620	3100	270	350	0	800	0%
CP7	3 Hours	620	3300	270	480	0	420	8%
CP8	2 Hours	620	2500	270	230	0	620	0%
CP9	1 Hour	620	590	270	490	0	520	6%
	4 Hours	620	2300	270	640	0	1550	6%

[1]Sample was filtered through a 0.45 micron filter.

[2]No filtration of sample.

[3]The fluid from CP4 and CP5 was flashed before sampling.

marizes the analyses performed for these constituents for the East Mesa and Cerro Prieto creep tests. Concentrations of silica in the output fluid tend to be dependent upon the time the fluid was detained within the rock. This is summarized in Figure 83. For the Cerro Prieto tests, excluding CP-4 and CP-5, the analyses of fluids detained for approximately one hour show a loss of silica, which is probably due to a small thermal disequilibrium; however, fluid from Cerro Prieto tests with detention times greater than one hour, but less than a day, show a large increase of silica. Some concentrations briefly reached values as high as 3300 parts per million, which is greater than five times the initial value and greater than three times saturation. These values later drop to values equal to or below original values. (Fluid samples from the Cerro Prieto tests were not filtered and thus reported silica values include suspended, colloidal, and dissolved solids.) These high values are well

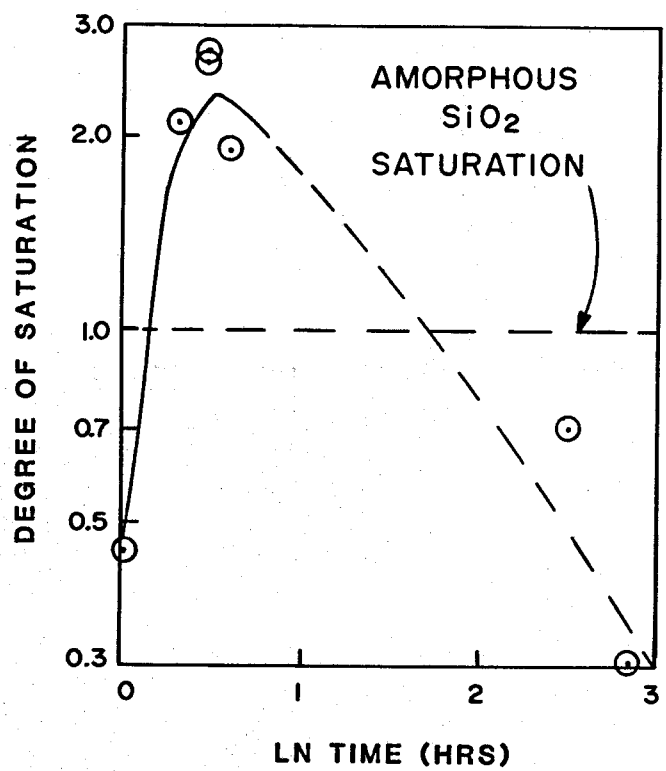

Figure 83. Concentration of silica with respect to degree of saturation for several Cerro Prieto creep tests as a function of time during the tests.

in excess of saturation concentration for silica even with respect to amorphous phases indicating the presence of other chemical, thermochemical or chemical-mechanical effects. The values reported for silica concentration during tests EM-6 and EM-7, which had 14 and 26 day detention times respectively, show that the long-term trend is toward dissolution and not precipitation of silica. The values 490 and 220 parts per million for tests performed on brine that was not filtered after sampling, as with Cerro Prieto brine, include suspended or colloidal silica concentrations. These values are not greatly different than input values. Thus, there seems to be a return to equilibrium as long-term testing goes on. In the case of East Mesa, the temperature of the pore fluid while in the rock is approximately 170°C. The saturation solubility of silica at this temperature is 200-250 parts per million with respect to quartz and 700-800 parts per million with respect to amorphous silica. The 75 part per million value reported for EM-6 for silica is for brine that has been filtered through a 0.45 micron filter prior to analysis. This value is most probably for dissolved silica since the filter should retain suspended solids.

The calcium concentrations in the pore fluid before and after being introduced to the rock, again excluding tests CP-4 and CP-5, indicate that if any reactions occurred they were probably related to the dissolution of calcium carbonate. Since all of the specimens contain at least a trace of calcium carbonate (values reported as zero indicate less than 0.5%), this type of reaction is expected for calcium concentrations that are less than saturation. The East Mesa fluid samples show that bicarbonate tends to decrease in concentration with increasing detention time. This indicates that much of the pick-up of bicarbonate occurs early in the tests or while in the pore pressure system which is reasonable since it was difficult to completely remove all of

the retained air from the system and the specimen prior to introducing the pore fluid. Since the brine used in the Cerro Prieto tests had not been adjusted with respect to bicarbonate and since several specimens showed very high calcium carbonate content, carbonate pick-up from the atmosphere (by CO_2 dissolution) and from calcium carbonate dissolution is expected.

The purposes of this phase of the program were to insure equilibrium with respect to water-rock interactions and to gain insight into any reactions which might be occurring during a test sequence on a rock specimen if equilibrium was not achieved or disturbed by a change in stress state. Analyses of pre- and post-test pore fluid from the East Mesa and Cerro Prieto tests show that in cases where equilibrium was not achieved, adverse reactions were probably not of major consequence to short-term mechanical response. Nevertheless, some effects are present and include mechanisms such as calcium carbonate dissolution and transportation of suspended silica out of the rock samples.

The suspended silica, in particular, might be one of the best clues we have as to the mechanism of creep compaction in these rocks (when it occurs). For Cerro Prieto, the solubility of SiO_2 at test conditions is approximately 400 ppm for quartz and 1200 ppm for amorphous silica. Thus, a consistent picture of results with respect to silica during creep testing shows that the increased effective stress caused by reduction of pore pressure causes pressure solution at quartz contact boundaries. This causes a local supersaturation, but with time, as initial solution rate and initial creep rate diminish, equilibrium is once again achieved (see Figure 83). This will be discussed further in Chapters 8 and 9.

7. MINERALOGICAL AND STRUCTURAL RESULTS

The fluid chemistry work associated with this program, as discussed in the preceeding chapter, has clearly shown that some types of alterations have occurred during creep testing. Observe the calcite dissolution and precipitation and the silica mobilization resulting, possibly, from pressure solution. We report here two types of examinations to assist us in analyzing these effects. The first is x-ray diffraction (XRD) of the clay fraction before and after creep tests. The second is scanning electron microscope (SEM) examination combined with energy dispersive analysis by x-rays (EDAX) on pre- and post-test specimens in an attempt to observe mechanisms of creep compaction. These efforts have concentrated on the East Mesa specimens, which have undergone more extensive long-term creep testing.

7.1 X-Ray Diffraction

X-ray diffraction analyses were carried out with CuK-alpha radiation at 40 KV, 20 MA accelerating potential and current. In general, three sets of scans were done for each sample. The first was air dried, the second was exposed to ethylene glycol vapor for several hours, which causes expansion of the smectites, and the third was heated to 550°C to destroy kaolinite. A summary of tests done is given in Table 20. For XRD scans, the clays in the sandstone samples were separated by dispersion in deionized water, centrifuging, and sedimentation on glass slides. Clay separation was done on eight samples. For two specimens (EM-6 post-test and EM-7 post-test), useful clay separations were not recovered since the presence of soluble salts caused the clays to floculate and settle during the first centrifuge step when it was necessary to keep them in suspension.

Table 20

XRD Scans Obtained of Separated Clays

Well Number	Depth (feet)		Untreated	Glycolated	550°C
78-30	5505	EM1 Pre-Test EM1 Post-Test	√ √	√	√
78-30	5510	EM5 Pre-Test EM5 Post-Test	√ √	√ √	√
78-30	5510	EM6 Pre-Test	√	√	√
78-30	7142	EM7 Pre-Test	√		√
58-30	3273	EM8 Pre-Test EM8 Post-Test	√ √	√	√

7.1.1 EM-5

Pre-Test: The following four clays can be distinguished:

1. A discrete 7 angstrom phase which disappears when heated to 550°C, and is therefore a kaolinite-like mineral.
2. A regular mixed layer phase with a reflection at 23.3 angstroms containing 10 angstrom and 14 angstrom components. It does not expand (with glycolation) to 22 angstroms. Therefore, it is not montmorillonite, and it disappears with heating to 550°C. Poorly crystallized chlorite can be decomposed by this heat treatment, and therefore this phase is probably a regular mixed layer illite and poorly crystalline chlorite.
3. A discrete chlorite at 13.4 angstroms for the air-dried and glycolated material and at 13.6 angstroms when heated to 550°C.
4. An irregular 10 angstrom to 14 angstrom mixed layer clay with a peak at 10.8 angstroms in the air dried and glycolated specimen and an 11.9 angstrom peak when ehated to 550°C. This is probably an illite-chlorite mix.

Post-Test: The following phases occur:

1. A 7 angstrom phase which would appear to be alteration product of the kaolinite-like mineral. In the pre-test it could be a serpentine, but this is ambiguous because the glycolated sample yielded a peak at 7.03 angstroms and neither kaolinite or serpentine minerals respond to glycolation, so the shift from 7.25 angstroms to 7.03 can only be interpreted as the results of the aging of a metastable alteration product.
2. An irregular 10 to 14 angstrom mixed layer clay which first produced a peak at 11.2 angstroms and appeared to be an alteration of the irregular 10-14 angstrom mixed layer phase in the pre-test sample. It does not expand with glycolation, and is therefore probably illite-chlorite.
3. A discrete 13.4 to 13.6 angstrom phase which does not expand with glycolation and is therefore chlorite.
4. A regular mixed-layer illite-chlorite producing a reflection at 24 angstroms.

The clay alteration which appears to have occurred during the testing of this specimen, in summary, is alteration of the irregular 10-14 angstrom mixed layer illite-chlorite and the alteration of the kaolinite phase to produce some metastable alterations.

7.1.2 EM-8

Pre-Test: The following phases are present:

1. A discrete 7.08 angstrom phase which disappears with heating and therefore is kaolinite.
2. A possible three component irregular mixed layer phase with peaks at 9.0 angstroms air dried, 9.9 glycolated and 10 heated. This could be a kaolinite-illite-montmorillonite mixed layer.

3. A discrete 13.8 angstrom chlorite which does not expand with glycolation and becomes subdued with heating, it is therefore purely crystalline.
4. A regular mixed layer of 10 angstrom illite, 12 angstrom montmorillonite producing a peak at 22 angstroms. It expands to 26.8 angstroms with glycolation and disappears with heating.

Post-Test: The following phases are present:

1. A discrete 7.1 angstrom kaolinite.
2. An irregular mixed layer 10-14 angstrom phase.
3. A regular 10-15 angstrom mixed-layer phase producing a peak at 25 angstroms. In this case, the chlorite peak at 13.8 angstroms apparently was altered to other clays during the testing. Glycolation and heating work were not completed for this specimen and therefore the results are somewhat less certain.

7.2 Scanning Electron Microscopy - Energy Dispersive Analysis by X-Rays

The main purpose of the SEM work was to look for evidence in the form of structural alteration of the creep compaction that was observed during mechanical testing. The main technique used was to view and compare the surface morphology of quartz grains in both pre- and post-test samples. Processes such as dissolution and growth of euhedral quartz in pore space were expected to be observed. Figures 84a and b show two examples from an East Mesa creep test where we believe pressure solution is observable. In Figure 84a, note that the surface of the quartz appears to be corroded or eaten away as though dissolved. This was not ever observed in pre-test specimens. The dissolved surface has been covered by a fresh clay, probably a smectite. The interpretation of smectite is derived from the chemical composition through EDAX analysis, and from the general morphology of this clay as compared with pub-

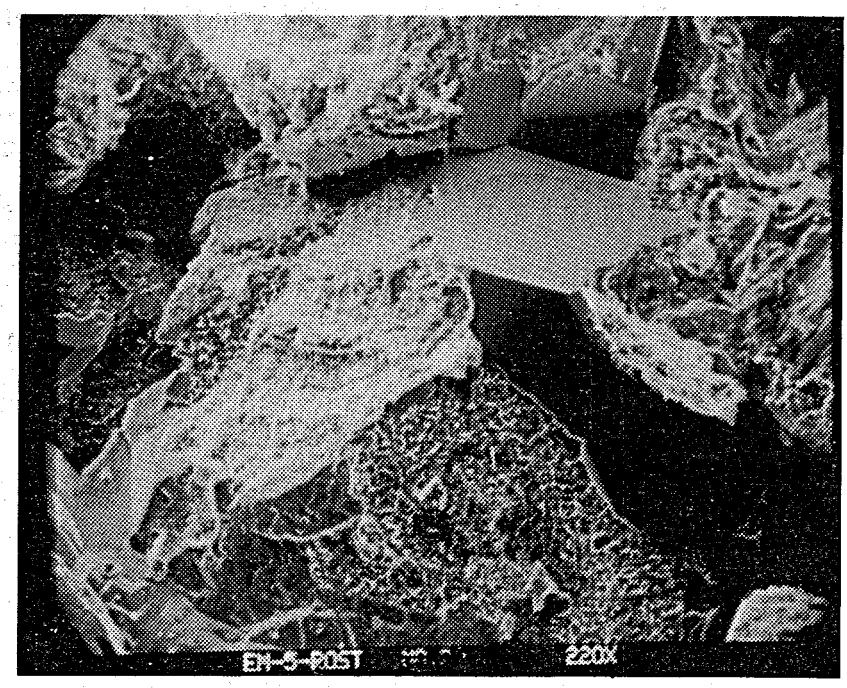

Figure 84a. SEM photomicrograph of quartz crystal in rock after creep test. Material is from East Mesa well 78-30.

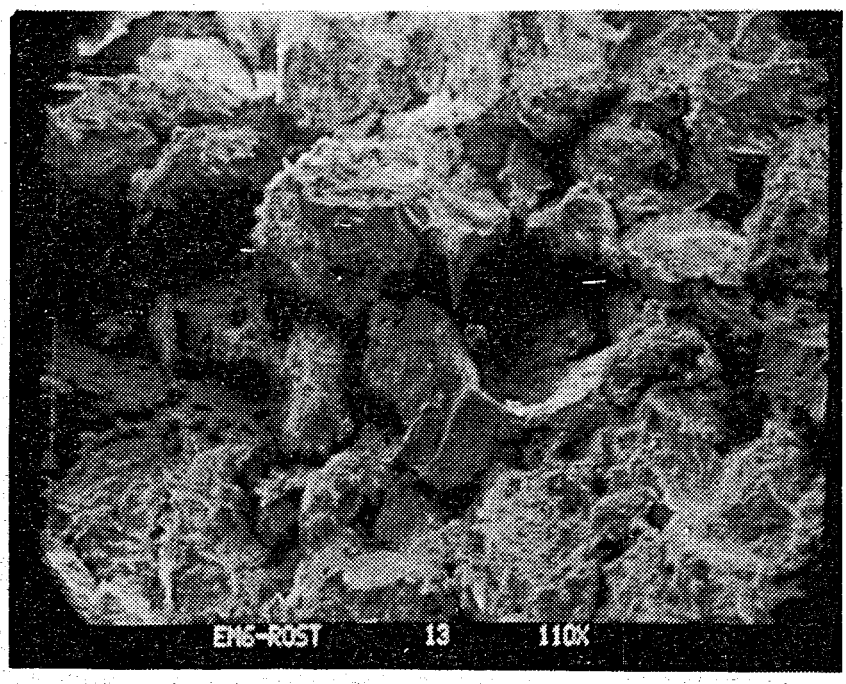

Figure 84b. SEM photomicrograph of void left by grain plucked during sample preparation process. Material is from East Mesa well 78-30 after creep test.

lished micrographs. Also note in Figure 84a that the center crystal has penetrated into the one above it, which possibly is additional evidence of pressure solution. In the other example, Figure 84b, a spherical void can be seen where a grain was plucked out during the breaking of the sample for test preparation. The quartz grain to the left gives an example of apparent dissolution along the surface that was in contact with the grain now removed. Just on top of the same grain, euhedral quartz overgrowth has occurred.

8. SUMMARY AND SYNTHESIS OF TEST RESULTS

Cores for this testing program were obtained from wells in the East Mesa and Cerro Prieto Geothermal fields in order to make measurements at simulated in-situ conditions for the purpose of determining the mechanisms of compaction and their relation to surface subsidence. A summary of the typical mineralogies of reservoir material that was obtained is given in Table 21. Some caprock material was obtained as well. Also shown in Table 21 are the approximate porosities of the rocks and the total dissolved solids contents of the reservoir brines. It can be seen from this table that both rock types are sedimentary sandstones. There is ample evidence, as well, of hydrothermal alteration in the rocks from Cerro Prieto. This can be seen, for example, by the epidote content of the Cerro Prieto rock. Epidote is a product of high temperature alteration which certainly occurs at the 300°C temperature of the Cerro Prieto reservoir.

Typical laboratory test conditions are shown in Table 22. The range of pressures are similar for the East Mesa and Cerro Prieto rocks; however, rocks from Cerro Prieto were generally tested at higher temperatures than rocks from East Mesa to correspond to the higher temperatures of the reservoir. Essentially, two types of tests were run (with some variations). The so-called basic tests began at reservoir conditions and then investigated the effects of changes in pore pressure, confining pressure and ratio of axial stress to confining pressure on the compressibility of specimens. The creep tests began at the same initial conditions as the basic tests and then investigated the effects of reduced pore pressure for long periods of time to determine time-dependent (creep) effects related to compaction. Some permeability measurements were also included with the creep tests.

Table 21

Typical Mineralogy of Test Specimens
(Minerals Given as % of Solids)

	East Mesa	Cerro Prieto
Quartz	75	65
Feldspar	7	10
Rock Fragments	6	–
Clays	5	10
Cement		
Calcite	2	1
Silica	5	7
Epidote	–	7
Porosity	20%	20%
Fluid T.D.S.	2,000 ppm	20,000 ppm
Temperature	165°C	300°C

Table 22

Test Conditions

	East Mesa	Cerro Prieto
Temp	165°C	250-300°C
P_c	3000-7000 psi	3000-7000 psi
P_p	1500-3000 psi	1500-3000 psi

A summary of basic test results is given in Table 23. Compressibilities for all materials range from 0.7 to 3.0 $x10^{-6}$ psi^{-1}. These are typical compressibilities for normally consolidated sandstones in this porosity range. In more detail, note that the compressibilities of the East Mesa caprock material, which is a fine grained siltstone, are greater than reservoir materials. Basic testing also indicated a greater amount of plasticity and sensitivity to differential stress (vertical to horizontal) in this material, as can be seen by the increase in compressibility related to testing with larger stress differences. The Cerro Prieto reservoir materials, in general, were more elastic than the East Mesa materials. The compressibilities were less and their sensitivities to stress difference were less. During some of the tests ultrasonic velocities were also measured, for possible use as a field indicator of compaction, to determine if these velocities were sensitive to compaction. Indeed, a sensitivity was measured, as shown in Table 24, that correlated with compaction-caused density increase. While the small increase in velocity, about 1%, is easily measured in the laboratory, it is of uncertain usefulness as a diagnostic indicator in the field.

A summary of creep test results is shown in Table 25. Creep test durations varied from about 0.2 to 9 $x10^5$ seconds. This covers a range of a few hours to greater than 10 days. In general, creep rates on the order of $1x10^{-9}$ per second were observed, measured as rate of change in volume strain. At this creep rate, were it steady, all porosity would be entirely removed from these rocks in a few years at most. However, it is unlikely that this reduction rate would continue at steady-state. Instead, the reduction would likely slow and then cease when a new equilibrium value of porosity was achieved. This will be further discussed in the next chapter on mechanisms and theory. Viewing the creep results in more detail we see that the apparent creep rate

Table 23

Basic Tests
Average Results

Compressibility (10^{-6} psi^{-1})

Test Type	Stress Difference	East Mesa Cap	East Mesa Reservoir	Cerro Prieto Reservoir
ΔP_p	Low	1.1	0.7	0.7
	Intermediate	1.9	1.1	0.7
	High	2.1	1.7	
ΔP_c	Intermediate	2.0	1.3	0.9
ΔP_p Uniaxial	Intermediate	3.0	1.1	0.8

Table 24

Ultrasonic Velocities
Average Results
(km/sec)

Cerro Prieto	P	S
Reservoir P_p	3.95 ± 0.12	2.36 ± 0.35
Reduced P_p	4.00 ± 0.09	2.41 ± 0.35
Change (%)	+1.3 ± 0.8	+2.2 ± 0.3

Table 25

Creep Tests
Average Results

	Average Duration (10^5/sec)	Average Rate (10^{-9}/sec)	Range of Rates (10^{-9}/sec)
East Mesa Intermediate Term	0.7	4.1	2.4 - 15.0
East Mesa Long Term	9.0	1.0	0.0 - 1.3
Cerro Prieto Short Term	0.2	7.2	1.7 - 87.0
Cerro Prieto Long Term	4.0	0.3	one test only

decreased as the duration of the test increased. This supports the observation that the creep compaction here is probably not at steady-state and is tending toward a new equilibrium value of porosity. However, none of the tests were carried to sufficient duration to experimentally confirm this supposition, and it would be impractical to test these rocks for the many months or years necessary to do this. Instead, we must turn to a theory based on mechanisms in order to extrapolate results to long periods of time, and use the experiments to provide an initial creep rate only.

Comparing the results for East Mesa and Cerro Prieto we see that creep rate is fairly consistent for the East Mesa sandstone rocks studied but not so consistent for Cerro Prieto rock, where specimens from some of the wells exhibited fairly rapid creep while others exhibited little or no creep within our limits of resolution. For Cerro Prieto, creep rate tended to be higher for siltstones than for sandstones, and higher for rocks of higher porosity. One specimen exhibited extremely high creep rate (almost two orders of magni-

tude greater than the average). It was a relatively unconsolidated fine-grained sandstone specimen from the Cerro Prieto reservoir. For East Mesa, only the reservoir sands exhibited significant long-term creep. The caprock appeared to stop creeping after several days.

The above results are consistent with the smaller variability of the East Mesa resevoir rock that we have tested, and the greater variability in the Cerro Prieto rocks (where Cerro Prieto material has come from many different wells and many different depths and zones of hydrothermal alteration in the reservoir). The higher temperature of the Cerro Prieto reservoir did not in itself result in a higher measured creep rate in this rock. On the contrary, the mineralogical state of the Cerro Prieto specimens that were most highly hydrothermally altered perhaps even inhibited creep. This is possibly explained by the previous acceleration of in-situ mechanisms that resulted in cementation and reduction of stress concentrations in hydrothermally altered material so that the rock was already stable in a high-temperature stressed environment prior to testing. It follows that less-altered sediments, as seen in some of Cerro Prieto and all of the East Mesa rocks, are more susceptible to perturbations from their natural state. This explanation is consistent with normal views of sedimentary and metamorphic processes in rocks.

In summary, we have observed that compaction is time-dependent in most of the rocks we have observed. For a 1,000 psi reduction in pore pressure, the instantaneous volume strain associated with compaction (for a compressibility of about $1x10^{-6}$ psi) is about $1x10^{-3}$. Typically, the creep we have observed would double this volume strain in about one day and increase it by a factor of ten in about three months, assuming a long-term creep rate of about $1x10^{-9}$ per second. This means that in three months time the apparent long-term compressibility with respect to pore pressure reduction is one order of magni-

tude greater than that which would be measured by ordinary laboratory techniques.

Fluid chemistry, measured for both input and output fluids, has been controlled to minimize the effect of non-equilibrium reactions otherwise caused by use of improper test fluid. This was particularly important at the elevated temperatures of these tests. As an indicator of chemical/mechanical effects that may relate to possible mechanisms of creep compaction, silica analysis has been most useful. During the earlier phases of creep testing, the silica content of output fluids increased to levels beyond those of saturation. However, for later phases of creep testing, silica concentrations trended back toward values that are consistent with equilibrium. This could indicate pressure solution at asperity contacts between quartz grains as a possible mechanism of creep compaction. At these points, quartz would be driven rapidly into solution and could easily exceed equilibrium values for the solution at its own pressure and temperature. Then, with time, the excess quartz in solution would have to come out of solution, most likely as euhedral quartz in areas where stress concentrations are absent. This has been previously observed as a mechanism of diagenesis in sandstone sedimentary sequences. We have perhaps only accelerated the process by the increase in effective stress during our tests. Some confirming evidence of this is found in the SEM results on post-test material.

Permeability values obtained for Cerro Prieto material, and summarized in Table 26, indicate an average initial permeability of about 4 millidarcies. This permeability is lower than that inferred from field tests at the reservoir. This would indicate that flow, on average, in this geothermal reservoir must be through channels of higher permeability that were not recovered as cores or fractures, or both. It is certainly conceivable that such channels

Table 26

Permeability Tests - Average Results

Mean at Room Temp. (md)	Temp. Change (%)	Creep Change (%)
4.0 ± 4.8	-40 ± 23%	-39 ± 18%

or fracture zones could exist considering the tectonically active nature of the area. With temperature increase, we observed a 40% decrease of permeability, but with pore pressure decrease we observed no statistically significant change in permeability. With creep we observe a further 39% reduction in permeability. It is interesting to note that creep had a more significant effect on permeability than on compressibility. This could be associated with creep compaction mechanisms that are active at asperity positions, which would possibly be very near to pore throats, therefore causing an amplifying effect. This conclusion, however, must be considered to be somewhat speculative, since other mechanisms of permeability reduction, such as particulate plugging, could also be active here.

In general, the testing done on this program has indicated that rocks from Cerro Prieto and East Mesa behave more or less as normally consolidated sandstones in short-term response. However, in long-term response the rocks exhibit a creep tendency that is most pronounced in the less consolidated, less hydrothermally altered material. The amount of creep is sufficient to cause the amount of compaction over a period of months or years to be one to two orders of magnitude greater than initial compaction related to instantaneous quasi-elastic behavior.

9. MECHANISMS OF CREEP AND THEORETICAL MODELING

Compaction as triggered by pore pressure reduction has been observed in all rocks tested during this program. Additionally, many of these rocks exhibited time-dependent behavior in the form of creep compaction when pore pressure reduction was held constant for long periods of time. It was not possible to conduct enough tests for long enough periods of time to completely determine creep compaction histories. This is not surprising since compaction as part of the diagenetic process in the field occurs over many, many years and it is not practical to perform tests in the laboratory over this long time period.

For subsidence prediction, an ultimate compaction value must be known. Therefore, the most useful result of this project would perhaps be to determine when creep compaction occurs and to be able to extrapolate it to times that are appropriate for reservoir production. To do this, it is necessary to develop a theory of creep compaction that allows reliable extrapolations to be made that are based on measurable laboratory parameters. An appropriate method in this case cannot be entirely empirical (curve fitting) because we do not know from our measurements if the long-term creep rate is steady-state or decaying. To predict ultimate compaction, the theory must therefore be based on physically plausible mechanisms.

Four possible mechanisms of creep compaction have been considered:

- grain plasticity
- slow crack growth
- frictional sliding
- pressure solution

By "plasticity" we mean compaction caused by true plastic deformation of grains. Previous work would indicate that the temperatures and pressures required for true plastic flow in these rocks are too large for this to be a significant mechanism although certain materials, such as calcite, salt, and some clays, might deform by true plasticity if they supported a significant part of the matrix. However, the rocks studies here appear to gain skeletal support primarily from their quartz grain content, and grain plasticity would appear not be be important.

Slow crack growth-caused compaction is the creation and/or growth of microcracks to relieve stress concentrations and cause associated deformation. This is certainly a conceivable mechanism here. However, our petrographic and SEM analyses have found no evidence of substantial crack growth in these specimens except in the cases where differential stresses have clearly approached levels causing gross specimen failure.

Frictional sliding at grain contacts is another conceivable compaction mechanism. However, we have also found no evidence for this, except as it might be associated with pressure solution.

In our judgment, the most likely mechanism for most of the creep compaction observed in these tests is pressure solution at quartz grain asperities. Solution and the resulting closure at these asperities would relieve stress concentrations and directly cause compaction. It would also lead to frictional sliding on surfaces that are under shear that contact those asperities, and indirectly lead to compaction. Pressure solution has been demonstrated to be a significant mechanism in the normal diagenetic process, especially in saturated sand bodies at the depths of typical oil and gas reservoirs that have not yet experienced metamorphism (Renton, et al., 1969; Mosher, 1976; DeBoer, 1977; Wilson and Sibley, 1978; Sprunt and Nur, 1979). (The process of pressure

solution is less important if the sands are dry. In this case, the quartz grains instead tend to fracture and break.)

The objective of the theoretical part of this work, then, was to develop a theory of creep compaction based on pressure solution as a root cause. To accomplish this we have taken a previously demonstrated theory of static pore collapse, the spherical pore theory developed by Bhatt, Carroll and Schatz (1975), and modified it with the help of a pressure solution theory of creep as developed by Rutter and Mainprice (1978).

9.1 Static Pore Collapse Theory

The spherical pore theory has had considerable success in describing the inelastic deformation of porous geologic materials. Its basis was introduced by McKenzie (1950) for porous metals. Other developments were made by McKenzie and Shuttleworth (1949), Torre (1978), Chadwick (1963), Hewitt, et al. (1973), Carroll and Holt (1972), Chu and Hashin (1971), and Butcher, et al (1974). Bhatt, Carroll and Schatz (1975) were the first to adapt this theoretical method to porous rocks. They performed this adaptation by using a Mohr-Coulomb model for the matrix material rather than a ductile or ductile-strain hardening theory for the matrix material as had been used previously.

A brief outline of the method follows: The pores in the real solid, as shown in Figure 85, are represented by an equivalent solid consisting of a homogeneous porous continuum surrounding a Mohr-Coulomb material ("real material") and a pore. It is acknowledged that the true pores in a rock are not spheres, but probably are better described as cracks of varying aspect ratios; however, to account for inelastic deformation in rock, the spherical pore theory has been demonstrated to appropriately represent the internal shearing stress concentrations that are caused by local inhomogeneities associated with granularity and porosity. In fact, this "appropriate representation" is the

SPHERICAL PORE THEORY

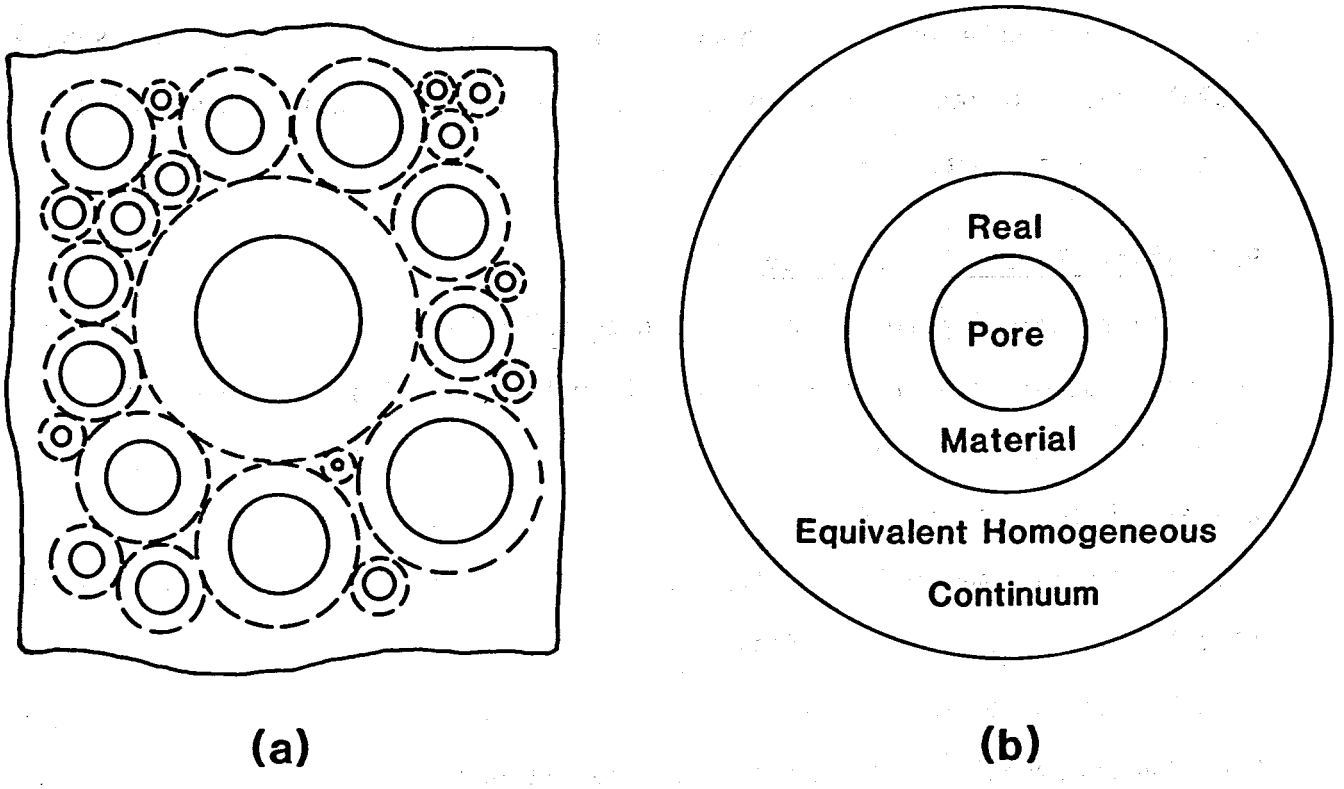

Figure 85. Diagram indicating the concept of spherical pore deformation theory. (a) shows porous solid represented by many pores of different sizes. (b) shows final representation of porous solid as a single pore surrounded by Mohr-Coulomb "real" material, surrounded by an equivalent homogeneous continuum.

strength of the spherical pore theory allowing great geometric simplicity for which mathematical closed-form results are easily obtained.

The inelastic deformation of the single spherical pore that now represents all porosity is treated as shown in Figure 86. Originally, the material is elastic with outer boundary b and inner boundary a. It is pressurized at boundary b. Boundary a, enclosing the pore, may be filled or partially filled with water. As boundary b is compressed inward due to pressurization, inelastic behavior begins due to shearing stress concentrations at boundary a. The created inelastic zone, demarked by the region between boundaries a and c, moves outward as pressure is increased. With sufficient pressurization, eventually all of the material behaves inelastically so that boundaries b and c coincide. It is assumed for the remainder of this theoretical discussion that the long-term equilibrium behavior of a normally consolidated porous rock may be described by the curve generated for the fully inelastic case, where boundaries b and c coincide. This is the state toward which creep compaction is assumed to progress.

The long-term equilibrium state, therefore, is given by

$$P = \frac{Y}{\beta} \left(\phi^{-2\beta/3} - 1\right) \qquad (1)$$

where P is the effective hydrostatic stress and ϕ is porosity. Beta (β) and Y are Mohr-Coulomb deformation parameters for the matrix material as given by

$$(1 + \beta)\, \sigma_{max} - \sigma_{min} = Y \qquad (2)$$

where σ_{max} and σ_{min} are maximum and minimum principal stresses, respectively. It can be seen that β is a frictional coefficient parameter and Y is an initial shearing strength, or cohesion, parameter. An example of the prior success of this theory is given in Figure 87, which shows the pressure-porosity loading and unloading behavior for a porous tuff, as matched by the theory.

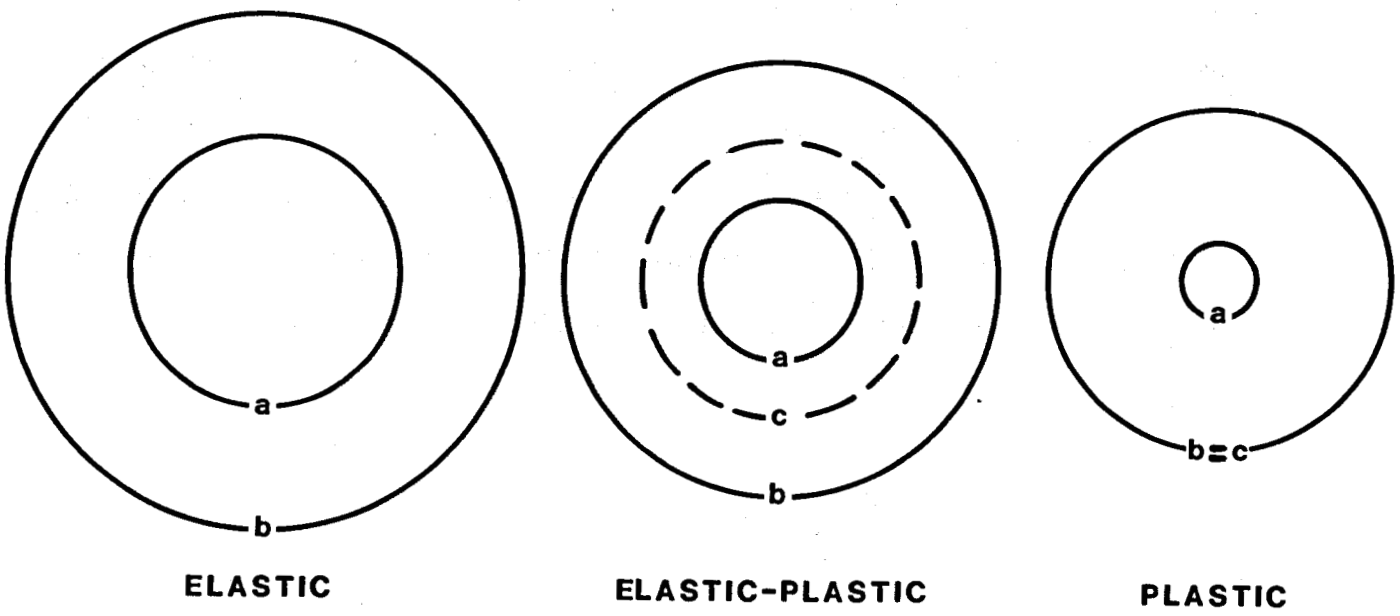

Figure 86. Deformation of pore in spherical pore theory. (a) is inner pore boundary and (b) is outer pore boundary. When inelastic deformation begins, boundary (c) is formed and moves outward toward boundary (b). Finally, in fully plastic state, boundaries (b) and (c) coincide as the pore collapses.

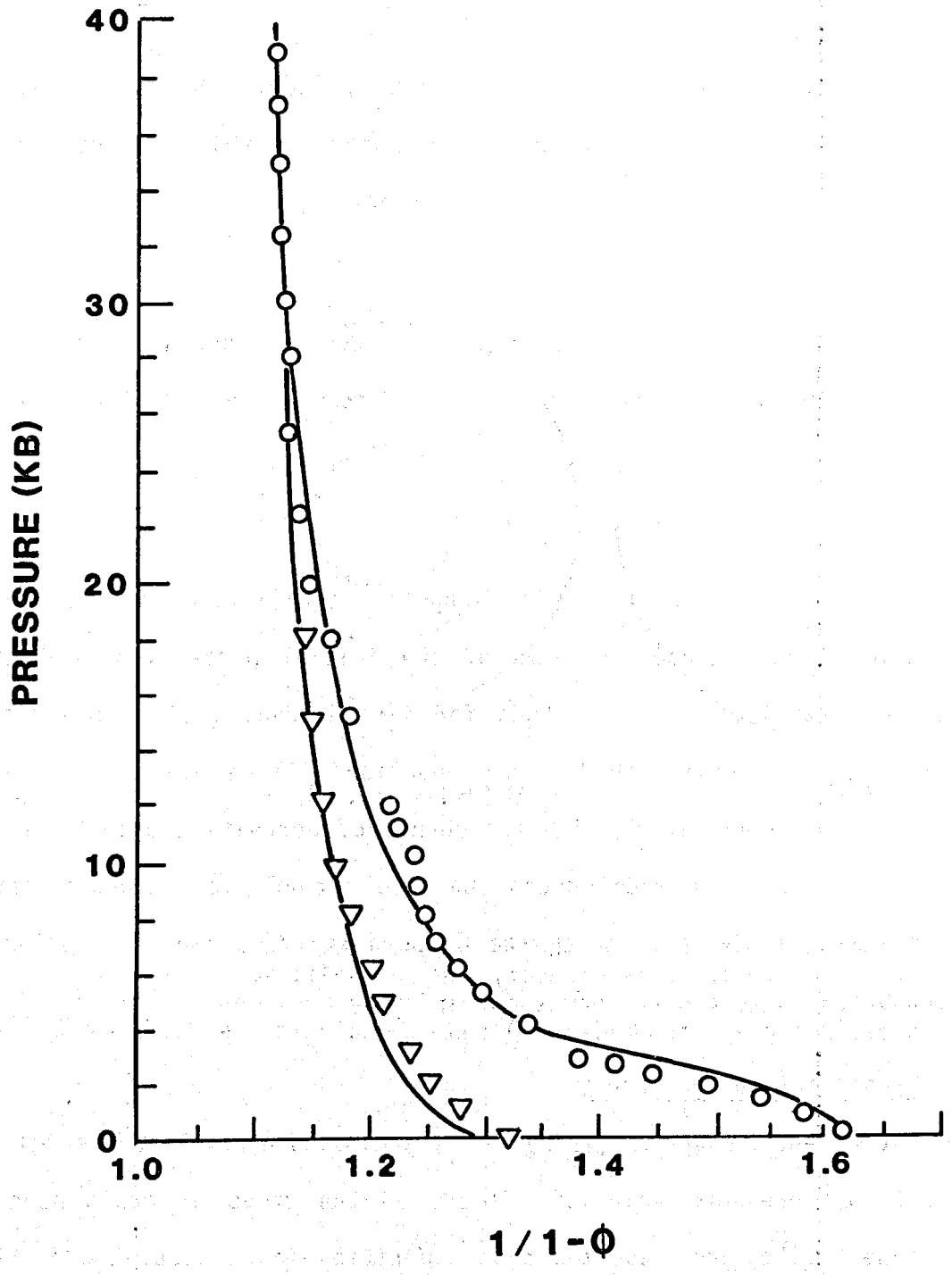

Figure 87. Spherical pore theory (solid line) compared with compaction data for a porous tuff, shown by circles for ascending pressure points and triangles for descending pressure points.

(Equation 1 is the equation for the loading portion of the behavior shown from about 1 kilobar up to maximum stress.)

For many porous rocks, a value of β of about 4.5 has been shown to be appropriate. For simplicity in the remainder of this analysis, that value will be used. Equation 1 then takes the form

$$P = \frac{2}{9} Y (\phi^{-3} - 1) \tag{3}$$

which contains only a single parameter, Y. Consider now a change in porosity, $\Delta\phi$, as triggered by a change in effective stress, ΔP. Differentiating Equation 3, we obtain

$$\Delta\phi = - \frac{3}{2} \frac{\phi_o^4}{Y} \Delta P \cong \frac{\Delta V}{V} \tag{4}$$

Equation 4 gives us the change in long-term equilibrium porosity for a given effective stress change in terms of the initial porosity ϕ_o and the single cohesion parameter, Y. Note that for insignficant grain compaction, $\Delta\phi$ is equal to volume strain, $\Delta V/V$. This equation will be used as our basic equation for the long-term equilibrium change of porosity caused by a change in effective stress. To model creep, we need now only to introduce time dependence to provide the rate of change of porosity from one equilibrium state to the next.

9.2 Pressure Solution Theory

Rutter and Mainprice (1978) have introduced a novel and useful theory to account for pressure solution effects on the creep at grain boundaries in sandstones. They have assumed that asperities in contact, under shear, dissolve slowly by pressure solution, and that the pressure solution rate may be related to the shear sliding rate. This is an ideal theory to combine with the spherical pore theory, since the spherical pore theory expresses effective

confining stress at external boundaries and compaction as related to shearing stresses and strains upon internal boundaries.

Rutter and Mainprice's theory is summarized by

$$u = \frac{8\ (\sigma_1-\sigma_3)\ C_o\ \delta\ D_b}{h^2\rho}\left(\frac{\partial\ \ln\ C_o}{\partial\ P}\right)_T \qquad (5)$$

where u is the sliding rate, $\sigma_1 - \sigma_3$ is the internal differential (shearing) stress at the grain boundary, C_o is the solubility of the solid (which is in general pressure and temperature dependent), δ is the grain boundary width, D_b is the grain boundary diffusion coefficient, h is the amplitude of grain boundary asperities, and ρ is the density of the solid. Furthermore, they have suggested that the overall shear strain rate, e, is given by

$$e = u/d \qquad (6)$$

where d is grain size. For the case of quartz, with the assumption of a 1.0 micron crack width, one obtains the result given by

$$e = 11.4\text{x}10^{-8}\ \frac{(\sigma_1 - \sigma_3)}{d}\ e^{-\frac{7460}{RT}}\ e^{0.415\ P_p} \qquad (7)$$

where P_p is the pore pressure. Units are seconds, kilobars, and millimeters.

Equation 7 for a 0.15 mm grain size is plotted as the family of straight lines shown in Figure 88, along with some data obtained by Rutter and Mainprice. As Rutter and Mainprice point out, results agree with their theory for small strain rates and relatively low stresses. For high strain rates and higher stresses, crack production and growth is probably the more dominant mechanism. However, as can be seen, the Rutter and Mainprice theory is very well-suited for our purposes because the appropriate stresses and strain rates are appropriate for the creep compaction that we have measured. To use the figure, we need only to determine the grain size of the specimen, adjust the lower axis accordingly, determine the internal shearing stress, and read off an appropriate strain rate for creep compaction.

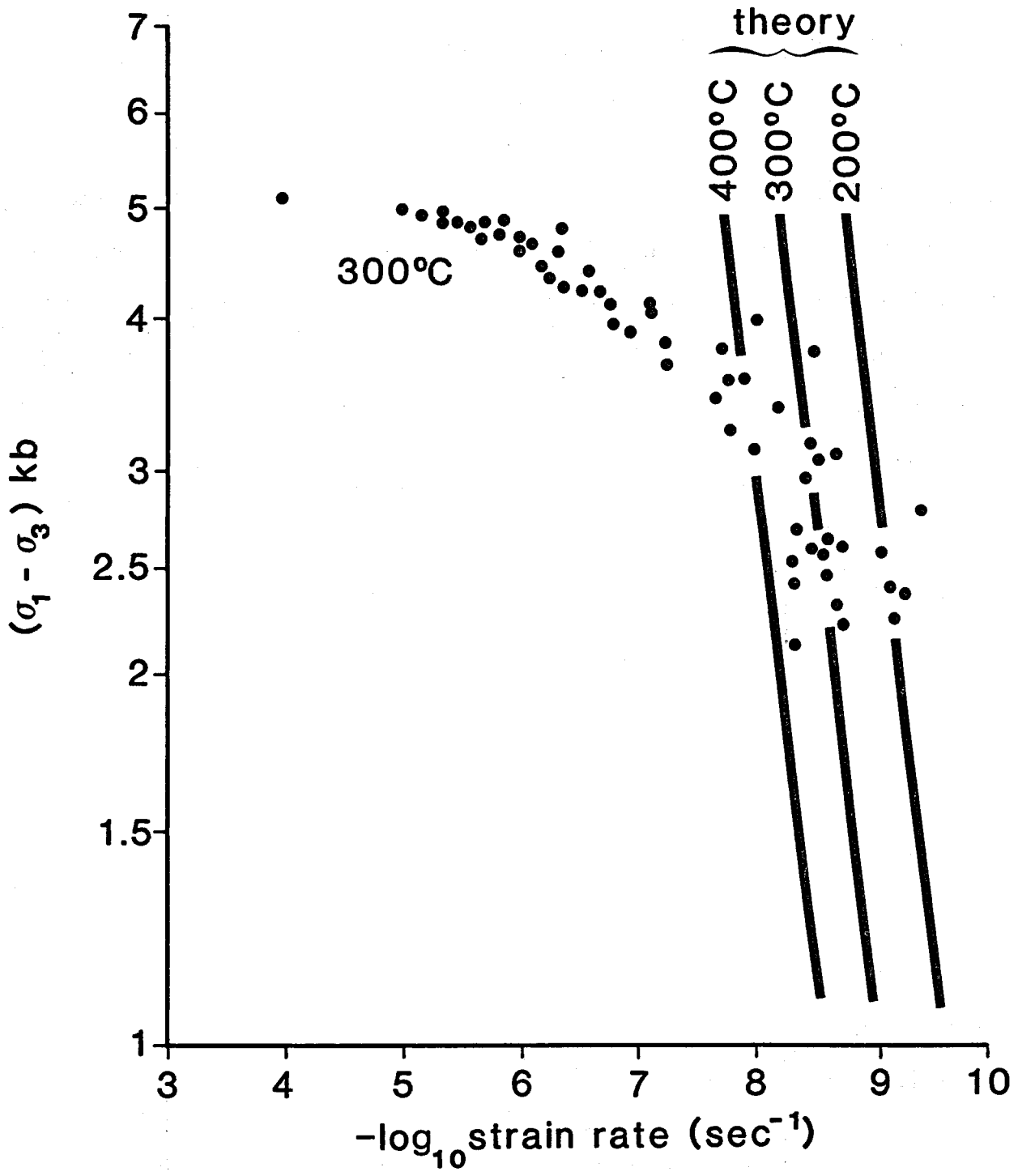

Figure 88. Internal contact shearing stress versus strain rate according to the theory of Rutter and Mainprice. Shearing stress here is the actual stress occurring at grain contacts within the material.

9.3 Creep Compaction Theory

To use Figure 88 or Equation 7, we need an expression for the internal stress difference, $\sigma_1 - \sigma_3$, as a function of the external effective pressure P. This can be obtained from spherical pore theory by our previous assumption that the internal shearing stresses are at or near to a state of Mohr-Coulomb yield as given by

$$\sigma_1 - \sigma_3 = Y\ (1 + \beta) \left(\frac{r}{a}\right)^{2\beta} \tag{8}$$

When integrated over a sphere the average volume-weighted shearing stress, assuming a value of $\beta = 4.5$ as before, is given by

$$(\sigma_1 - \sigma_3)_{avg} \cong sY/\phi^3 \tag{9}$$

where we have assumed that the grain-to-grain shear stress is enhanced by the ratio of grain diameter to grain contact diameter, s. If combined with Equation 3, one then obtains

$$(\sigma_1 - \sigma_3)_{avg} \cong s\ (Y + 4.5\ P) \tag{10}$$

If P is of the same order as Y, which should be true if stresses are not far from Mohr-Coulomb equilibrium, a shearing stress concentration on the order of five times s should exist.

For further calculation, considering the highly approximate nature of this analysis, we will assume, for simplicity, a factor of five times s stress concentration as given by

$$(\sigma_1 - \sigma_3)_{avg} \cong 5s\ P \tag{11}$$

Referring to Figure 88 and using Equation (11), we see that for a mean effective stress in the range of 3,000-4,000 psi (as for our tests) and for s = 2 (giving an internal shearing stress of about 3 kilobars) a creep strain rate of about 1×10^{-9} per second would result. This is the strain rate order that has been observed in our experiments.

Let us now assume that creep compaction follows an exponential decay curve with time constant τ as given by

$$\phi = \phi_o - \Delta\phi\ (1 - e^{t/\tau}) \tag{12}$$

For $\Delta\phi$ as given by Equation 4, and the initial creep strain rate, e, as given either by our experiments or by the Rutter and Mainprice-derived theory, one obtains the results

$$\phi = \phi_o - \frac{3}{2}\frac{\phi_o^4}{Y}\ \Delta P\ (1 - e^{-t/\tau}) \tag{13}$$

$$\tau = \frac{3}{2}\frac{\phi_o^4\ \Delta P}{Ye} = \frac{\Delta\phi}{e} \tag{14}$$

In Equations 13 and 14, there are but two undetermined parameters, Y and e. The creep compaction problem has been reduced to determining the appropriate values to use for the long-term effective internal cohesion, Y, of the porous rock, and the initial creep rate, e. It is suggested that an appropriate value to use for Y may be obtained by matching porosity-pressure curves, such as those obtained from Equation 3, with porosity-depth curves as actually seen in the reservoir. If an effective stress of about one-half psi per foot of burial is assumed, Equation 15 results for Y, where z is depth of burial.

$$Y = \frac{9}{4}\ z\phi_o^3 \tag{15}$$

Combining equations, we then obtain

$$\Delta\phi = -\frac{2}{3}\frac{\phi_o\ \Delta P}{z}\ (1 - e^{-t/\tau}) \tag{16}$$

$$\tau = \frac{2}{3}\ \frac{\phi_o\ \Delta P}{ze} \tag{17}$$

where e may be obtained from experiment or Equation 7. Suppose for example, that initial porosity is 0.20, ΔP is 1000 psi, z is 5000 feet and initial strain rate is 10^{-9} per second. We then obtain

$$\Delta\phi = -0.027\ (1 - e^{-t/\tau})$$

$$\tau = 2.7\text{x}10^7 \text{ sec (309 days)}$$

The maximum porosity change is -0.027 and the time constant is 309 days.

As a final result of this approximate theory, combine the creep rate from Equation 7 (neglecting the effect of pore pressure, which is small), the stress concentration result of Equation 11, and the previous assumptions concerning the relationship of depth of burial to pore pressure, to give a theoretical result for the creep rate of

$$e = 7.9\text{x}10^{-12} \frac{(0.5\ z + \Delta P)s}{d} e^{-\frac{3730}{T}} \text{sec}^{-1} \qquad (18)$$

where z is in feet, P is in psi, d is in mm and T is in °K. This result assumes that the average shearing stress concentration is given by Equation 11. It is expected that s might range from one to ten or more. Therefore, looking at Equation 18 we would expect that for equivalent rock types, the highest creep rate would be observed in materials with:

- the smallest grain sizes, thus decreasing a
- the most angular grains, thus increasing s

This is nicely consistent with what we have observed in testing. For example, Cerro Prieto sample M-93 had a small grain size and had among the most angular grains of the rocks that we tested. It also had the highest creep rate. Sandstones with low creep rate tended to be larger-grained and have more rounded grains.

For the example mentioned above, (20% initial porosity, 10^{-9} initial creep rate, ΔP = 1000 psi, z = 5000 feet), a long-term extrapolation is shown in Figure 89. Note that compaction effects do not diminish significantly until the second year. Also note how small the initial (short-term) compaction (small vertical segment at ϕ = 20%) is as compared to the total long-term compaction. Since the parameter values used for this example calculation are typical of our laboratory results, we might expect Figure 89 to represent a realistic case.

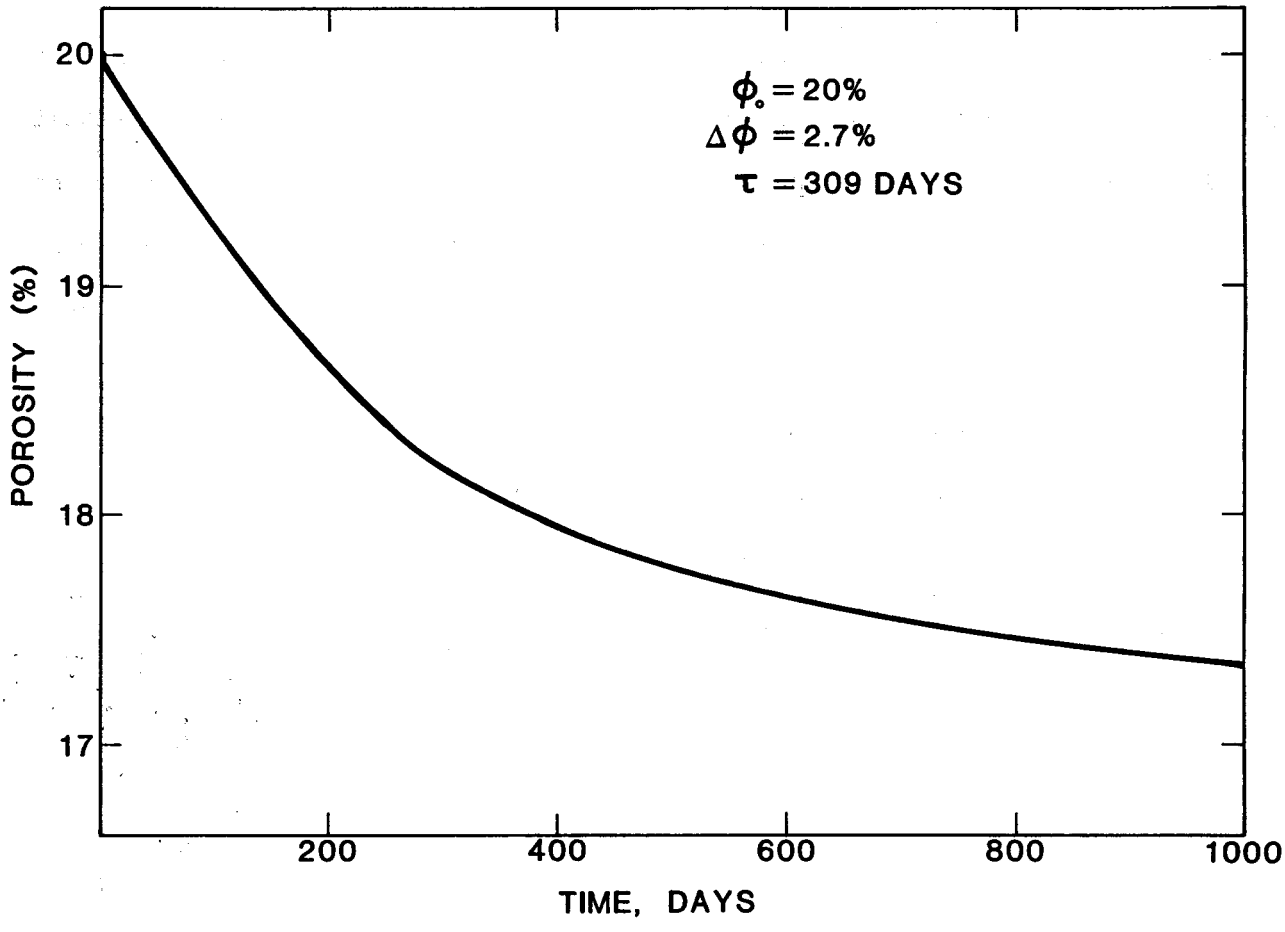

Figure 89. Long-Term sandstone creep compaction extrapolation predicted by theory derived in text and for parameters typical of those measured during this program.

10. CONCLUSIONS AND IMPLICATIONS FOR SUBSIDENCE PREDICTION

This program has demonstrated that rocks from the East Mesa and Cerro Prieto geothermal fields behave quite normally with respect to instantaneous compaction as caused by pore pressure reduction, having compressibilities of the order $1x10^{-6}$ psi^{-1}. They also demonstrate a tendency to compact further with time. The rate of creep compaction varies from rock to rock, averaging about 10^{-9}/sec and is statistically significant. The creep results are consistent with an approximate theory of creep compaction developed here that is based on spherical pore analysis and previous work on pressure solution in quartz sandstones.

Test results show that for a typical 1000 psi reduction in pore pressure, similar to that caused by reservoir production, a compaction strain of 0.001 can be expected to be observed instantaneously. However, for a creep rate of $1x10^{-9}$/sec, an ultimate compaction of about 0.03 in a time period of a few years can be expected. These results are approximate and are based on our theoretical extrapolation. Nevertheless, one sees that this ultimate compaction is a factor of 30 greater than the initial compaction. An alternative statement of this result is that the ultimate effective long-term compressibility is about $30x10^{-6}$ psi rather than $1x10^{-6}$ psi.

According to the theory presented here, the <u>magnitude</u> of ultimate creep compaction is a function mainly of initial porosity and pore pressure drop and not a strong function of rock type. (It is important to note here, that we have assumed a normally consolidated rock, that is, one that has not previously experienced a higher effective stress than it currently experiences in the reservoir, and a non-highly cemented rock. Preconsolidated rock or highly cemented rock will probably show less tendency to creep compact.) On the other

hand, the rate of creep compaction is a function mainly of the pressure solution rate, and is therefore strongly dependent upon grain type, temperature, grain contact angularity, cementation that would reduce stress concentrations, etc. However, even accounting for our uncertain knowledge of the values of parameters, we find that an initial creep compaction rate on the order 10^{-9}/sec should be common for fairly clean, normally consolidated sandstones. Extremely angular-grained, small-grained and high porosity sands might be expected to have a higher initial creep rate.

As a result of the experimental and theoretical analyses performed during this program, we conclude that the difference between laboratory-measured and field-measured moduli that is usually attributed to size effect (certainly some part of this is truly size effect) may to some extent be attributable to time-dependent creep phenomena that are not ordinarily observed in the laboratory because of the short-term nature of most laboratory tests. Unfortunately, it would not be practical to routinely test rock for periods of months or years; however, it is suggested that when a large suite of rocks is being tested, and accurate moduli values are very important, that at least a few of these rocks be tested for creep effects.

Consider, for example, the effect on the compaction of a subsurface reservoir, leading to subsidence. For a reservoir thickness of 100 meters and a pore pressure reduction of 1000 psi, the instantaneous compaction-related thickness loss predicted by results here might be approximately 10 centimeters. If this were all the compaction to occur, it would be expected to be translated to the surface as an ultimate subsidence of a few centimeters at most. However, with the occurrence of creep, an ultimate compaction of 30 times this amount might occur. The compaction thickness loss is now 300 centimeters, and the surface subsidence resulting from this might be a few tens of centimeters, which, depending upon location, might be significant.

11. REFERENCES

Butcher, B.M., Carroll, M.M. and Holt, A.C., "Shock Wave Compaction of Porous Aluminum," J. Appl. Phys. 45, 3864-3875, 1974.

Carroll, M.M. and Holt, A.C., "Static and Dynamic Pore-Collapse Relations for Ductile Porous Materials," J. Appl. Phys. 43, 1626-1636, 1972.

Chadwick, P., "Compression of a Spherical Shell of Work Hardening Material," Int. J. Mech. Sci. 5, 165-182, 1963.

Chu, T.Y. and Hashin, Z., "Plastic Behavior of Composites and Porous Media Under Isotropic Stress," Int. J. Engng. Sci. 9, 971-994, 1971.

De Boer, R.B., "On the Thermodynamics of Pressure Solution - Interaction Between Chemical and Mechanical Forces," Geochimica et Cosmochimica Acta, Vol. 41, pp. 249-256, 1977.

Elders, W.A., Jr., Hoagland, J.R., Olson, E.R. McDowell, S.D. and Collier, P., "A Comprehensive Study of Samples from Geothermal Reservoirs: Petrology and Light Stable Isotope Geochemistry of Twenty-Three Wells in the Cerro Prieto Geothermal Field, Baja California, Mexico," Institute of Geophysics and Planetary Physics, University of California, Riverside, 1978.

Elders, W.A., ed., Guidebook, "Geology and Geothermics of the Salton Trough," Geological Society of America 92nd Annual Meeting, San Diego, 1979.

Grimsrud, G.P., Turner, B.L. and Frame, P.A., "Areas of Ground Subsidence Due to Geofluid Withdrawal," Geothermal Subsidence Research Management Program, Lawrence Berkeley Laboratory, 1978.

Hewitt, R.L., Wallace, W. and deMalherbe, M.C., "The Effects of Strain-Hardening in Powder Compaction," Powder Metall. 16, 88-106, 1973.

Mackenzie, J.K. and Shuttleworth, R., "A Phenomenological Theory of Sintering," Proc. Phys. Soc., B62, 833-852, 1949.

Mackenzie, J.K., "The Elastic Constants of a Solid Containing Spherical Holes," Proc. Phys. Soc. B63, 2-11, 1950.

Mosher, S., "Pressure Solution as a Deformation Mechanism in Pennsylvanian Conglomerates from Rhode Island," J. of Geology, Vol. 84, 1976.

Reed, M.J., "Geology and Hydrothermal Metamorphism in the Cerro Prieto Geothermal Field, Mexico," Proceedings, Second U.N. Symposium on Development and Use of Geothermal Resources, 1, 539-547, 1976.

Renton, J.J., Heald, M.T. and Cecil, C.B., "Experimental Investigation of Pressure Solution of Quartz," J. of Sedimentary Petrology, Vol. 39, No. 3, p. 1107-1117, 1969.

Rutter, E.H. and Mainprice, D.H., "The Effect of Water on Stress Relaxation of Faulted and Unfaulted Sandstone," Pageoph, Vol. 116, 1978.

Sprunt, E.S. and Nur, A., "Reduction of Porosity by Pressure Solution: Experimental Verification," Geology, Vol. 4, p 463-466, 1979.

Torre, C., "Theorie und Verhalten zusammengepreßteer Pulver," Berg- u. Hüttenmännische Monatshefie 93, 62, 1948.

Wilson, T.V. and Sibley, D.F., "Pressure Solution and Porosity Reduction in Shallow Buried Quartz Arenite," American Association of Petroleum Geologists Bulletin, V. 62, No. 11, p. 2329-2334, 1978.

GPO 687-009/8377